UNIVERSITY OF CALIFORNIA,
IRVINE

A skin integrated sheet device for pancreatic islet transplantation

DISSERTATION

submitted in partial satisfaction of the requirements
for the degree of

DOCTOR OF PHILOSOPHY

in Biomedical Engineering

by

Rachel Ellyn Gurlin

Dissertation Committee:
Professor Elliot L. Botvinick, Chair
Professor Christopher C.W. Hughes
Professor Bernard Choi

2019

Dedication

To my mom, Gwen Utterberg-Gurlin, for her unconditional love in supporting my academic journey and dreams.

To my sister, Michelle Gurlin, who was diagnosed with type 1 diabetes when we were kids, for her continual belief in me and inspiration for my research and work. Your daily fight against this disease keeps me motivated to make this life easier for you.

I love you both with all my heart.

Table of Contents

List of Figures v
List of Tables vii
List of Equations viii
Acknowledgements ix
Curriculum Vitae xi
Abstract xvii
Chapter 1: Introduction 1
1.1 Type 1 diabetes 1
1.2 Islet transplantation 1
1.3 Islet encapsulation 2
1.4 Subcutaneous transplantation site 4
1.5 Summary and approach 4
Chapter 2: Slit Sheet Vascularization 7
2.1 Introduction 7
2.2 Materials and methods 8
2.2.1 Sheet fabrication 8
2.2.2 *In vivo* study 9
2.2.3 Histological preparation 9
2.2.4 Histological staining 10
2.2.5 Quantification of vessel and nerve count/morphology 11
2.2.6 Statistical analysis 11
2.3 Results 11
2.4 Discussion 16
2.5 Conclusion 19
Chapter 3: Device Development 20
3.1 Introduction 20
3.2 Materials and methods 22
3.2.1 Early prototype device fabrication 22
3.2.2 Later prototype device fabrication 23
3.2.3 Islet isolation 24
3.2.4 First generation *in vitro* islet loading 24
3.2.5 Second generation *in vitro* islet loading 25
3.2.6 Islet viability and imaging 26
3.2.7 *In vivo* device implantation and lectin staining 27
3.2.8 Fabrication of Oxygen Sensitive Tubes (OSTs) 28
3.2.9 OST calibration and device fabrication 28
3.2.10 Animals and Dynamic Inhaled Gas Test (DIGT) 30
3.2.11 Histological examination 31
3.2.12 Quantification of vessel count/morphology 32

3.2.13 Statistical analysis 32
3.3 Results 33
3.3.1 Device evolution 33
3.3.2 *In vitro* islet viability 35
3.3.3 Lectin perfusion 36
3.3.4 Oxygen dynamics 38
3.4 Discussion 41
3.5 Conclusion 43
Chapter 4: Islet Transplantation within Sheet Devices 44
4.1 Introduction 44
4.2 Materials and methods 45
4.2.1 Animals 45
4.2.2 Prevascularized device implantation 46
4.2.3 Islet transplantation 46
4.2.4 Intraperitoneal Glucose Tolerance Test (IPGTT) 49
4.2.5 C-peptide measurements 49
4.2.6 Graft explantation and histology 49
4.2.7 Islet immunohistochemistry 51
4.2.8 Macrophage immunohistochemistry 52
4.2.9 Data display and statistics 52
4.2.10 Device modeling 52
4.3 Results 53
4.3.1 Experiment 1 53
4.3.2 Experiment 2 55
4.3.3 Experiment 3 58
4.3.4 Experiment 4 60
4.3.5 Experiment 5 64
4.3.6 Device modeling 70
4.4 Discussion 79
4.5 Conclusion 81
Chapter 5: Summary and Future Directions 83
5.1 Summary 83
5.2 Future Directions 84
Appendix 85
SolidWorks drawings 85
Modeling MATLAB code 89
References 95

List of Figures

Figure 1.1: Illustration of clinical islet transplantation into the portal vein.[7] 2

Figure 1.2: Illustration of the host response to encapsulated islet.[20] 3

Figure 1.3: Schematic of two-phase approach to islet transplantation. 5

Figure 1.4: The thin sheet macroencapsulation device. 6

Figure 2.1: Sheet fabrication, implantation, and explantation process. 8

Figure 2.2: H&E staining reveals vascularized and innervated tissue. 12

Figure 2.3: Immunohistochemistry detects both mature blood vessels and nerve tissue. 13

Figure 2.4: Quantification and comparison of vessel area, circularity, count, and area percentage 14

Figure 2.5: Quantification and comparison of nerve area, circularity, count, and area percentage 16

Figure 3.1: First generation islet loading and islet compression through the windows of the device. 25

Figure 3.2: Second generation islet loading. 26

Figure 3.3: Oxygen sensitive tube (OST) and device calibration. 29

Figure 3.4: Oxygen sensitive devices and implantation. 30

Figure 3.5: Device evolution. 34

Figure 3.6: Viability of SD rat islets. 35

Figure 3.7: Islet viability staining within PEEK braids. 36

Figure 3.8: Device vascularization and lectin staining. 37

Figure 3.9: Comparison of oxygen dynamics via DIGTs over 8 weeks of noninvasive monitoring. 39

Figure 3.10: Histological analysis of oxygen sensitive device slit tissue 8 weeks post implantation. 40

Figure 3.11: Vessel morphometrics and comparison to oxygen dynamics at day 56. .41

Figure 4.1: In vivo study set-up and groups. 46

Figure 4.2: Blood glucose profiles and IPGTT of first experiment of islet transplant recipients. 54

Figure 4.3: Blood glucose profiles of nude mice in second transplant study. 56

Figure 4.4: IPGTT results of second transplant experiment recipients. 58

Figure 4.5: Blood glucose values of four PV mice in third transplantation experiment. 59

Figure 4.6: Results from fourth islet transplant experiment. 61

Figure 4.7: Macrophage immunohistochemistry staining in device slit tissue. 63
Figure 4.8: Blood glucose profiles and blood C-peptide measurements in experiment 5 groups. 65
Figure 4.9: IPGTT results of fifth experiment. 67
Figure 4.10: Islet immunohistochemistry of pancreas and graft tissue from experiment 5 groups. 69
Figure 4.11: Maximum length estimation dependent on cell packing fraction *in vitro*. 72
Figure 4.12: Schematic of the device and outline of a repeating segment. 73
Figure 4.13: Resistance map for R_T with convection. 74
Figure 4.14: Glucose consumption rate in the device as a function of glucose concentration. 76
Figure 4.15: Tube surface glucose concentration as a function of blood glucose concentration. 77
Figure 4.16: Total insulin production by the device per time over varying glucose concentrations. 79
Figure A.1: Device mold design for *in vivo* oxygen sensing study. 85
Figure A.2: Device mold design for islet transplantation experiment 1 86
Figure A.3: Device mold design for islet transplant experiment 2 86
Figure A.4: Device floor mold design for islet transplant experiment 3. 87
Figure A.5: Device ceiling mold design for islet transplant experiment 3. 87
Figure A.6: Device floor mold design for islet transplant experiments 4-5. 88
Figure A.7: Device ceiling mold design for islet transplant experiments 4-5. 88

List of Tables

Table 4.1: List of primary antibodies used for IHC staining of explanted grafts. 50
Table 4.2: List of secondary antibodies used for IHC staining of explanted grafts 51
Table 4.3: Parameter values for analytical model. 70

List of Equations

Equation 4:1 Maximum spherical radius 71
Equation 4:2 Maximum cylindrical radius 71
Equation 4:3 Minimum blood vessel contact area 73
Equation 4:4 Mass transport coefficient 73
Equation 4:5 Resistance of features with symmetry in Cartesian coordinates 74
Equation 4:6 Resistance of convection 74
Equation 4:7 Available glucose consumption rate 75
Equation 4:8 Actual glucose consumption rate with a maximum cap 75
Equation 4:9 Rate of glucose consumption for the device 75
Equation 4:10 Glucose concentration at the islet tube surface 76
Equation 4:11 Glucose concentration within the islet tube 78
Equation 4:12 Hill function for rate of insulin production 78
Equation 4:13 Rate of insulin production for the device 78

Acknowledgements

Firstly, I would like to extend my deep gratitude to my advisor, Professor Elliot Botvinick, whose persistent support for me personally, emotionally, and academically has been unmatched by any other person in my professional career. His willingness to help and his positivity towards any situation has been a needed light in the journey that is a PhD. I thank him for his understanding and patience when guiding me and my projects.

My committee members, Professors Chris Hughes and Bernard Choi have been a wealth of knowledge, encouragement, and support during my dissertation work. I thank them for their willingness to help and give advice whenever I asked for it.

I would like to thank my mentors, in particular Dr. Bhupinder Shergill who started this project from the beginning and taught me everything I know today. His insight and calm demeanor was immensely beneficial to the project's progress. I extend my immense gratitude to Dr. Shiri Li, whose amazing technical skill in animal surgery made all of this work possible. Also, the senior BEAMS lab members including Drs. John Weidling, Abhishek Kurup, Shreyas Ravindranath, Mark Keating, Todd Thorson, and Avid Najdahmadi were so helpful in giving me advice over the years. I also thank the rest of the BEAMS lab for their thoughtful input and conversations and students Mellonie Zhang, Hannah Takasuka, Kimberly Stahovich, and Kendra Moore for their help with my work. Additionally, I thank Linda McCarthy and Ann Fain for their support in research and administrative matters. They went above and beyond to make sure that any issue that came up was resolved immediately.

Thank you to all my friends that have followed my journey and helped me to experience other things besides research. I am truly thankful for all of the memories we have made together.

I would like to thank Yan Kliaver for his love, support, and reassurance during my final PhD years. He has given me encouragement in times of uncertainty, happiness in times of sadness, and heartening in times of disappointment. Thank you for all that you did to help me. I cannot wait for what the future holds for us.

Most importantly, I thank my family, for all of their support throughout this process. Thank you for indulging me on my academic adventures and providing love whenever I needed it. My mother instilled a passion for learning in me as a young girl for which I am incredibly grateful. My sister has been the driving force for my desire to pursue research in type 1 diabetes. Her struggles keep me motived to engineer solutions. Thank you for providing me with inspiration and the motivation to do better.

Thank you to the publishers for granting permission to use copyrighted materials to support my dissertation. Permission granted by Copyright Clearance Center, Inc.

Lastly, I would like to thank my funding sources during my graduate career, which have helped me to focus on my research goals rather than worrying about finances. The Iacocca Foundation funded the early beginnings of this work, followed by a grant from the JDRF. The Biomedical Engineering Department at UC Irvine graciously funded my first year at UCI. The Whitaker International Program gave me the opportunity to do research abroad in the Netherlands. The NIH T32 Cardiovascular Applied Research and Entrepreneurship (CARE) program through the Edwards Lifesciences Center for Advanced Cardiovascular Technology gave me enhanced training that resulted in participation in the UCI Business Plan Competition. The School of Medicine Award received from this competition funded some of my dissertation work and led to the opportunity for a trip to Japan. In addition, the ARCS Foundation has been helpful in funding extra supplies and travel that have greatly added to my training. Professor Fadi Kurdahi, associate dean for graduate and professional studies, supported my fourth and fifth years in conjunction with the UCI Graduate Division under the direction of Professor Frances Leslie with Bridge funding. The UCI Graduate Division has been an essential supporter of my research work with the Diversity Recruitment Fellowship, the La Verne Noyes Fellowship, and the Public Impact Distinguished Fellowship. I sincerely enjoyed my trip with Dr. Leslie to the state capitol in Sacramento to advocate for graduate research.

I extend my deepest thanks to all of those who have supported my work.

Curriculum Vitae

Education

University of California, Irvine — Irvine, CA
PhD Biomedical Engineering, GPA: 3.98 — Sep 2019
MS Biomedical Engineering — Dec 2017

University of California, Davis — Davis, CA
BS Biomedical Engineering, GPA: 3.63 — Jun 2014

Research Experience

UC Irvine – Elliot Botvinick (BEAMS) Lab — Irvine, CA
Graduate Researcher — Aug 2014–Aug 2019

- Designed and developed prototype implantable bioartificial pancreas device for islet transplantation within a 3D print-assisted housing and tested functionality in a preclinical mouse model
- Mentored 2 undergraduate and 2 high school students, gave 3 poster and 3 oral presentation, served as safety on site representative, and received part of a $1.3 million JDRF grant for research support

JDRF (formerly Juvenile Diabetes Research Foundation) — New York, NY
Summer Research Intern (paid position) — Aug 2018–Sep 2018

- Interviewed 15 current bioprinting leaders to isolate best approaches/biomaterials for beta cell replacement therapies which led to an in-person workshop

University of Groningen – Paul de Vos Lab — Groningen, Netherlands
Visiting Graduate Researcher, Whitaker Program — Jun 2015–Aug 2015

- Interpreted tissue response to hard material implants via resin histology

UC Davis – Alexander Revzin Lab — Davis, CA
Undergraduate Research Assistant — Jan 2014–Jun 2014

- Tested a microfluidic device for analyzing cell secretions during the rescue process between melanoma two cells lines, resistant and susceptible, to a drug

UC San Francisco – Shuvo Roy Lab — San Francisco, CA
Summer Research Training Program (SRTP) Researcher — Jun 2013–Jul 2013

- Quantified the strength and hydraulic permeability of Silicon Nanopore Membranes (SNMs) under variable pressure conditions using automated flow cell systems; funding provided NSF-REU

UC Davis – Soichiro Yamada Lab — Davis, CA

Undergraduate Researcher — Apr 2012–Jun 2013

- Created a confocal microscope-compatible cell-stretching device to analyze zyxin, a focal adhesion protein, and its recruitment during cyclic force application in real time

Leadership and Activities

Graduate Association of BME Students (GABES) — Irvine, CA

Member — Jun 2015–Aug 2019

President – Internal — May 2017–May 2018

- Connected alumni and industry leaders to UCI BME grad students through 30+ events (alumni night, industry tours), hosted students during visitation weekend, and managed 7 officer members
- Created and held 10+ science outreach demos

Co-Founder, Treasurer — Jan 2015–Apr 2017

- Established organization and managed budget for weekly events

COSMOS (California State Summer School for Math and Science) Program

UC Irvine — Irvine, CA

Cluster 6 Presenter – Biomedical Sciences — Jul 2016/17/18/19

- Created and taught a microfluidics hands-on activity and presented my research to 25 high school students

UC San Diego — San Diego, CA

Cluster 7 Participant – Bioengineering — Jun 2008–Jul 2008

- Performed wet lab techniques and analyzed mechanics of the red blood cell as a group project and won second place for poster
- Received scholarship ($2,500) to participate

Teaching Assistant — Irvine, CA

BME 160, Tissue Engineering — Sep 2017–Dec 2017

- Explained class concepts, led discussion sections, performed grading duties, and taught one lecture to 90 students

Graduate Student Lead — Irvine, CA

Pathways to Biophotonics and BME (PBBE) Program — Jun 2017/18–Aug 2017/18

- Hosted poster workshop and organized social activities for 20 visiting summer undergraduate students from HBCUs (historically black college and universities)

Women and Minorities in STEM Mentorship Program — Irvine, CA
Mentee: Adrienne Lee — Feb 2017–Aug 2019

- Met with undergraduate student monthly to provide graduate/career tips

Biomedical Engineering Society (BMES) — Davis, CA
Member — Sep 2011–Present
Vice President – Outreach — Jul 2013–Jun 2014

- Planned and executed 40+ weekly events such as lunches with faculty, lab tours, alumni presentations, and symposiums
- Led an Outreach committee of 10 people for volunteering/school events

Treasurer — Sep 2012–Jun 2013

- Managed $3,000 budget for weekly events including reimbursement/ fundraising

Engineering Joint Council (EJC) Representative — Sep 2011–Jun 2012

- Collaborated with EJC/BESA (grad group) to hold joint events, graduate panels, and research fair

Delta Gamma Sorority, Delta Chi Chapter — Davis, CA
Member — Sep 2012–Present

- Performed community service for the foundation, Service for Sight, participated in sisterhood events, tutored members, and attended weekly meetings

Tau Beta Pi, National Engineering Honor Society — Davis, CA
Member — Sep 2012–Present

- Tutored students and attended weekly events

General and Organic Chemistry Tutor (paid position) — Davis, CA
Student Academic Success Center — Sep 2011–Jun 2014

- Taught 100+ students chemistry concepts by using a participatory approach in individual and group settings while enabling them to work independently

Awards

BME Graduate Student of the Year — Feb 2018
Outstanding TAs nominated by undergrads of the Engineering Student Council are honored at the annual Engineering Awards Banquet

La Verne Noyes Fellowship ($3,000) — Jan 2018
Provides financial support to students who demonstrate outstanding past academic achievement and are descendants of World War I US Army or Navy Veterans

Public Impact Distinguished Fellowship ($12,000) Nov 2017
Highlights 4 doctoral students at UCI whose current research has the potential for substantial impact in the public sphere

ARCS Foundation Scholar Award ($10,000) Sep 2017
Recognizes 10 (2 in engineering) academically superior doctoral students per year at UCI with outstanding promise as scientists

Best Entrepreneur Award, Global Science Week Sep 2016
Winner of international bioentrepreneurship pitch competition against 4 other countries

School of Medicine Award ($10,000), UC Irvine Business Plan Competition May 2016
Prize given to our mock company, Sher Biomedical, over 11 other teams to support research of medical technologies

CARE Fellowship May 2015
Cardiovascular Applied Research and Entrepreneurship NIH T32 Program
Training program and full funding for 2 years for a small number of PhD students who can produce impactful research in cardiovascular science and technology

Whitaker International Summer Grant ($10,000) May 2015
Summer award for biomedical engineers to travel abroad to perform high-quality, individually arranged, research at an international university

Mazda Foundation Scholarship ($10,000) Apr 2015
Awards 2 engineering PhD students based on academic excellence and financial need

UC Irvine Diversity Recruitment Fellowship ($5,000) Mar 2014

National Science Foundation Mar 2014
Graduate Research Fellowship Program – Honorable Mention

Undergraduate Leadership Award, UC Davis BME Dept Jun 2014

Best Senior Design Award, UC Davis BME Dept Jun 2014

Outstanding Mentor Program Award, BMES Jun 2014

Outstanding Achievement Award, BMES Sep 2013

Commendable Achievement Award, BMES Oct 2012

UC Davis Dean's Honor List 5 quarters (2010-2013)

Publications

2. Thorson TJ, **Gurlin RE**, Botvinick EL, Mohraz A. Bijel-templated implantable biomaterials for enhancing tissue integration and vascularization. *Acta Biomater.* 2019; 94: 173-182.

1. **Gurlin RE**, Keating MT, Li S, Lakey JRT, de Feraudy S, Shergill BS, Botvinick EL. Vascularization and innervation of slits within polydimethylsiloxane sheets in the subcutaneous space of athymic nude mice. *J Tissue Eng.* 2017; 8: 204173141769164

Presentations

Graduate Research Advocacy Day — Sacramento, CA
Represented the University of California advocating for continued funding of graduate research by presenting to California lawmakers — Mar 2018

JDRF Orange County Local Chapter Research Update — Newport Beach, CA
Presented recent research findings to chapter members (mainly type 1 diabetics and families) — Feb 2018

UC Los Angeles Bioengineering Symposium — Los Angeles, CA
Poster Presentation, Two Phase Implantation of Pancreatic Islets Via a Skin Integrated Sheet — Jul 2017

University of Tsukuba, Japan, Global Science Week — Tsukuba, Japan
Oral Presentation, Sher Biomedical – fearless in the fight for better diabetes treatment — Sep 2016

UC Irvine Institute for Clinical Translational Science (ICTS) Research Day — Irvine, CA
Poster Presentation, Two Phase Approach to Beta Cell Replacement Tissue Transplantation — Jun 2016

UC Irvine Business Plan Competition — Irvine, CA
Oral Presentation, Sher Biomedical – fearless in the fight for better diabetes treatment — May 2016

UC Davis Senior Design Symposium and Engineering Design Showcase — Davis, CA
Oral/Poster Presentations, CORE (Cadaver Organ Retrieval) Biopsy Device — Jun 2014

- Manufactured multiple organ biopsy device for use with digital autopsy

BMES Annual Meeting — Seattle, WA
Best Practices Oral Presentation and Panel — Sep 2013

Summer Research Training Program Symposium	San Francisco, CA
Oral/Poster Presentations, Silicon Nanopore Membrane Characterization Using Automated Flow Cell Instrumentation	Jul 2013
BMES Annual Meeting	Atlanta, GA
Best Practices Oral Presentation	Oct 2012
24^{th} Annual Undergraduate Research Conference	Davis, CA
Oral Presentation, The Analysis of Force-Dependent Zyxin Recruitment in Epithelial Cells	Apr 2013

Abstract

A skin integrated sheet device for pancreatic islet transplantation

by

Rachel Ellyn Gurlin

Doctor of Philosophy in Biomedical Engineering

University of California, Irvine, 2019

Professor Elliot Botvinick, Chair

An estimated 1.25 million Americans suffer from type 1 diabetes (T1D), an incurable autoimmune disease with increasing prevalence. Currently, patients manage their disease with combined insulin administration via injection or pump and blood glucose monitoring. For severe cases, pancreatic islet transplantation into the liver via the portal vein has shown to increase patient quality of life; however, this procedure comes with many risks and potential morbidities making it unsuitable for a majority of the T1D population. A bioartificial pancreas provides an attractive advantage over current treatment methods by allowing "hands-free" glucose control mediated by pancreatic islets.

We developed a two-phase approach to islet transplantation with a thin-sheet device perfused by the host vasculature prior to islet introduction. In phase one, the host develops new tissue within the device that is fully integrated into the subcutaneous space, demonstrated by infiltration of mature vasculature via both lectin perfusion and histology as well as nerve tissue via histology. Noninvasive *in vivo* oxygen dynamics measurements indicate shorter prevascularization periods may be more beneficial. In phase two, we infuse islets with a newly developed loading method into a single file configuration within the device channels such that they are immediately adjacent to host vasculature. Prototype devices were fabricated, modified, and tested in diabetic athymic nude mice. Devices were allowed to vascularize and then re-accessed to load islets *in situ*. Intraperitoneal glucose tolerance tests, C-peptide measurements, nonfasting blood glucose values, and

immunohistochemistry staining results indicate islets transplanted into devices maintain partial function and in a few cases, euglycemia. Device modeling with *in vivo* perfusion conditions indicates the islet packing fraction and level of perfusion majorly contribute to insulin production by the device and could explain differences in glycemic control.

Chapter 1: Introduction

1.1 Type 1 diabetes

Type 1 diabetes (T1D) is an autoimmune disorder characterized by the destruction of the beta cells within the pancreas.[1] Without these vital cells, insulin cannot be produced to maintain normal blood glucose levels. In the United States, an estimated 1.25 million people are living with T1D and another 40,000 people are diagnosed every year.[2] Currently, patients require intensive insulin therapy and regular glucose monitoring to maintain glycemic control and reduce their risk for microvascular complications such as retinopathy, nephropathy, and neuropathy.[3] Despite technology improvements such as continuous glucose monitoring[4] and closed loop systems,[5] less than one-third of type 1 diabetic patients are achieving target blood glucose levels.[2] T1D poses a major burden not only on individual patients to constantly manage their disease, but also on the healthcare system where long-term complications of the disease contribute to high costs.[6]

1.2 Islet transplantation

Many approaches to alleviating T1D are under investigation, including clinical pancreatic islet transplantation.[7] Ranging in size from 50-500 μm, islets can be isolated from a donor via collagenase digestion and density gradient purification.[8] Islets of Langerhans are clusters of cells that produce multiple hormones including glucagon (α-cell), insulin (β-cell), pancreatic polypeptide (γ-cell), somatostatin (δ-cell) and ghrelin (ε-cell).[9] In the Edmonton Protocol pioneered by Shapiro and Lakey,[10] donor islets are transplanted into the hepatic portal vein (Figure 1.1) to achieve insulin independence and greater glucose control.[11] While this breakthrough procedure provided a treatment option for those with brittle diabetes, the challenges of lifelong immunosuppression, lack of donor organs, and short graft life prevent this approach from becoming widely available.[12] At best, insulin independence rates of 50% after 5 years post-transplant can be achieved at some experienced centers,[8] necessitating improvements in islet transplantation.

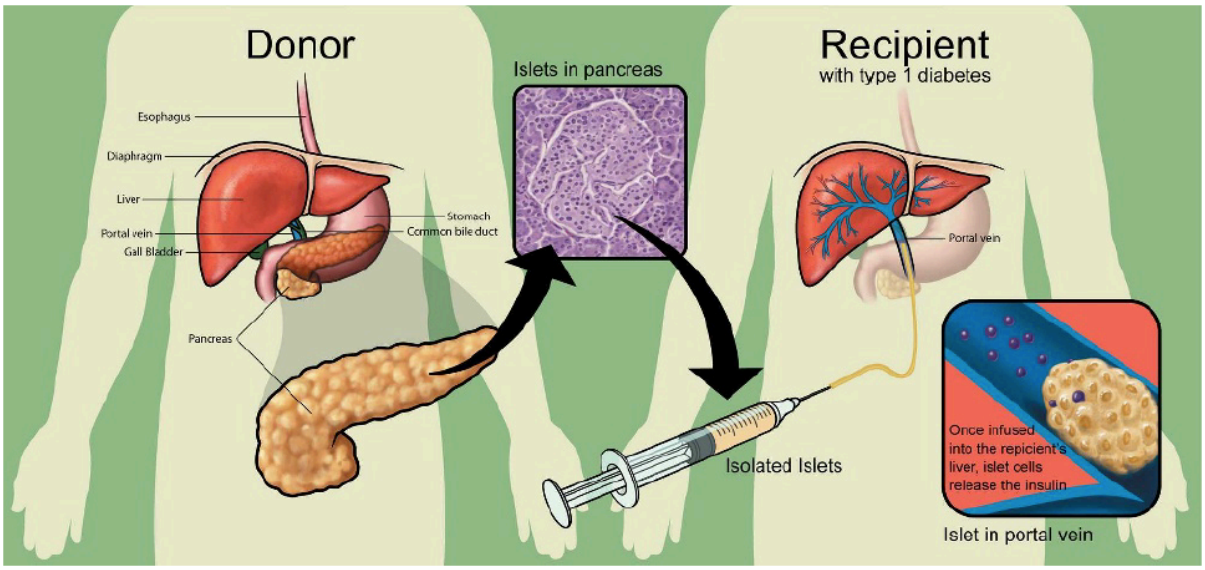

Figure 1.1: Illustration of clinical islet transplantation into the portal vein.[7]
Islets from a donor pancreas can be isolated via collagenase digestion and density gradient purification and transplanted into the portal vein. Islets lodged in the hepatic capillaries sense glucose and secrete insulin.

1.3 Islet encapsulation

As an alternative to intraportal islet transplantation, islet encapsulation methods are categorized by three types: microencapsulation, macroencapsulation, and intravascular devices.[13] The most popular and extensively studied method of islet transplantation involves the microencapsulation of islets within an alginate membrane, (Figure 1.2) first performed by Lim and Sun in 1980.[14] Derived from seaweed, alginate capsules provide immunoisolation via a selectively permeable membrane that allows small molecular weight molecules (e.g. glucose, insulin) to pass through, but prevents large molecular weight molecules (e.g. antibodies) from entering the encapsulated cells.[15] Ongoing work strives to improve the biocompatibility of alginate capsules by removing impurities and incorporating various chemicals for increased mechanical strength.[16,17] Alginate encapsulation or other microencapsulation methods,[18] can be transplanted into the host; however, it can take days to weeks for new blood vessels to form (Figure 1.2), potentially leaving the metabolically active islets without the required oxygen they need to survive.[19]

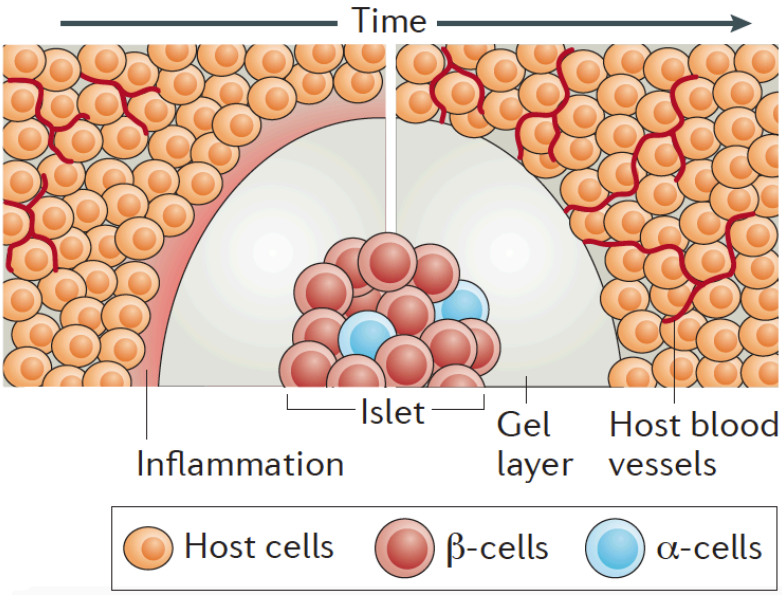

Figure 1.2: Illustration of the host response to encapsulated islet.[20]
After transplantation, the host tissue surrounds the alginate capsule with in an initial inflammatory response. Over time, the inflammation resolves and host blood vessels eventually reach the capsule surface.

With macroencapsulation, a similar problem exists. Islets are aggregated into a relatively large device, potentially leaving them to compete for resources.[21] Hypoxia, or lack of sufficient oxygen, plagues a majority of macroencapsulation devices.[22] Prevascularization can offset the deficit in oxygen sources,[23] which has been accomplished via the implantation of an array of cylindrical rods supported by a polymer mesh and subsequent removal of the rods for islet infusion.[24,25] This approach, labeled the Cell Pouch System™, has been commercialized by Sernova Corp. and is currently under clinical trial investigation (ClinicalTrials.gov Identifier: NCT01652911).[26] Reports mention that the rods are about 3 mm in diameter,[27] which may still be too large to avoid islet aggregation and mass transport limitations. In the native pancreas, islets are highly vascularized and beta cells form rosette-like structures around blood vessels;[28–30] yet, it is unknown to what degree this form needs to be recapitulated for transplanted islets. Critics of the Cell Pouch System™ approach suggest that a quantitative understanding of the degree of neovascularization and cell viability and function needs to be attained in order for implantable devices to achieve success.[27]

1.4 Subcutaneous transplantation site

Numerous problems with portal vein islet transplantation such as instant blood-mediated inflammatory reaction (IBMIR), large doses of immunosuppression drugs, and thrombosis risk have lead researchers to investigate alternative islet transplant sites.[31] The subcutaneous space is an attractive transplant site because it provides ease of infusion, imaging, and retrieval with minimal surgical risk.[32] In addition, it has the potential to support a clinically-relevant volume of tissue capacity. However, islets alone transplanted into an unmodified subcutaneous space (in mice and rats) does not restore euglycemia.[33,34] It is thought that poor oxygen tension and lack of blood supply in the native subcutaneous tissue contribute to poor islet engraftment.[35] Investigators are working towards a variety of biomaterials and angiogenesis approaches including fibrin gel,[36–39] poly (D,L-lactide-co-ε-caprolactone) PDLLCL,[40] and polyethylene glycol (PEG)[41–43] scaffolds, collagen modules with embedded endothelial cells,[44] catheter introduction and removal,[34] fibroblast growth factor (FGF)[38,45–47] or vascular endothelial growth factor (VEGF) and platelet derived growth factor (PDGF) administration,[39] coculturing with mesenchymal stromal and endothelial cells,[48] or adipose-derived stem cells,[38] and more[31] to improve islet vascularization in the subcutaneous space. There is a consensus that establishing a sufficiently vascularized environment while minimizing immunogenicity and fibrosis will be essential in the success of subcutaneously implanted macrodevices.

1.5 Summary and approach

In order to address some of the challenges seen in islet transplantation, this research focuses on development of a subcutaneously implanted macroencapsulation device via a two-phase approach. The first phase involves the implantation of a thin sheet microfluidic device into the subcutaneous space in which the host tissue integrates, creating a prevascularized environment (Figure 1.3). Due to slits that are cut through the device, vessel growth is permitted into the thickness of the sheet. At a later time period, the islets are loaded within the device in a single file configuration, producing minimal islet aggregation and confining them into a

predefined geometry in which they are immediately positioned adjacent to host vasculature (Figure 1.3). If necessary, islets can be retrieved and replaced with new cells without disturbing the established vasculature or entire device excision. For scalability, sheets can be stacked on top of each other to create larger cell dosages without compromising vasculature proximity or increasing device footprint. Taken together, these key components are postulated to improve islet survival.

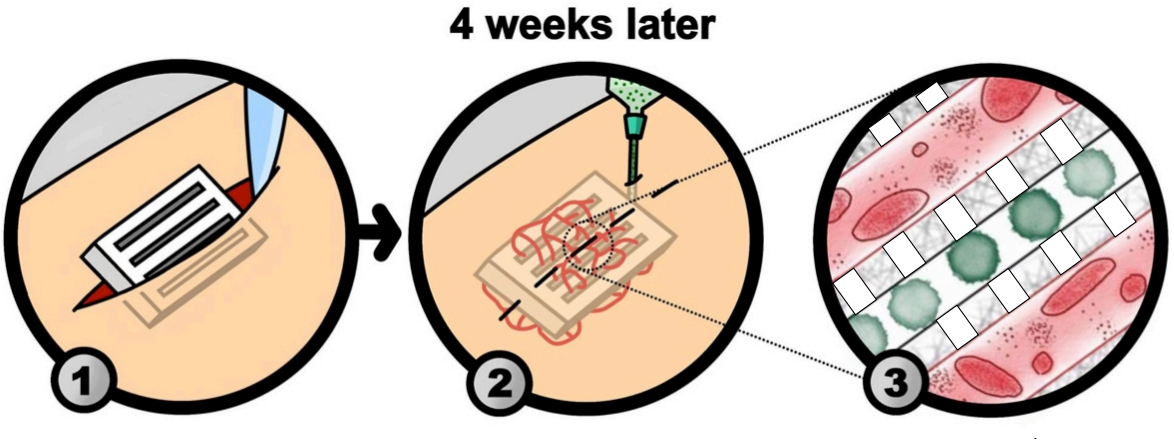

Figure 1.3: Schematic of two-phase approach to islet transplantation.
The device is first implanted under the skin (subcutaneous site) and allowed to integrate with the host tissue. Then, islets (green) can be infused into the device channels. Islets are close to through-cut slits (red) where the host tissue has vascularized the space.

A bioartificial pancreas can be likened to a housing community: the infrastructure is the organ and the people living in the community are the islets of Langerhans. The homeowners cannot move into the community before the infrastructure is complete. In the same way, islets cannot live in a microenvironment that is not equipped with proper oxygen, nutrient sources, and waste removal.

The device comprises a thin (~1 mm), non-degradable flexible sheet through which a series of slits are cut (Figure 1.4A, top). Important to the design, initially conceived by previous lab members: Shergill et al,[49] multiple sheets can be stacked (Figure 1.4A, bottom) and remain vascularized because host vasculature can pass through each sheet. In addition to the slits, a parallel array of microchannels are formed within the thickness of each sheet as illustrated in Figure 4B. The slits allow for vasculature (red) while the channels (green) allow for the filling of islets. The channels can be tuned to thickness t to assemble the islets in a single file

configuration. This arrangement is critical to prevent islet aggregation and mass transport limitations. Additionally, the channels can be flushed or aspirated without disturbing the local vascularized environment for retransplantation of new cells if necessary. This research aims to assess the feasibility of such a macroencapsulation device for the transplantation of islets within the subcutaneous space for the treatment of type 1 diabetes.

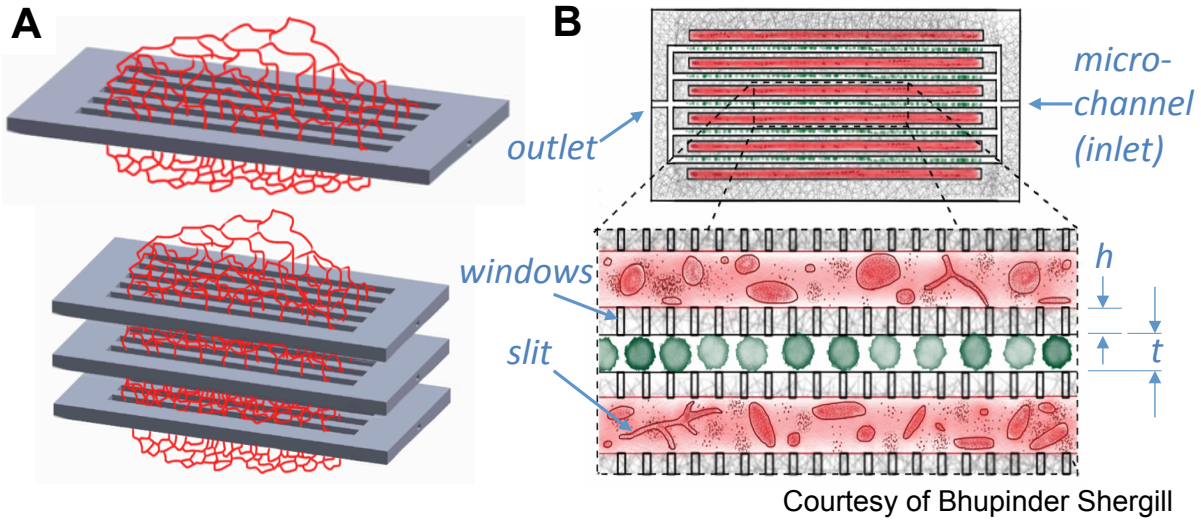

Figure 1.4: The thin sheet macroencapsulation device.
(A) The device comprises one or more sheets that are stackable and contain aligned slits passing through each layer. Host tissue infiltrates these slits. (B) Macro (top) and magnified (bottom) illustrated views of a longitudinal section through the mid-plane of a single sheet. Vascularized host tissue (red) passes through the slits, which are adjacent to flushable microchannels housing pancreatic islets in single file (green). Slits and channels are separated by a wall of thickness h that is perforated with windows to allow the passage of nutrients and waste.

Chapter 2: Slit Sheet Vascularization

2.1 Introduction

To investigate if the slit architecture can provide a vascularized environment for later cell transplantation, we implanted thin PDMS sheets of varying slit widths (150, 300, 500, and 1500 μm) in the subcutaneous space of athymic nude mice and examined the tissue response. This chapter is adapted from the published version.[50]

Vascularization of scaffolds and implanted materials has been a major topic of study in the field of tissue engineering for the past several decades.[51,52] Notably, cell therapies, in which autologous or foreign tissues are transplanted, are emerging as complementary or replacement options to a myriad of ailments and diseases. One promising approach is to embed these cells within a three-dimensional (3D) scaffold, which can provide mechanical support and potentially access to the host vasculature for exchange of oxygen, carbon dioxide, metabolites, and waste. Considerable advances have been made to promote invasion of the host vasculature into these scaffolds in an effort to improve cell viability and function. Many groups have investigated various approaches such as the use of proangiogenic factors, progenitor cells, vascular-inductive biomaterials, bioreactors, microelectromechanical system (MEMS)-related approaches, and combinations of these methods to promote neovascularization and angiogenesis.[53,54] Important to our study, others have shown that the geometry of an implant, and not chemical factors alone, also plays a role in forming vascular networks.[55–57]

Polydimethylsiloxane (PDMS) has long been used for medical device implants in addition to creating tissues,[58] promoting vessel growth,[59,60] and regenerating nerves[61] *in vivo*. PDMS is considered to be biocompatible and has other advantages such as low cost, optical transparency, flexibility, and durability. PDMS is a good candidate material for tissue engineering strategies that require biocompatibility and non-resorption over time. On the other hand, physical geometries and shapes, mainly microchannels, have also been used to encourage vascularization[41,55,57,62,63] and nerve growth[63–66] *in vivo*. We investigate if this biocompatible material cast into thin sheet

containing rectangular slits can promote healthy tissue growth in the subcutaneous space.

2.2 Materials and methods

2.2.1 Sheet fabrication

Thin sheets of PDMS (Sylgard 184 Silicone Elastomer Kit, Dow Corning Corp.), each containing a parallel array of slits of approximately equal width (150, 300, 500, or 1500 µm), were fabricated by polymerization within a custom mold. Molds were designed in SolidWorks, exported to an STL file, and printed by a high-resolution stereolithography 3D printer (Pico Plus 27, Asiga). The mold was made of a hard 405-nm light curable resin (PlasCLEAR, Asiga), with x- and y-resolutions of 27 µm, and fabricated layer-by-layer in 10-µm-thick slices (Figure 2.1A). After the build was finished, molds were washed 3× in isopropanol and sonicated for 10 min. Molds were air dried for 15 min, further cured by 10 min exposure to an 8W 302 nm UV light source (Dual UV Transilluminator, VWR), and subsequently baked in an oven

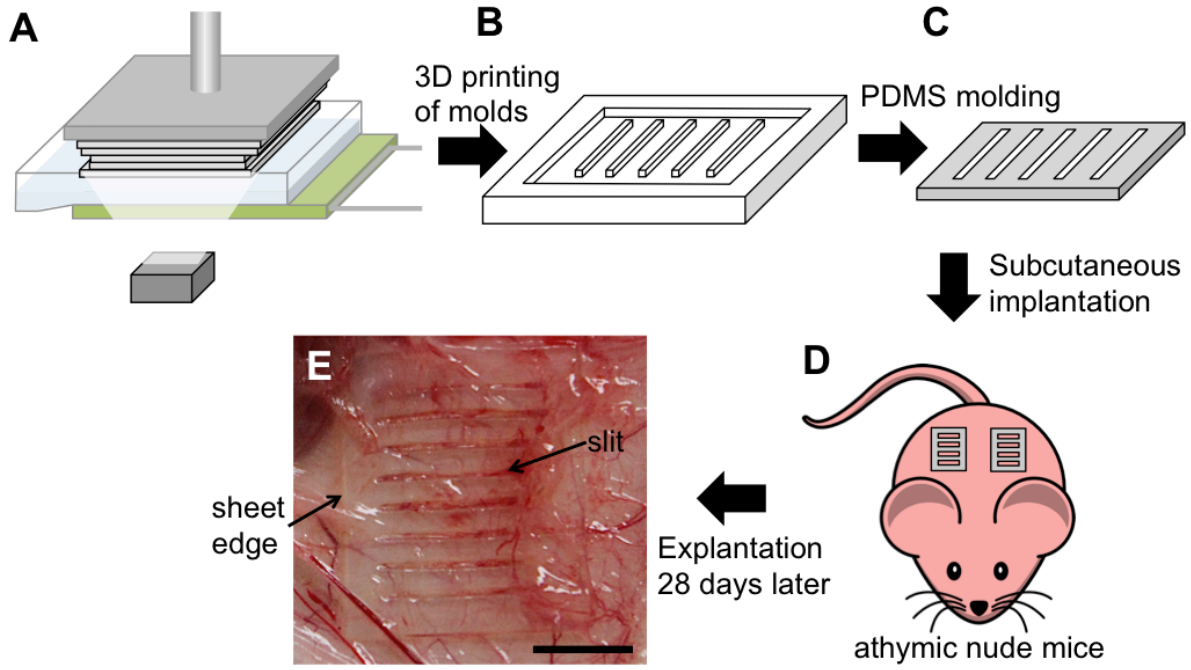

Figure 2.1: Sheet fabrication, implantation, and explantation process.
(A) A micro-stereolithographic 3D printer creates molds layer by layer. (B) Molds are filled with PDMS to create the sheet implants (C) with various slit widths. (D) Two sheets are implanted into the subcutaneous space of each athymic nude mouse. (E) At 28 days, the skin flap shows vessel infiltration around the 500 µm slit size implant, scale bar: 5 mm.

overnight at 80°C. Finally, liquid PDMS (1:10 ratio of crosslinker to monomer base) was poured into the molds and baked at 80°C for 2 h (Figure 2.1B). The polymerized thin sheets (Figure 2.1C) were removed from the molds and autoclaved at 122°C for 20 min. All sheets had planar dimensions of approximately 14 mm x 22 mm and thickness 0.5 mm. Slits were placed such that the space between neighboring slit edges was 1 mm.

2.2.2 *In vivo* study

Approximately 8-week-old male athymic nude mice (Charles River Laboratories) weighing between 20 and 25 g were used in this study. All procedures were approved by the UC Irvine Institutional Animal Care and Use Committee (IACUC #2008-2850). Animals were anesthetized with 2%–4% isoflurane for surgical experiments. A midline incision through the dorsal skin was created via sterile surgical scissors and two subcutaneous pockets were created by blunt dissection, one on the left and one of the right side of the incision. A single sheet was placed within each pocket (Figure 2.1D), and then a drop of blood (5–10 μL) from a donor mouse was spread across the upper surface of the sheet (in situ) in order to fill the slits with clotted blood.[67,68] The pocket on the left side was sealed by sutures running between the bottom layer of subcutaneous tissue and the underlying muscle layer to prevent the sheets from shifting and overlapping each other. The dorsal incision was sutured closed and secured with surgical clips. The animals received ibuprofen, between 50 and 80 mg/kg, via drinking water for 2 days following surgery. Five animals were studied in each slit width group (150, 300, 500, and 1500 μm). Animals were monitored daily and after 28 days sheets were removed (Figure 2.1E) and animals were sacrificed.

2.2.3 Histological preparation

Sheets were removed on day 28 by cutting through the full thickness of surrounding skin while leaving the tissue above and below the sheet intact. The excised tissue was immediately fixed by submersion in a 4% solution of phosphate-

buffered formalin for 24 h. Samples were placed and sectioned in one of two orientations (Figure 2.2A and B). For each slit width, four sheets were placed for horizontal sectioning and one sheet for vertical sectioning. Vertical samples were prepared by first cutting the sheets with a trimming knife (Cancer Diagnostics) through their center in a direction transverse to the long axis of the slits and then transferring each half sheet into cassettes. Samples were processed and embedded within a paraffin block with the cut end facing the surface of the block (by Harris Histology Services, Tustin, CA, USA) and sectioned (Figure 2.2A). Horizontal samples were prepared by first cutting the sheets along the long axis of the center slit and then transferring each sheet half into cassettes. Samples were processed and blocked in paraffin wax with one half of the cut sheet with the skin facing the surface of the block and the other half with the muscle facing the surface of the block, side by side in one block (by Harris Histology Services) and sectioned (Figure 2.2B). Serial sections were cut (5 μm thickness) and mounted onto slides.

2.2.4 Histological staining

For histological observations, sections were stained with H&E. For immunohistochemistry, sections were deparaffinized followed by antigen retrieval via overnight incubation in 0.1 M Tris/HCl buffer, pH = 9.0 at 80°C.[69] Sections were then washed with phosphate-buffered saline (PBS), permeabilized with 0.5% Triton X-100, and blocked with 5% Donkey serum (Jackson ImmunoResearch) for 30 min at room temperature. After serum blocking, slides were incubated with 1:200 monoclonal rabbit anti-alpha smooth muscle actin (αSMA) (Abcam) in 1× PBS supplemented with 5% Donkey serum and 0.5% Triton X-100 at 4°C overnight. Detection of peripheral nerve axons was performed with incubation of 1:400 polyclonal rabbit anti-S100 (Dako). Slides were then washed with PBS and incubated with 1:500 AlexaFluor® 488 donkey anti-rabbit (Life Technologies). Images were taken on an Olympus IX-83 microscope at 20× with an Orca R2 camera (Hamamatsu) through Micro Manager.[70]

2.2.5 Quantification of vessel and nerve count/morphology

For analysis, H&E slides were imaged with a Nikon eclipse E800 microscope at 20× using Olympus cellSens Entry program. Images that contained vessels or nerve axons on multiple adjacent images were stitched together using Adobe Photoshop. At least three slits were imaged for each slit size group. Images (or stitched images) for each slit were analyzed with a custom MATLAB code for manual tracing of blood vessels and nerve tissue within each image and calculations of area and lengths of major and minor axes of the tracings. Vessels were identified by three criteria: (1) hollow lumen, (2) endothelial cell lining, and (3) luminal erythrocytes.[71,72] Nerve axonal tissue was identified by characteristic morphology: wavy bundles of eosinophilic fibers associated with spindled Schwann cells. Identifications and tracings were confirmed by a blinded dermatopathologist. The vessel (or nerve) area percentage or count was calculated as total vessel (or nerve) area or count divided by total slit tissue area. Circularity of vessels (or nerves) was defined as the length of the minor axis divided by the length of the major axis.

2.2.6 Statistical analysis

GraphPad Prism 6 was used for graphing and statistical testing. Data did not pass tests for normality necessitating non-parametric Kruskal–Wallis tests followed by post hoc Dunn's multiple comparisons test. Tests were determined statistically significant when $p<0.05$. Vertical and horizontal section data were analyzed separately. Data represented by box plots show the median, IQR (interquartile range), and maximum and minimum values or 1.5IQR, whichever is shorter. Data represented by bar plots show the median±IQR.

2.3 Results

Sheets were fabricated and implanted in pairs in the subcutaneous space along the back of male nude mice (Figure 2.1D). Animals tolerated the implants well, showing no changes in eating habits or signs of discomfort. No adverse reactions such as infection or necrosis were observed out to 28 days post-implantation. Digital

photographs of sheets during explantation indicated local vascularization. Note that vessels can be resolved through the transparent sheet indicating the lack of thick fibrotic and opaque tissue at the sheet surface (Figure 2.1E). H&E staining of both vertical (Figure 2.2A, C–J) and horizontal (Figure 2.2B, K–N) sections showed host tissue infiltration within the slit space including erythrocyte-filled blood vessels and nerve tissue. On vertical sections through the larger slits (300, 500, and 1500 µm), the upper and lower region of each slit contains vessels, nerves, connective tissue, and muscle, suggesting that mouse superior and inferior dermis have squeezed into the larger slits (Figure 2.2D–F, H–J). Tissue within all slits exhibits a foreign body response comprising macrophages and multi-nucleated giant cells in contact with the material edges.

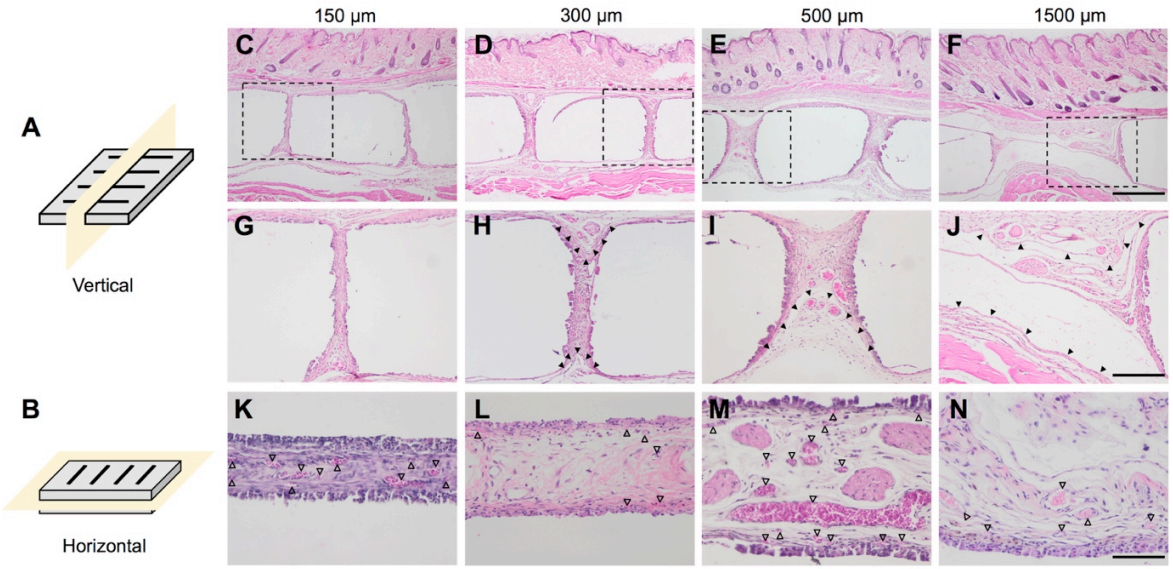

Figure 2.2: H&E staining reveals vascularized and innervated tissue.
Samples were cut either in a vertical orientation (A) or in a horizontal orientation (B). Histological images post 28 days implantation into the subcutaneous space of athymic nude mice are shown for each slit width: (C, G, K) 150 µm, (D, H, L) 300 µm, (E, I, M) 500 µm, and (F, J, N) 1500 µm. Vertical sections at 4× magnification (C–F) are marked with a dashed rectangle, which were imaged again at 10× magnification (G–J). Arrows point to what appears to be invagination of native tissue into the slit space. Horizontal sections are shown in (K–N) at 20× magnification. Hollowed arrows point to erythrocyte-filled blood vessels. Scale bars: (C–F): 500 µm; (G–J): 200 µm; (K–N): 100 µm.

The presence of mature vessels (Figure 2.3A) and Schwann cells (Figure 2.3B) was confirmed by immunohistochemistry staining for αSMA (Figure 2.3C) and S100[73] (Figure 2.3D), respectively.

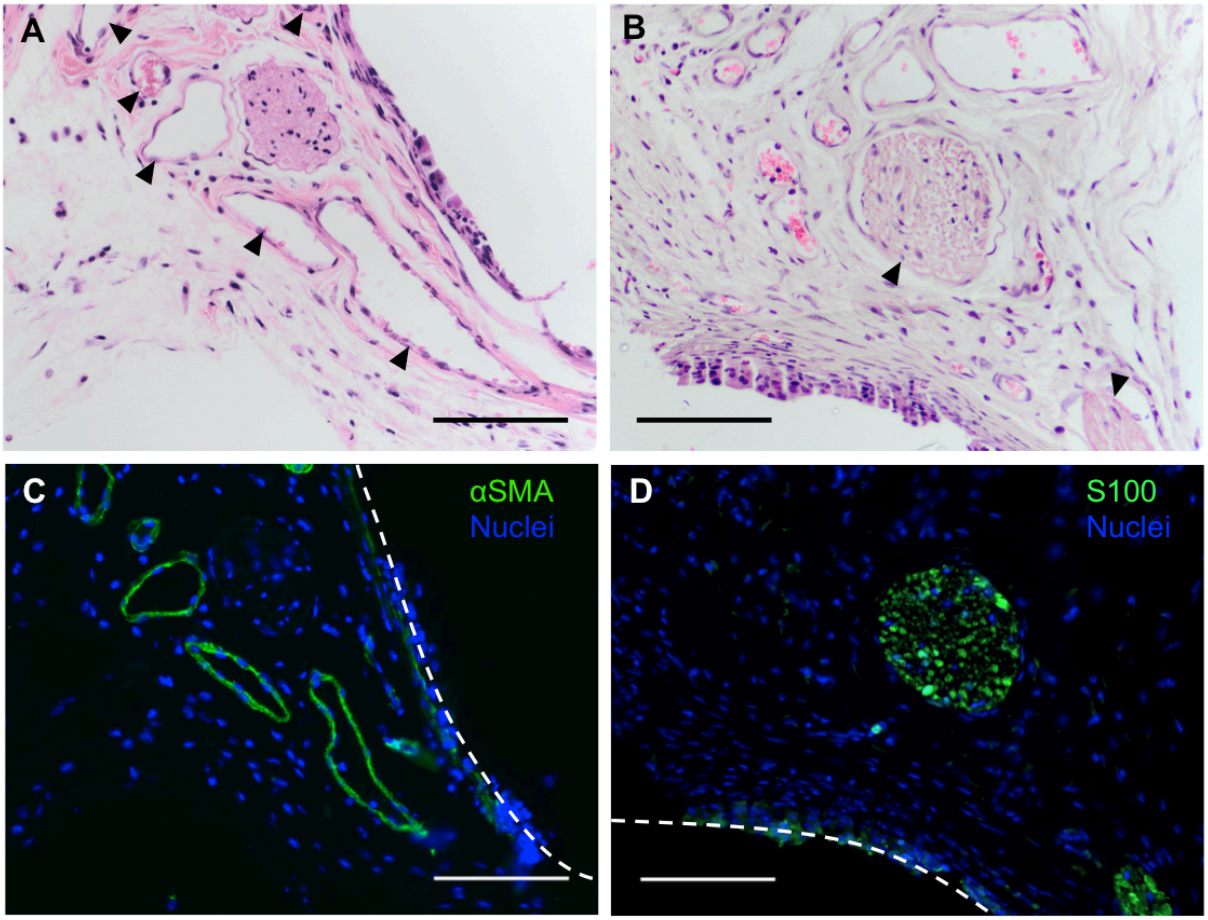

Figure 2.3: Immunohistochemistry detects both mature blood vessels and nerve tissue. Vertical sections of 500 μm slit samples were stained with H&E where arrows indicate (A) blood vessels or (B) nerves. The presence of (C) mature blood vessels via αSMA and (D) nerve via S100 were confirmed with immunohistochemistry of serial sections. Dashed white lines indicate the border of the material and tissue interface. Scale bar=100 μm.

Examination of all detected vessels in horizontal slices shows that tissue within the 1500 μm slits contains vessels with larger cross-sectional area as compared to the other groups (Figure 2.4A), and vessels within the 500 μm slits were of significantly smaller area as compared to the other groups. While differences in area were statistically significant, the physiological implications may be subtle, and absolute values of vessel area are consistent with other studies on vascularization of scaffolds.[72,74] No statistically significant differences in vessel area were found for vertical sections. Similarly, when investigating vessel circularity (Figure 2.4B) across all detected vessels in horizontal slices, we found that the 1500 μm slits contained vessels of greater circularity as compared to the other groups. In interpretation of

circularity, it should be considered that circularity is dependent not only on vessel shape but also on the orientation of the vessel relative to the plane of sectioning.

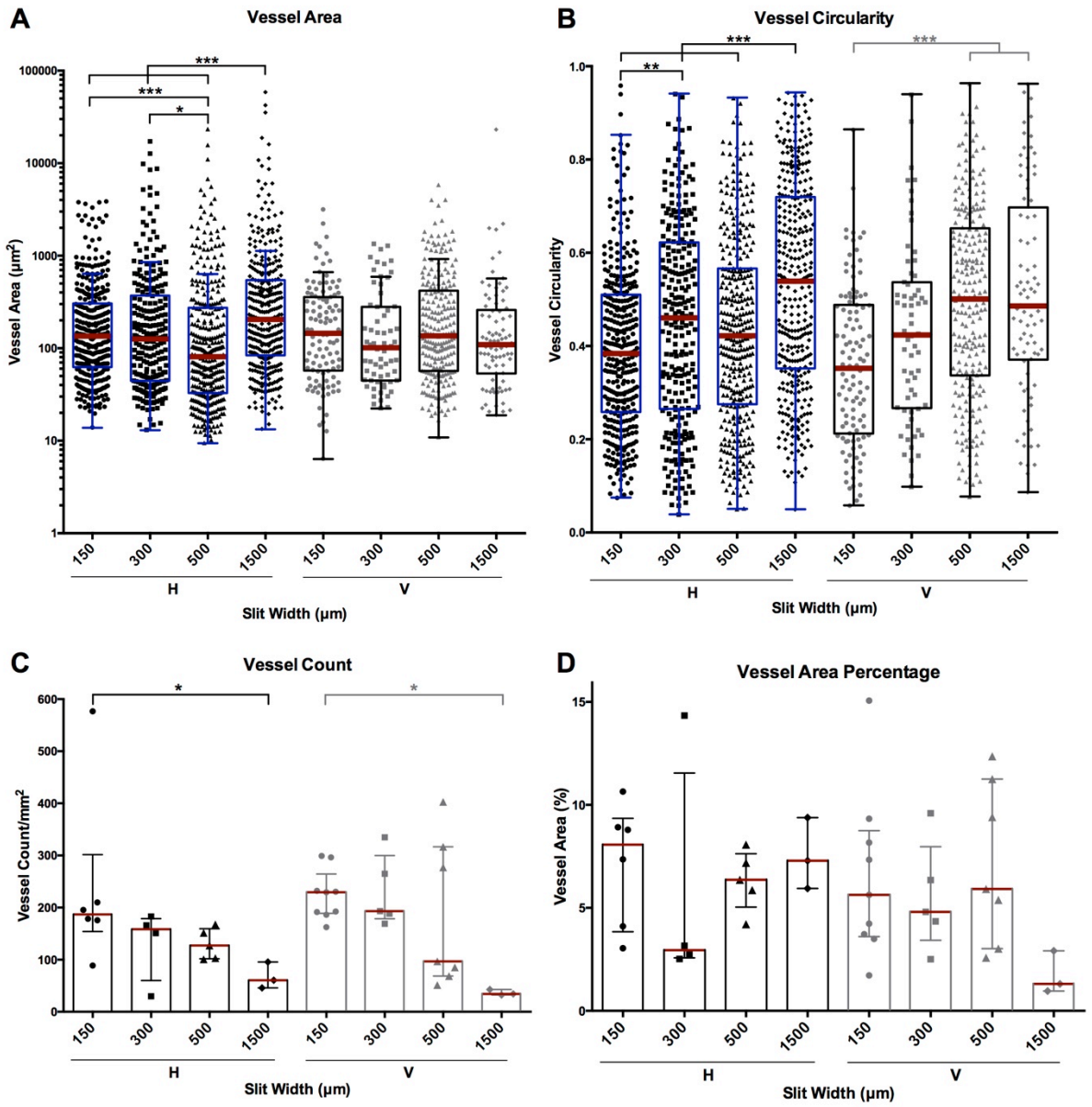

Figure 2.4: Quantification and comparison of vessel area, circularity, count, and area percentage within each slit width (150, 300, 500, 1500 μm) for both horizontal (H) and vertical (V) sections. Aggregate data of every detected vessel across all examined slit widths for (A) vessel area and (B) circularity. Each data point corresponds to a single vessel. The box plots show median (red), IQR (box), and 1.5IQR (or max and min values; whichever is shorter (whiskers)). Per slit, (C) the number of vessels per square millimeter tissue area and (D) the percentage of vessel area normalized by the total tissue area were quantified. Each data point is for a single slit. Data represent the median±IQR. Statistical differences are indicated by ***$p<0.001$, **$p<0.01$, and *$p<0.05$.

Assuming that vessels are on average circular in cross section, vessels that appear round (circularity ≅ 1) likely run more perpendicular to the direction of sectioning as

compared to those appearing oblong (circularity < 1), which may have a long axis at an angle to the section. Next, we compared vessel count and total vessel area percentage between multiple slits of the same width. For each individual slit, we determined total vessel count normalized by total slit area (Figure 2.4C), as well as the percentage of slit area occupied by vessels (Figure 2.4D). Interestingly, vessel count per slit area appears to decrease with increasing slit width (in both horizontal and vertical sections), and a statistically significant difference was detected between the 150 and 1500 μm groups. No trends or statistical differences were observed for percent vessel area.

Nerve axons were analyzed using the same metrics as for vessels. No nerves were detected within 150-μm-wide slits, but were detected within wider slits. While horizontal sections show nerves in the 300 μm slits had significantly larger areas as compared to those in the 500 μm slits (Figure 2.5A), this difference is biased by the unusually large nerve found in the 300 μm slit. In horizontal sections, nerve circularity within 300-μm-wide slits (Figure 2.5B) was significantly lower than that for the wider slits, a similar trend was observed for vertical sections. Next we investigated variability in nerve count and total area between multiple slits of the same width. For each individual slit, we determined total nerve count normalized by total slit area (Figure 2.5C), as well as the percentage of total slit area occupied by nerves (Figure 2.5D). No trends were observed for nerve percent area.

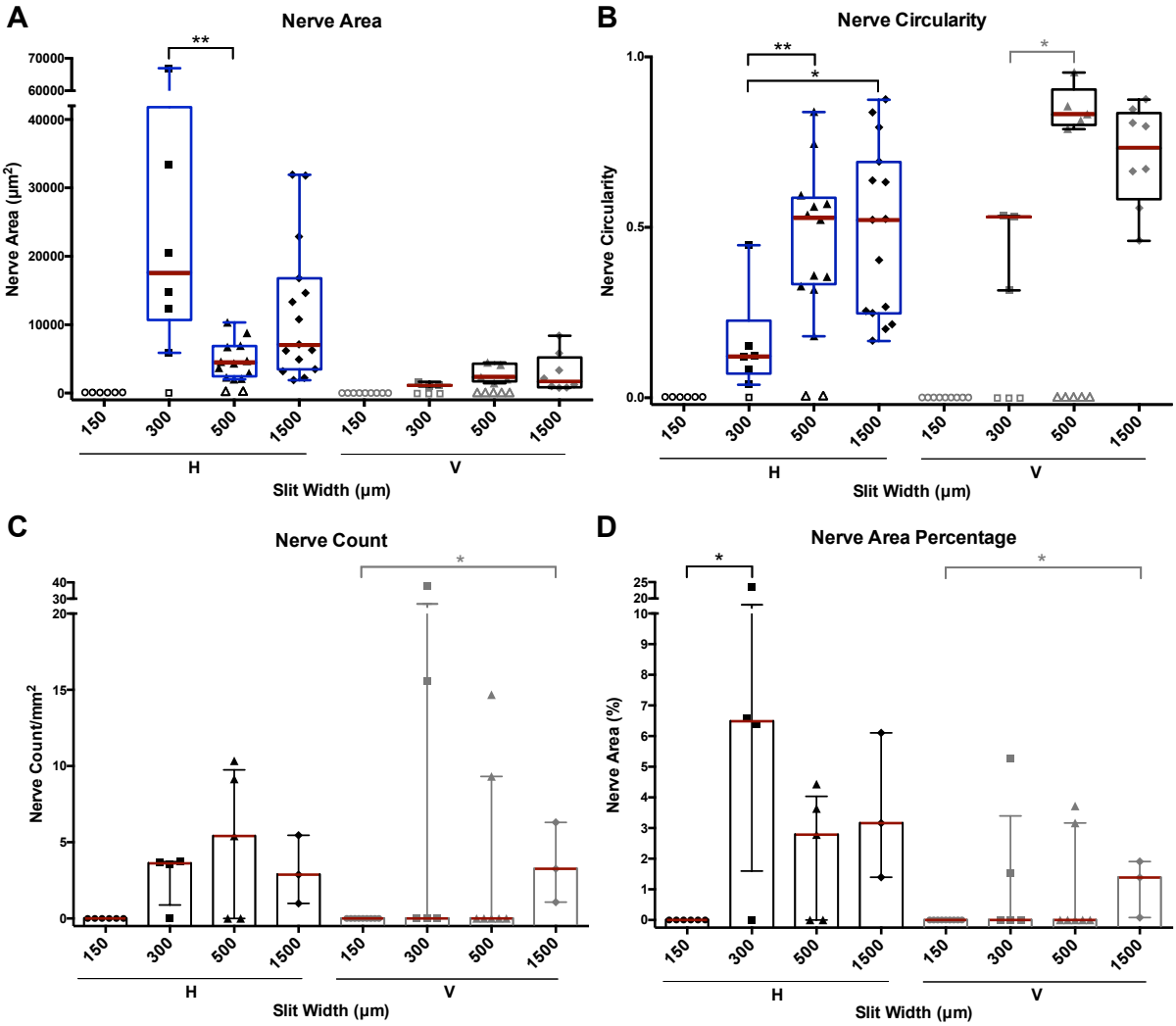

Figure 2.5: Quantification and comparison of nerve area, circularity, count, and area percentage within each slit width (150, 300, 500, 1500 μm) for both horizontal (H) and vertical (V) sections. Aggregate data of every detected nerve across all examined slit widths for (A) vessel area and (B) circularity. Each data point corresponds to a single nerve. Hollow symbols indicate that no nerves were detected in an individual slit. The box plots show the median, IQR (box), and 1.5IQR (or max and min values; whichever is shorter). Per slit, (C) the number of nerves per square millimeter tissue area and (D) the percentage of nerve area over the total tissue area were quantified. Each data point is for a single slit. Data represent the median±IQR. Statistical differences are indicated by ***$p<0.001$, **$p<0.01$, and *$p<0.05$.

2.4 Discussion

In this work, we describe a method to fabricate thin sheet silicone devices with varying slit widths to harness the host's tissue response to not only vascularize but also innervate an implant. Using a micro-stereolithographic printer for the quick prototyping of molds, sheets can be easily reconfigured (e.g. for slit width) and prototyped with PDMS or alternatively other moldable materials. Tissue within slits

contained nerve axons after 28 days of subcutaneous implantation. While the presence of nerve tissue in a device or scaffold typically indicates healthy tissue, it remains unclear if these nerve axons were formed de novo after implantation, or if they belong to native tissue that has fallen into the slits. There is conflicting evidence as to which mechanism is likely at day 28. A study of an engineered skin[75] implanted at the site of a full-thickness skin excision in nude mice shows absence of nerve tissue on day 40, with sparse innervation observed by day 60. This result suggests that insufficient time has passed for the de novo formation of nerve tissue in the slits and that only native nerve tissue is present. Conversely, new nerve tissue has been detected at day 28 in porcine-derived extracellular matrix scaffolds implanted intramuscularly within the rat abdominal wall[76] as well as in regenerated silk fibroin scaffolds implanted subcutaneously in immune-competent mice.[77] Relevant to these findings, slits in our sheets also contain a scaffold comprising fibrin polymerized from fibrinogen and other factors of autologous blood loaded into our sheets during implantation. Thus, there is a possibility that we observe new nerves at day 28.

To help elucidate which mechanism is responsible for innervation, we examined H&E-stained histological slides and notice, unexpectedly, what appears to be native tissue within slits that is innervated. This putative native tissue seems confined to the distal and proximal slit opening (Figure 2.2H, black arrows) for the 300-µm-wide slits and penetrates increasing deeper within 500- and 1500-µm-wide slits (Figure 2.2I and J, black arrows). The relationship between slit width and native tissue penetration is consistent with the fact that resistance of tissue to physical deformation into the narrow slits will increase with decreasing slit width. If this were the case, and if nerves were exclusively from native tissue, then we would expect at some critical slit width that no nerves would be detected. In support of this notion, the 150-µm-wide slits alone did not indicate infiltration of native tissue and excluded nerves.

These same 150-µm-wide slits do contain a dense population of blood vessels, which normally form by angiogenesis during wound healing. Considering that blood within the slits forms a fibrin scaffold known to support angiogenesis, we speculate angiogenesis dominated vascularization in 150-µm-wide slits, whereas both native and new vessels penetrated the 300- and 500-µm-wide slits. In support of this, we found more vessels per cross-sectional area in the narrower slits (Figure 2.4C), indicating that de novo vascularized tissue was formed containing vessels typically smaller than those observed in 1500-µm-wide slits that contain native tissue (Figures 2.4A and 2.2G-J). Interestingly, no matter the slit size, the tissue still maintains similar vessel area percentage (Figure 2.4D), which may be a critical finding with respect to the design of cell therapy devices because narrower slits increase the remaining area of the sheet available.

Finally, and importantly, our method exploits the host's own tissue response to vascularize and innervate an implant without the need for synthetic hydrogels or exogenous proangiogenic factors. Additionally, we observed vessel area percentage values ranging from 1.3% to 8.1%, which are similar to that reported for other scaffolds.[71,78,79] Thus, our approach of utilizing the body's own response to promote tissue infiltration into a thin sheet not only provides a dense vasculature, but will not be considered a drug-device combination product by regulatory agencies. To the best of our knowledge, this is the first study to investigate rectangular slit architecture in promoting tissue growth. Numerous geometries have been investigated previously, the most common being pores or microchannels with spherical or cylindrical shapes.[55–57,60,62,63,72]

Our findings demonstrate that rectangular slits are also a suitable geometry for promoting subcutaneous tissue infiltration. In general, the 150-µm-wide slits may be preferred over the wider slits if a vascularized, but not necessarily innervated, environment is required. On the other hand, the larger slit widths are more suitable to generate an innervated environment while remaining well vascularized. These

results provide information about the optimal slit width to use for sheet devices. A 300-500 μm slit width provides both vascularization and innervation while also maintaining a small device size. Although not a main focus for many islet transplant macrodevices, the capabilities of the slit architecture to provide innervation may be useful given that native islets are richly innervated in order to fine-tune hormone secretion.[80] The dimensions of 500 μm will be utilized for future experiments in and islet transplantation due to a smaller slit size and ease of fabrication.

2.5 Conclusion

Thin PDMS sheets with varying slit widths were molded via the simple and inexpensive technique of projection micro-stereolithography and implanted into the subcutaneous tissue of athymic nude mice. While no differences were found in blood vessel area percentage between the slit widths, vessel count did increase inversely with slit width likely due to active angiogenesis. We observed the infiltration of de novo tissue, an invagination of mature host tissue, or a combination of both. The presence of developed blood vessels and Schwann cells was confirmed by the expression of αSMA and S100, respectively. Further studies must be conducted to determine if results generalize to other tissue compartments such as the intramuscular space, omentum, or kidney capsule, or if our findings are exclusive to the subcutaneous space. In future work, sheets could contain openings or channels for cells to reside within the thickness of the sheet as a method for transplantation into a prevascularized and innervated network.

Chapter 3: Device Development

3.1 Introduction

With evidence that slit geometry allows for vascularization and integration into the subcutaneous tissue, it is now appropriate to fabricate entire devices with channels, windows, and other features that can support pancreatic islets for transplantation. This chapter describes the process of fabricating the devices and the design changes over time. Initially, the devices were large, and caused wound closure issues when implanted in the subcutaneous space in mice; subsequent device revisions scaled down the device size for improved healing. Vascularization of these subsequent designs via lectin staining and histology as well as oxygen availability was examined.

The timing of both islet revascularization and optimal device implantation in the realm of islet transplantation is poorly understood. A device prevascularization period of 28 days, in which a scaffold,[81] catheter,[34] or polymer rod[24] was inserted into the subcutaneous space prior to islet transplantation to stimulate the tissue response and vascularization *in vivo*, has been used previously; however, islets transplanted into a rodent dorsal window chamber within alginate encapsulation materials showed greatest blood flow in vessels near the implant relative to blood flow in vessels not near the implant and hemoglobin oxygen saturation by day 14[82] while another skinfold chamber after islet transplantation alone showed signs of angiogenesis in the first 2-4 days, with complete revascularization at day 10.[83] Because the optimal vascularization period is unknown and changes based on device and transplant site,[84] an investigation of the best time for islet transplantation via a noninvasive technique would be especially informative.

In this chapter, we employ a previous technique developed by the Botvinick laboratory:[85] an oxygen-quenching porphyrin dye that is probed with pulses of LED red light to measure oxygen dynamics *in vivo*. Depending on the partial pressure of oxygen surrounding the dye, a unique luminescent lifetime decay value characterizes the light emitted by the dye.[86] This dye is incorporated into the devices via oxygen sensitive tubes (OSTs) and probed optically and noninvasively over time. With this information on oxygen dynamics, we set out to determine an optimal

prevascularization period. Oxygen measurements and analysis were completed in collaboration with Dr. Avid Najdahmadi[87] and Mellonie Zhang,[88] alumni from the Botvinick laboratory.

Additionally in this chapter, we investigated a method of loading islets within devices. We aimed to minimize the device channels such that islets could be organized in a single-file configuration, precluding a necrotic core. The channel size also had to allow for the wide range of islet diameters (50-500 μm). Typically, islets are loaded into other scaffolds, the subcutaneous space, or the kidney capsule space by aspirating the islets and centrifuging them into a pellet using polyethylene (PE)-50 tubing, with an outer diameter of 965 μm, which was too large to fit into the device channels of ~400 μm. First, we investigated loading the channels with a needle and syringe. We hypothesized that the high fluid pressure associated with needle loading was damaging the cells. Thus, smaller diameter polyimide (PI) tubing and alternative loading method was explored.

Lastly, in preliminary experimentation, a challenge that arose was the tendency for islets to compress through the device windows and escape the channels (Figure 3.1) when loaded with a needle and syringe. To counteract this, we incorporated polyether ether ketone (PEEK) braids, similar to a stent, into the device channels. The PEEK braids serve two purposes: (1) contain islets within device channels and (2) keep channels patent. As an FDA-approved material, PEEK has been incorporated in many medical devices.[89] More specifically, Beta-O_2, a company developing a subcutaneous macroencapsulation device with a refillable oxygen chamber, utilizes PEEK for the device housing to provide mechanical protection.[90,91] PEEK was also used for hollow fiber membranes and protected islets from interleukin-1, a toxic chemokine.[92] In addition, PEEK serves as the mesh material surrounding a polymer rod used for prevascularization before islet transplantation.[93]

In this chapter, prototype PDMS sheet devices are revised to achieve a refined design. Devices are evaluated for vascularization via lectin staining and oxygen measurements. In addition, islets are loaded into PEEK-reinforced channels within devices using small diameter PI tubing and assessed for viability.

3.2 Materials and methods

3.2.1 Early prototype device fabrication

Devices were fabricated similarly to that as previously described in Chapter 2.[50] Briefly, device molds were designed in SolidWorks, converted to STL files, and printed on a photostereolithographic 3D printer (Asiga Pico Plus 27) with PlasGRAY (Asiga) material. Molds were washed and sonicated in isopropanol, left to air dry for 10 min, post-cured with 302 nm UV light for 10 min (Dual UV Transilluminator, VWR), and hardened by heating in an oven overnight at 60°C. Molds were then silanized with (tridecafluoro-1,1,2,2-tetrahydrooctyl)trichlorosilane (Gelest). PDMS (Sylgard® 184, Dow Corning) mixed at a ratio of 1:10 (curing agent: monomer base) by weight was poured into the molds, degassed in a desiccator for 20 min, and then cured in an oven at 60°C for at least 2 hours. Pieces were carefully removed from the molds with tweezers.

Two components made up an entire device: a 'ceiling' and 'floor' piece. The floor contained all of the features of the device (windows, slits, and channels) while the ceiling was a solid sheet of silicone that sealed off the device to create the enclosed channels. The ceiling and floor pieces were treated in a plasma cleaner (Harrick) to activate the silicone surfaces, and bonded together. After bonding, slits in the ceiling were carefully cut out with a razor blade using the slits in the floor as a guide to create a through-cut slit space. The slit is entirely open through the whole thickness of the device. For prevascularized devices, wires (30G, Kanthal) were inserted into the channels to prevent tissue ingrowth during the vascularization period. Complete devices were sonicated for 1 hr in 70% ethanol, placed in autoclave packets, and autoclaved at 122°C for 20 min. Early device prototypes were used for first generation *in vitro* islet loading (Section 3.2.4), oxygen experiments (Section 3.2.7, Section 3.3.4), and animal islet transplant experiments 1-2 (Figure 3.5A-B, Section 4.3.1-4.3.2). Further details on dimensions of these device prototypes can be found in the Appendix (Figure A.1-A.3).

3.2.2 Later prototype device fabrication

Later prototypes of the device were fabricated as described in the previous section with some changes. After molds were silanized, they were then blown with air to remove debris. For sterilization, molds were placed in 70% ethanol and sonicated for 1 hr. While under a biosafety cabinet, medical grade PDMS (MED-6215, Nusil™) mixed at a ratio of 1:10 (curing agent: monomer base) by weight was poured into the molds placed in petri dishes. The PDMS-filled molds were degassed in a desiccator for 20 min and then cured in an oven at 60°C for at least 2 hours while remaining within the petri dishes. Pieces were removed from the molds using sterile tweezers under a biosafety cabinet and placed into new petri dishes to maintain sterility.

PEEK braids (MicroLumen, outer diameter: 418 μm, inner diameter 368 μm) were sterilized in 70% ethanol and sonicated for 1 h. Braids were removed from the mandrel on which they were shipped, cut to a length with wire cutters, sprayed with 70% ethanol, and placed into device channels in the 'floor' pieces with sterile tweezers. The ceiling piece was molded to contain slits (instead of a solid piece with slits cut out, as done previously) and carefully aligned with the slits in the floor following plasma treatment, and bonded. For prevascularized devices, either the silver plated copper mandrel wires on which the PEEK braids came (experiments 3-4) or polyimide (PI) tubing (MicroLumen) (experiments 3, 5) were inserted into the braid-reinforced channels to prevent tissue ingrowth during the prevascularization period. In animal experiment 3, ceiling and floor pieces were of the same outer dimensions. The device was further modified for animal experiments 4 and 5 with the goal of eliminating unintended protrusion of the inserted wires up through the epidermis. Thus, the ceiling piece was lengthened to extend over the channel openings such that the wires were protected.

Assembled devices were checked for slit alignment, sonicated for 1 hr in 70% ethanol, placed in autoclave packets, and autoclaved at 122°C for 20 min. Later device prototypes were used for both *in vitro* (Section 3.2.5-3.2.6, 3.3.2) and *in vivo* animal lectin (Section 3.2.5, 3.3.3) and islet experiments 3-5 (Figure 3.5C-D, Section

4.3.3-4.3.5), with the exception that experiment 3 still utilized Sylgard 184® rather than the medical grade NuSil™ MED-6215. Animal experiments are described in further detail in Chapter 4. SolidWorks drawings for the various prototypes of the molds for the devices can be found in the Appendix (Figure A.4-A.7).

3.2.3 Islet isolation

Sprague-Dawley (SD) rat islets were isolated via collagenase digestion and density purification according to standard techniques[94] and cultured overnight in PIM(R) media (Prodo Laboratories). Two samples of approximately 50 islets from the islet suspension were stained with zinc-binding dithizone (DTZ, MP Biomedical) to discern between endocrine and exocrine tissue and counted by categories of islet diameter ranges via brightfield microscopy (EVOS) and ImageJ to achieve islet equivalent (IE) counts and prepare islet aliquots.

3.2.4 First generation *in vitro* islet loading

In first attempts to load islets within devices, a blunt needle (25G, CML Supply) and 1 mL syringe (Becton Dickinson) was filled with the islet aliquot. The needle was directly inserted into the device channels. The syringe plunger was pushed to release islets into the channel. When loading, we observed islet compression through the windows of the device (Figure 3.1C) and escaping the device channels. Figure 3.1A is a schematic of the device (also shown in Figure 1.3) and can be compared with the micrograph in Figure 3.1C. To counteract this islet compression, PEEK braids (Figure 3.1B, outer diameter: 418 μm, inner diameter: 368 μm) were inserted into device channels as described in Section 3.2.2 and a second generation loading method with small diameter polyimide tubing was explored.

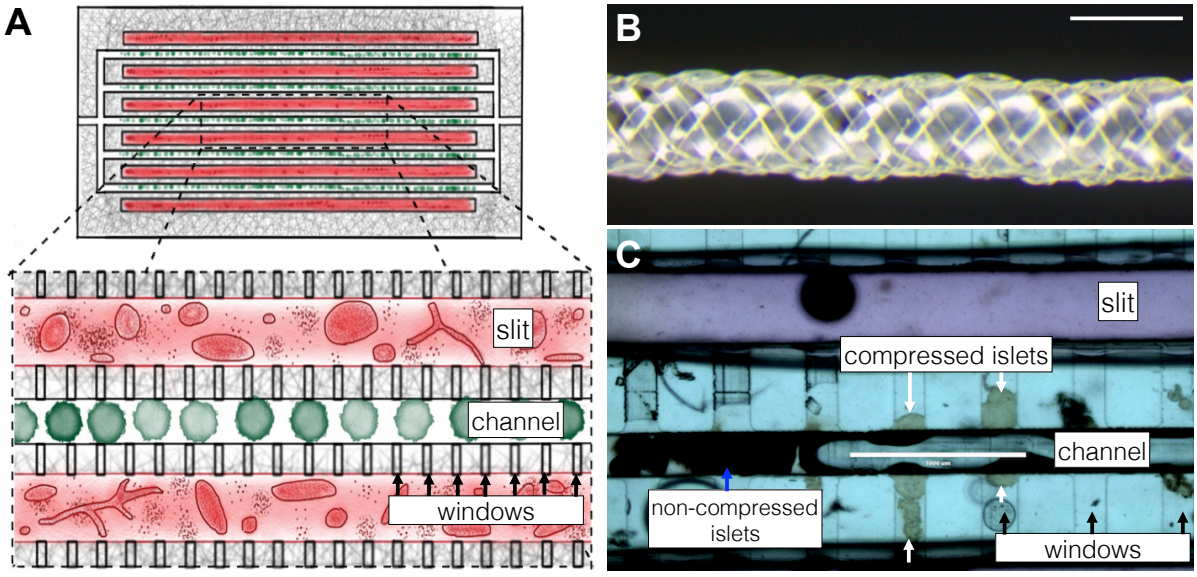

Figure 3.1: First generation islet loading and islet compression through the windows of the device. (A) As a reminder, the schematic of the device is shown with labeled slit, channel, and windows (black arrows). (B) PEEK braids of an inner diameter of 368 µm and outer diameter of 418 µm are inserted into device channels to prevent islet compression (white arrows) seen in (C), a micrograph of a PDMS device with labeled slit, channel and windows. Some non-compressed islets within the channel can also be visualized as dark objects (blue arrow). Scale bars=500 µm (B) and 1000 µm (C).

3.2.5 Second generation *in vitro* islet loading

Islet aliquots were separated into three groups, (1) control (CTRL), (2) polyimide tubing (PI), and (3) device (DVC). For the CTRL group, islet aliquots were placed in a 6-well nonstick plate (Fisher Scientific) and placed back into the incubator for overnight culture. For the PI group, a 5 mL syringe (Becton Dickinson) with a 25G blunt needle (CML Supply) attached to three polyimide (PI) tubes (MicroLumen; inner diameter: 251 µm, outer diameter: 300 µm), via heat shrink tubing and a silicone PDMS (Sylgard® 184) seal to prevent leakage (Figure 3.2A). The syringe plunger was slowly pulled back to aspirate the islets from a petri dish into the tubing (Figure 3.2B). To test if there were any deleterious effects of the loading method and tubing itself, the islets remained within the tubing for 10 min and were subsequently pushed back out into a fresh 6-well plate for overnight culture. For the DVC group, islet aliquots were first loaded into the PI tubing as for the PI group. Once filled, each of the PI tubes was next inserted into the full length of the PEEK braids (MicroLumen) (Figure 3.2C) within the device channels. Islet loading was achieved

by simultaneously, and carefully, pushing in the syringe plunger to release the islets as the PI tubing is slowly retracted out of the braids in the device channels in a single-file configuration (Figure 3.2D). In this way, 3 braid-reinforced channels are loaded simultaneously. Islet-filled devices were placed in 6 well plates for 3 hr incubation or overnight culture.

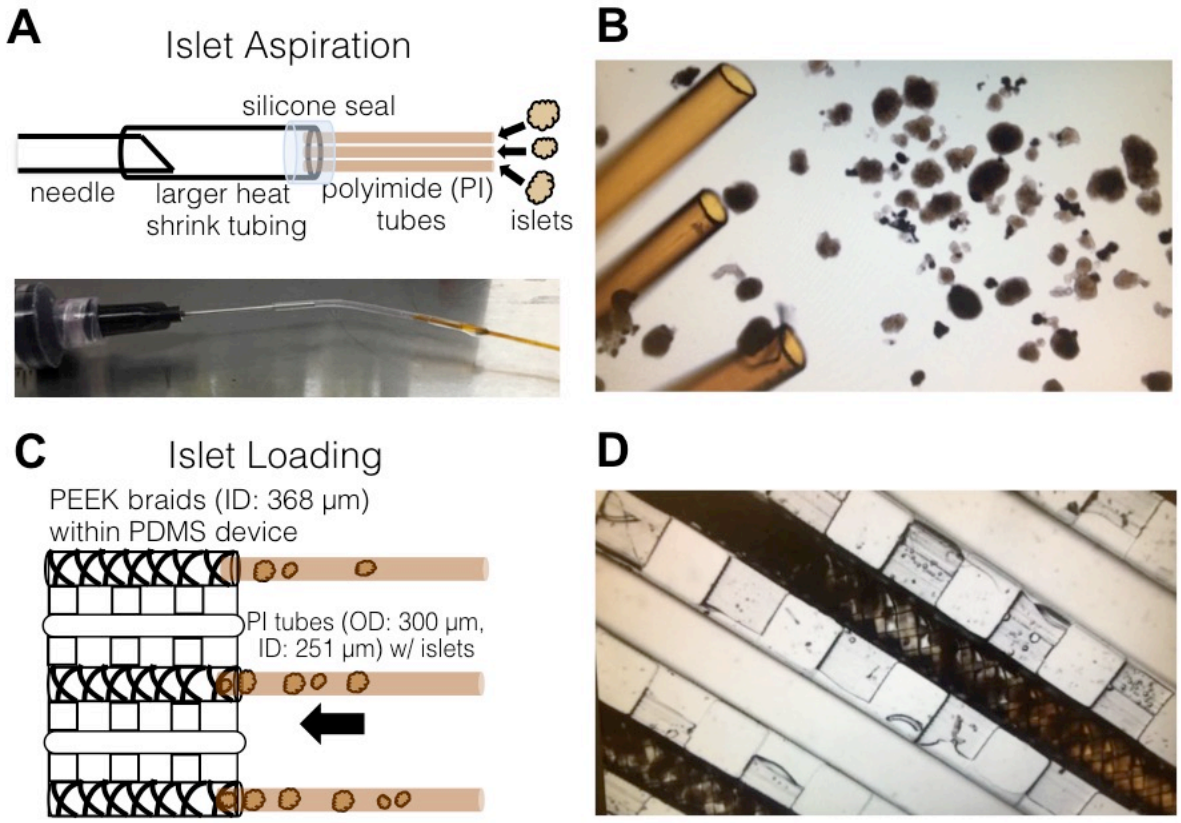

Figure 3.2: Second generation islet loading.
(A) First, SD rat islets are aspirated into a custom tubing apparatus. A schematic (top) and picture (bottom) of the apparatus shows a needle connected to 3 polyimide tubes (PI) via heat shrink tubing and sealing with PDMS. (B) Using the connected needle and syringe to control flow, the PI tubes are loaded with islets from a petri dish. (C) A schematic of the orange PI tubing being inserted into the channels of a PDMS device containing windows and embedded PEEK braids. (D) The loaded PI tubes are inserted into braid-enforced device channels. Three channels are simultaneously loaded with islets in a single-file configuration as the PI tubes are retracted manually.

3.2.6 Islet viability and imaging

DVC islets either remained within devices after 3 hr incubation or were retrieved from devices after overnight culture and subjected to viability staining via live/dead assay. All samples (CTRL, PI, DVC) were incubated with 50 µM calcein AM (live) and 37.4 µM propidium iodide (dead)[95,96] (Life Technologies) for 15 min in the dark

at room temperature. Samples were washed with PBS (Lonza) and placed into glass bottom dishes before imaging. Confocal imaging was done on an IX-81 inverted microscope (Olympus) equipped with a FluoView 1200 laser confocal scan head (488 nm and 559 nm laser lines, Olympus), using a 40× air objective (LUCPLFLN, 0.60 NA, Olympus). Image stacks through the volume of an islet were acquired using a z-step of 5 μm. These image stacks (n=9 per group) were processed in Fiji[97] and used to calculate areas of dead and live staining to quantify viability *(1 - area of dead staining/total islet area)*.

3.2.7 *In vivo* device implantation and lectin staining

Fully fabricated devices (later prototype, Appendix Figure A.6-7) were implanted into the subcutaneous space of 6-8 week old athymic nude mice (Envigo) to assess vascularization of full thickness devices under Institutional Animal Care and Use Committee (IACUC) at the University of California Irvine, protocol #2008-2850 and AUP-018-038. Similar to previously described techniques,[50] a midline incision through the dorsal skin was created via sterile scalpel (Bard-Parker®) and a subcutaneous pocket was created by blunt dissection. A device was dipped in saline and placed into the pocket using tweezers. The dorsal incision was sutured closed and secured with surgical clips. The animals received ibuprofen, between 50 and 80 mg/kg, via drinking water for 2 days following surgery. In some animals after 3 weeks, devices were explanted and imaged under an EVOS scope for macroscopic views of device vascularization. In some animals after 4 weeks and before sacrifice, retroorbital injection of 200 μL DyLight® 649 labeled lycopersicon esculentum tomato lectin (Vector Laboratories) diluted 1:3 in PBS was allowed to circulate for 15 min. Animals were sacrificed and devices were explanted and fixed in 10% phosphate buffered formalin.

After at least 24 h fixation, samples were optically cleared by submerging in FocusClear™ (CelExplorer) for 24 h. Confocal imaging on the same system as described in the previous section allowed for visualization of the vasculature surrounding and entering the device using a 559 nm laser line and a 10× air objective

(UPLFL, 0.30 NA, Olympus). Images throughout the volume of the device were acquired with a z-step of 10 μm and stitched together in Fiji.[97] Z-stacks at a z-step of 5 μm at regions of interest were also acquired. From the z-stacks, a maximum intensity projection was created to observe the extent of vascularization around the device.

3.2.8 Fabrication of Oxygen Sensitive Tubes (OSTs)

The oxygen sensitive tubes comprises silicone tubing (BTSIL-025, Instech Laboratories) having an outer diameter of 0.64 mm and inner diameter of 0.31 mm homogenously coated on the luminal surface with oxygen-sensitive film: a luminescent porphyrin dye platinum(II)-meso-tetra (4-flurophenyl) tetrabenzoporphyrin (PtTPTBPF) (Frontier Scientific) embedded within micron-sized polystyrene (MW: 2500, Sigma-Aldrich) particles dissolved using chloroform (Sigma-Aldrich). The dye has peak absorptions at 430 and 614 nm and emission peak at 773 nm. The tubes were left to dry in the dark for 24 h for any remaining chloroform to evaporate. A stainless steel wire (24G A1 wire, Kanthal) was inserted into each OST to provide mechanical support. The tubes were cut to length of the devices and the ends were sealed with silicone (MED-1000, Nusil^{TM}). The sealed tubes were kept in a dark environment at room temperature for 2 days to fully cure.

3.2.9 OST calibration and device fabrication

Governed by oxygen-quenching of the porphyrin dye and based off the partial pressure of oxygen proximal to the OSTs, the light emitted by the dye following strobed optical excitation decays exponentially with a specific luminescent lifetime decay value, τ, which is inversely related to pO_2. Probed by a custom emitter-detector system controlled by LABVIEW (National Instruments), individual OSTs were placed within a custom gas chamber (Figure 3.3A) for *in vitro* calibration by exposure to different gases. These gases included room air (152 mmHg, 21%), 76 mmHg (10%), 38 mmHg (5%), 15.2 mmHg (2%) oxygen, and argon (0% oxygen). Three OSTs were matched with similar calibration curves and inserted into three-

channel, four-slit PDMS devices (10 mm x 13 mm x 1.3 mm), (Figure 3.4A, Appendix Figure A.1). With one OST per channel (a total of three OSTs), devices were placed into the gas chambers, and calibrated once more at each of the oxygen levels listed (Figure 3.3B). A calibration curve was thus generated for each oxygen sensitive device containing 3 individual OSTs (Figure 3.3C). The lifetime to oxygen conversions (Figure 3.3B,C,D) were performed using a custom MATLAB (MathWorks) code based on the Stern-Volmer equation through averaging lifetime values measured at each oxygen concentration. Devices were sterilized by immersion in 70% ethanol for 12 h.

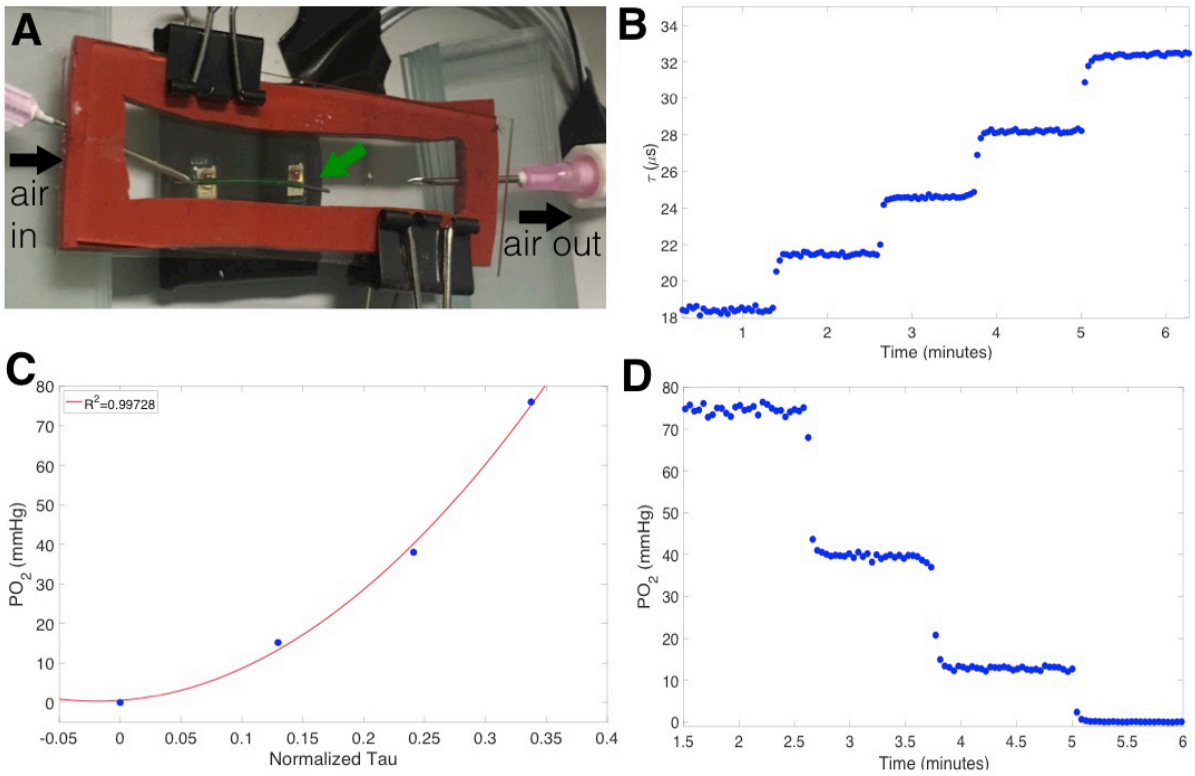

Figure 3.3: Oxygen sensitive tube (OST) and device calibration.
(A) Calibration apparatus includes a custom gas chamber allowing gas mixtures of nitrogen and prescribed % oxygen to flow over (black arrows indicate air flow) one or more fabricated oxygen sensitive tubes (green arrow). (B) Unique lifetime decay values (τ) at each pO_2 level (0, 15.2, 38, 76, 156 mmHg), represented by plateaus, captured with a custom emmiter-dector system. (C) A calibration curve relating τ to pO_2 is fit using the average plateau τ at each oxygen level (without 156 mmHg) in (B). (D) The original calibration data in (B) is converted back to pO_2 using the calibration curve in (C).

3.2.10 Animals and Dynamic Inhaled Gas Test (DIGT)

Under approval of the IACUC at UCI (IACUC #2008-2850), devices with OSTs inserted into device channels (Figure 3.4A) were implanted subcutaneously in 8-week old athymic nude mice (Envigo) (n=5) similar to that previously described.[50] Athymic nude mice were used for comparison to prior vascularization[50] and future islet transplantation studies and due to their hairless attributes, making optical measurements more feasible. Briefly, a small incision (~15 mm) through the dorsal skin was created by sterile scissors and a subcutaneous pocket was created by blunt dissection. One device per animal was placed into the pocket using tweezers (Figure 3.4B) and the dorsal incision was secured with surgical clips. The animals received ibuprofen, between 50 and 80 mg/kg, via drinking water for 2 days following surgery.

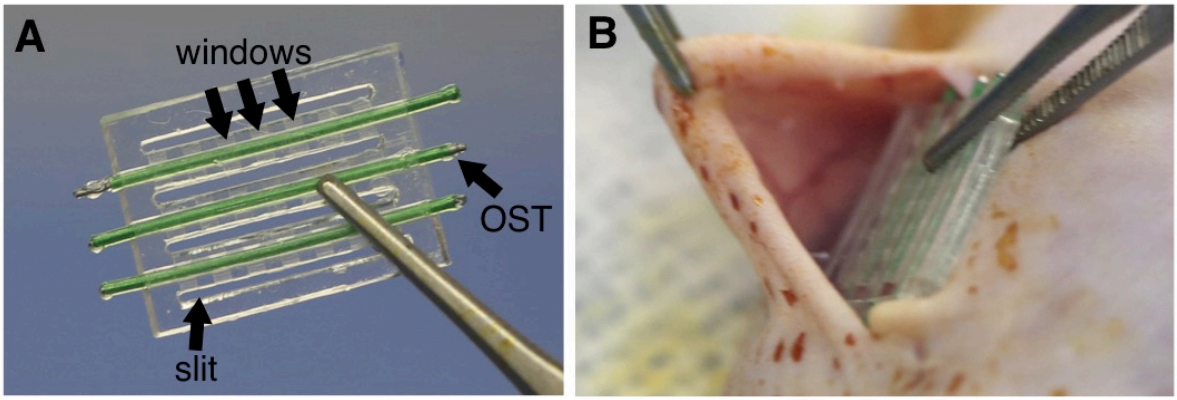

Figure 3.4: Oxygen sensitive devices and implantation.
(A) PDMS devices with three inserted oxygen sensitive tubes (OSTs) with matching calibration curves were assembled to create oxygen sensitive devices. (B) Oxygen sensitive devices were implanted into the subcutaneous space of athymic nude mice.

Oxygen transport between the blood and the implanted OSTs was measured using a dynamic inhaled gas test (DIGT).[85] In a DIGT, an animal was first anesthetized by 5% isoflurane and 100% O_2 (760 mmHg) initially until the animal was under complete anesthesia. The animal was also connected to a physiological monitoring system (PhysioSuite®, Kent Scientific) to monitor body temperature and SpO_2 during the duration of the test. The gas is quickly changed to room air (21% O_2, 152 mmHg) and 1.5% isoflurane. The emitter detector system was then placed on the surface of the animal's skin above the implanted device. After approximately 100

measurements (spaced by 4.25 s for a total of 425 s), the inhaled gas is switched back to 100% O_2 with isoflurane. Over time, the tissue pO_2 reported by OSTs was expected to increase, or lifetime value (τ) decreases, until a new steady-state is reached. The time period from which the pO_2 reaches its new steady-state relative to the time of gas exchange is defined as the *rise time*. Measurements of oxygen sensitive devices by the emitter detector system during a DIGT were taken for a maximum time of 1 h. The time points assessed were day 3, 7, 14, 21, 28, 35, 42, 49, and 56. For each animal at each timepoint, one metric for comparing the data is to compute the DIGT slope ($\mathbf{\Delta}P/\mathbf{\Delta}t$) as a measurement of oxygen dynamics was used. During the rise time, the slope was computed between the time at which the minimum PO_2 and the time at which the maximum PO_2 was reached.

3.2.11 Histological examination

After 56 days (8 weeks), animals were sacrificed. Devices were explanted and fixed in 10% phosphate buffered formalin for 24 h. Due to difficulty of sectioning PDMS, device tissue samples went through post-processing steps to separate the tissue from the silicone material. One end of the device was cut with a fresh microtome blade (SHURSharp^{TM}, Triangle Biomedical Sciences, Inc.). The device was slid out from the surrounding tissue, leaving 'holes' where the device once was and the surrounding slit tissue intact. Samples were given to JIT Labs (Irvine, CA) to be blocked on edge in paraffin, sectioned and stained for H&E.

Immunohistochemical staining similar to that previously described[50] indicated vasculature. Briefly, sections were deparaffinized, rehydrated, and subjected to overnight incubation in 0.1 M Tris/HCl buffer, pH = 9 at 80°C. Sections were washed with PBS (Lonza), permeabilized with 0.5% Triton X-100, and blocked with 5% donkey serum (Jackson ImmunoResearch) for 1 hr at room temperature. After blocking, slides were incubated overnight at 4°C with 1:200 monoclonal rabbit anti-alpha smooth muscle actin (ab124964, Abcam) and 1:200 polyclonal goat anti-CD31 (sc-1506, Santa Cruz Biotechnology) in PBS with 5% donkey serum and 0.5% Triton

X-100. Slides were washed with PBS and incubated with 1:500 AlexaFluor 488 donkey anti-rabbit (Life Technologies) and 1:400 AlexaFluor 594 donkey anti-goat (Jackson ImmunoResearch). DAPI (1:3000, Invitrogen) counterstaining was also performed. Images were taken on an Olympus IX-83 microscope with a 20× air objective and an Orca R2 camera (Hamamatsu Photonics) through Micro Manager[70] and stitched together using Fiji.[97]

3.2.12 Quantification of vessel count/morphology

Similar to that described previously in Chapter 2,[50] H&E slides were imaged with a Nikon eclipse E800 microscope at 4× using Olympus cellSens Entry program stitched together using Fiji[97] to visualize the entire surrounding device tissue. Each slit within the oxygen sensitive devices were imaged at 20× and stitched together using Fiji.[97] Stitched images for each slit were analyzed with a custom MATLAB code for manual tracing of blood vessels within each slit. Vessels were identified by three criteria: (1) hollow lumen, (2) endothelial cell lining, and (3) luminal erythrocytes.[71,72] The vessel area percentage or count was calculated as total vessel area or count divided by total slit tissue area.

3.2.13 Statistical analysis

GraphPad Prism software was used to perform statistical analysis on all data. For islet viability, data was found to not pass the D'Agostino-Pearson normality test so nonparametric Kruskal-Wallis test was used to compare the three groups. For slope values during rise times of DIGTs, nonparametric Friedman test for repeated measures followed by post-hoc Dunn's multiple comparisons tests was used to detect differences amongst groups. For vessel area and density data, nonparametric Kruskal-Wallis test was used to compare individual devices, as done previously.[50]

3.3 Results

3.3.1 Device evolution

As described in Section 3.2.1 and 3.2.2, the device went through many changes over the course of animal experiments. After each *in vitro* and *in vivo* experiment, modifications based off what was learned were made to lead to improved outcomes. Figure 3.5 displays the 4 different prototypes that were tested. Overall, devices decreased in size from 30 x 20 mm to 18.5 mm x 10 mm to 14.5 mm x 10 mm and lastly, 13.3 mm x 13.3 mm. Sheet thicknesses of ~1 mm remained the same throughout all prototypes. Decreases in size were motivated by the failures in wound closure with larger devices. Early prototypes of the device (Figure 3.5A-B) were fabricated by cutting out the slit space of the ceiling with a razor, potentially introducing rough edges, so direct molding and use of medical-grade PDMS was incorporated into later device fabrication methods. Additionally, loading issues were observed (Figure 3.1), so PEEK braids and a capped channel design in the subsequent later device prototypes (Figure 3.5C-D) were introduced to prevent islets from escaping the device channels. Rounded device edges and a ceiling flap were incorporated in the final prototype (Figure 3.5D) to further facilitate healing.

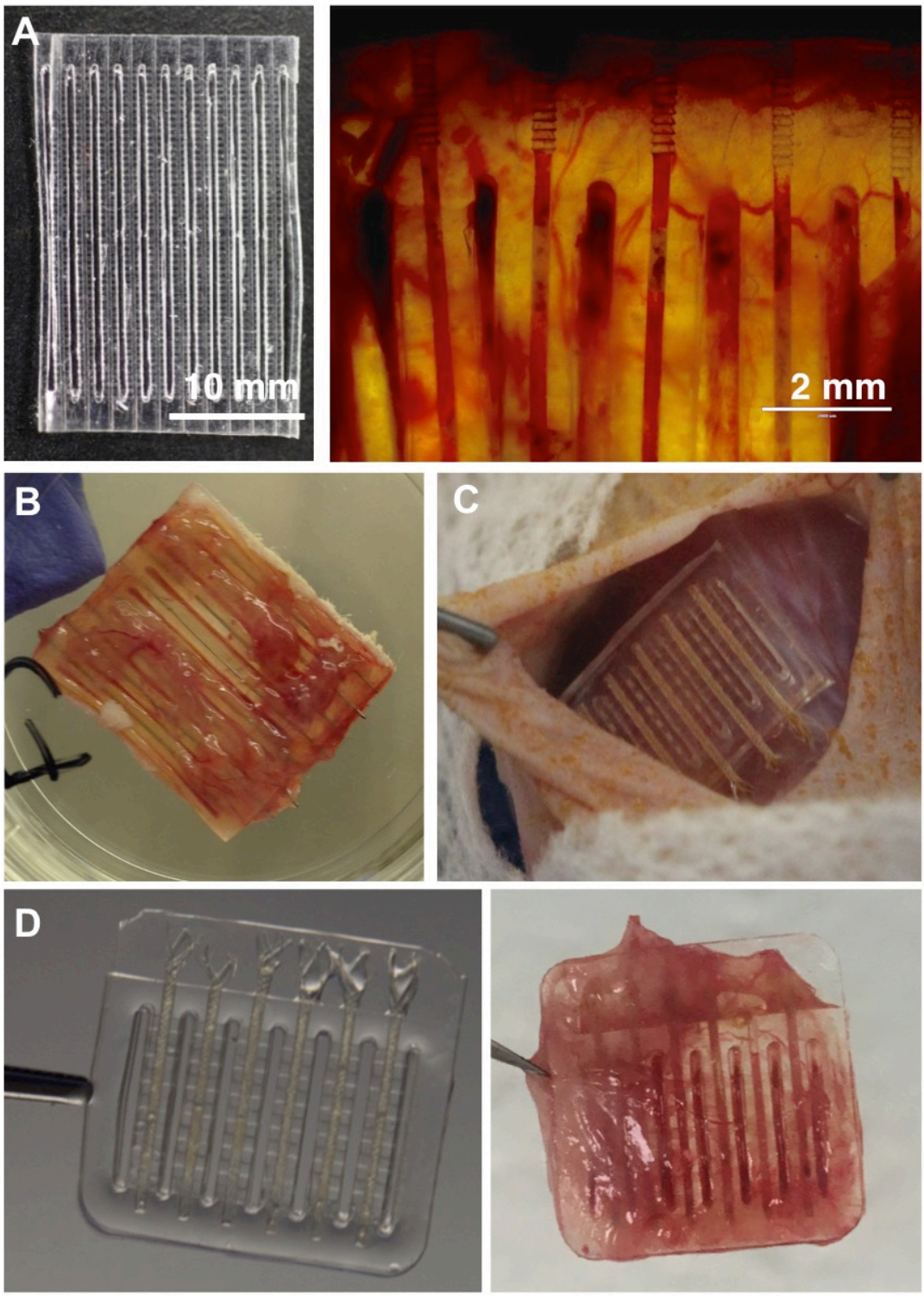

Figure 3.5: Device evolution.
(A) First prototype of islet transplant device before (left) and after (right) implantation in athymic nude mice measuring 30 mm x 20 mm x 1 mm with 8 channels. (B) Smaller device used for second transplantation experiment post explantation, measuring 15 mm x 18.5 mm x 1 mm with 8 channels. (C) Even smaller device measuring 10 mm x 14.5 mm x 1 mm with 6 capped channels used for third islet transplantation study during implantation. (D) Sheet device with rounded edges and ceiling flap used for the 4^{th} and 5^{th} islet transplantation experiments before (left) and after (right) implantation measuring 13.3 mm x 13.3 mm x 1 mm with 6 capped channels.

3.3.2 *In vitro* islet viability

In order to test if the second generation loading method described in Section 3.2.5 adversely affected, viability of pancreatic islets was investigated. After isolation and overnight incubation, SD rat islets were either incubated in media alone (CTRL) in a petri dish, loaded into PI tubing for 10 minutes and ejected out into a petri dish (PI), or loaded into devices (DVC) using the PI tubing in a single-file configuration and incubated for 24 hrs. CTRL, PI, and DVC islets were stained for viability and imaged on a confocal microscope. For each group (n=9), dead cell area and total islet area were calculated to give viability percentages *(1 - dead cell area/total islet area)*. All groups maintained high viability (Figure 3.6) and no statistical differences were found between groups via Kruskal-Wallis nonparametric testing. Islets that remained within the braid reinforced channel for a 3 hr incubation time and stained for viability also appeared to maintain high viability (Figure 3.7).

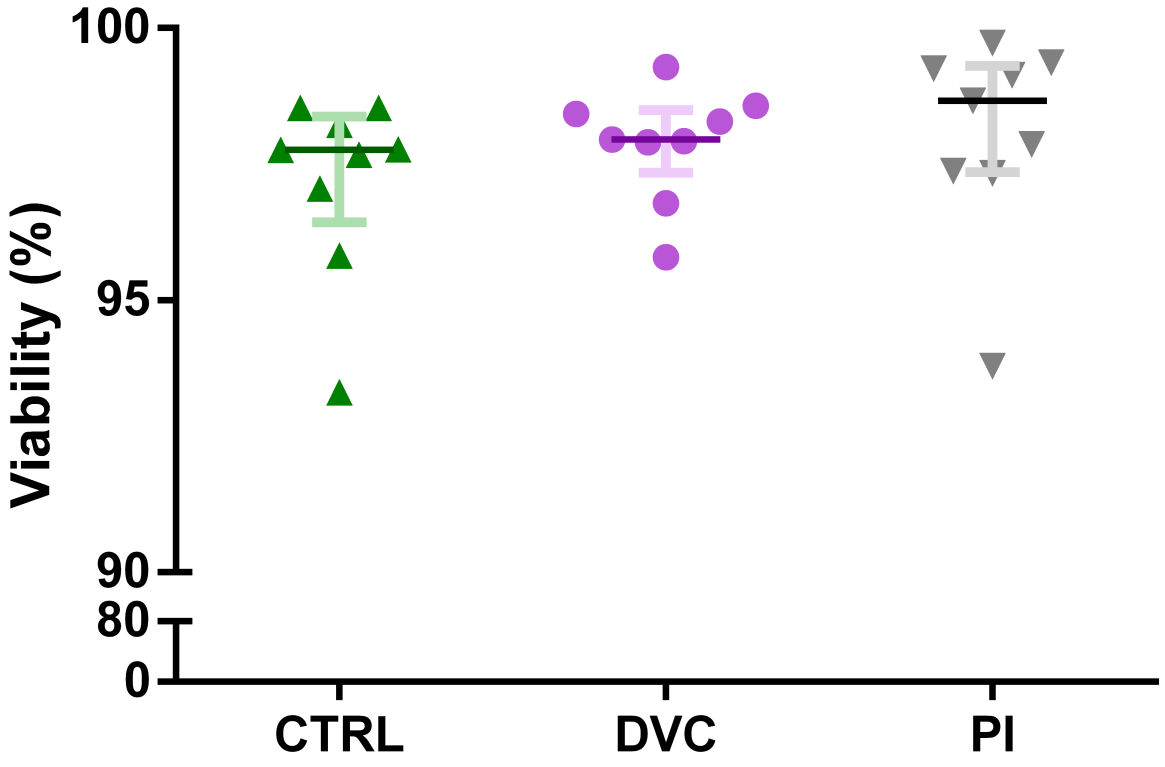

Figure 3.6: Viability of SD rat islets.
Islet viability after 24 hours was quantified for each group (n=9) and all maintained high viability. Data is represented as median±IQR. Kruskal-Wallis test resulted in no statistical differences.

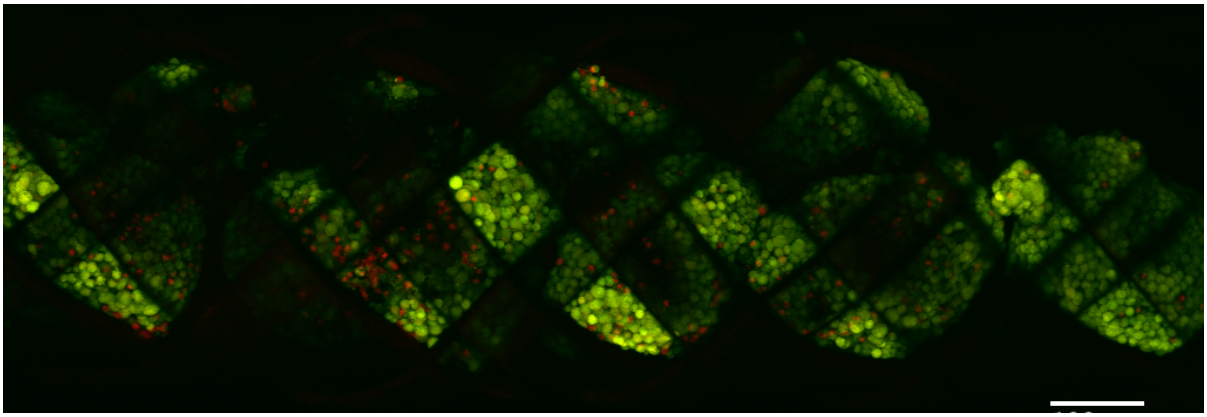

Figure 3.7: Islet viability staining within PEEK braids.
After 3 hour incubation, islets loaded into PEEK braids in a single-file configuration were stained with calcein AM (live, green) and propidium iodide (dead, red). Scale bar=100 μm.

3.3.3 Lectin perfusion

In Chapter 2, we investigated the ability for 0.5 mm thick slit sheets (no channels or windows) to integrate with the subcutaneous tissue. To investigate the ability for full thickness devices (1 mm) to be vascularized, fully fabricated devices with channels and windows were implanted into the subcutaneous space of athymic nude mice. After a 3 week implantation period, macroscopic observation of the devices (Figure 3.8) indicated vasculature growing around the device, and into the slit space (Figure 3.8A). The details of this vasculature was further illustrated by whole-device lectin perfusion and staining after a 4 week implantation period (Figure 3.8B). Investigation of an individual section z-stack demonstrated vasculature diving into the slit space (Figure 3.8C) close to the material like roots from a tree wrapping around the device. The white and yellow colorings signify deeper vessels within the device while blue and purple colorings denote more surface level vessels.

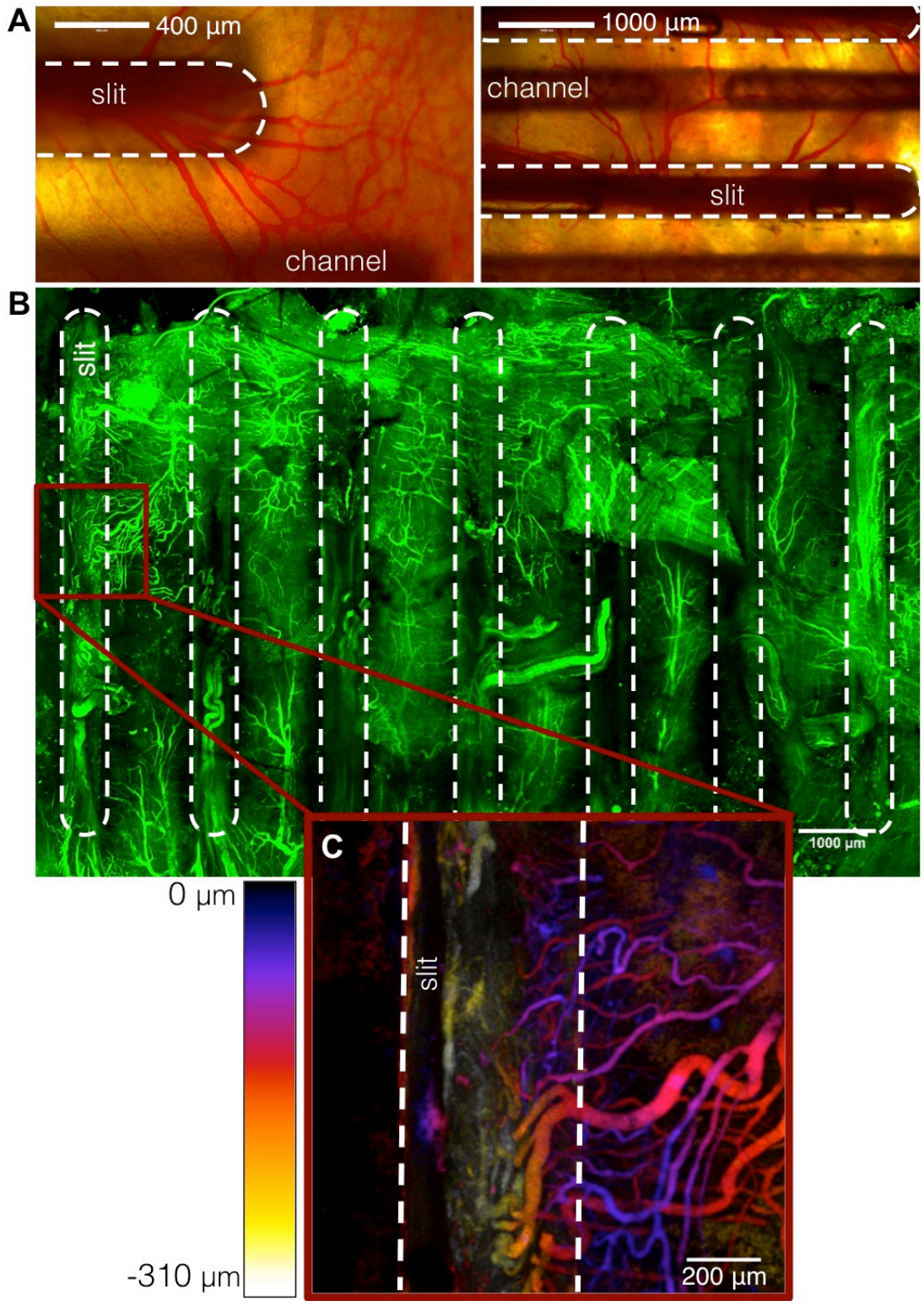

Figure 3.8: Device vascularization and lectin staining.
(A) Three weeks post implantation, fully fabricated devices indicate vasculature diving into the slit space and wrapping around the PDMS devices. Scale bar=400 µm (left) and 1000 µm (right). (B) A maximum intensity projection of the FocusClear-processed device explant with lectin staining shows vascularized tissue surrounding the device 4 weeks post implantation. White dashed lines indicate the slit space. Scale bar=1000 µm. (C) Depth coding of a small portion of the device indicates vasculature diving down into the slit space. Scale bar=200 µm.

3.3.4 Oxygen dynamics

To assess the availability of oxygen to islets within devices *in vivo* and determine the best time for islets to be transplanted, devices with oxygen sensitive tubes were implanted into the subcutaneous space of athymic nude mice and evaluated optically over time. Dynamic inhaled gas tests (DIGTs) were performed at days 3, 7, and every 7 days thereafter for 8 weeks total. Individual DIGTs (Figure 3.9A) measured the lifetime decay values (τ) of the oxygen sensitive devices over the duration of the test and were converted to pO_2 measurements using calibration data. After increasing the inhalation oxygen percentage (room air to 100%), the time until a new steady-state is reached is defined as the *rise time*. The slope of the DIGT curve was calculated: the change in pO_2 increase from the minimum pO_2 measurement to the maximum pO_2 measurement during the rise time. DIGT slopes were plotted over time (Figure 3.9A). Oxygen dynamics were fastest at day 3 and slowly decreased over time reaching a minimum at day 35. Nonparametric Friedman test detected differences between the groups ($p=0.0009$). Post-hoc Dunn's multiple comparisons tests found significant decreases in oxygen dynamics from both day 3 to day 35 and day 7 to day 35 (Figure 3.9C).

PDMS devices were explanted after 8 weeks (56 days) and the surrounding tissue was stained with H&E and immunohistochemically for blood vessel markers, αSMA and CD31 (Figure 3.10). H&E vertical sections (Figure 3.10A) were used for quantifying vessel morphometrics by hand drawing around identified vessels (Figure 3.10B). Immunostaining of the same slit tissue confirmed the presence of vascularized tissue (Figure 3.10C,D)

Quantification of the vascularized slit tissue (Figure 3.11) from H&E slides indicated no significant differences in vessel area percentage or vessel density between individual PDMS devices. Comparing this vessel morphometric data to oxygen dynamics data at day 56 (Figure 3.9B) indicate no obvious correlation. The functional assay may contain information that vessel quantification with histology does not fully capture.

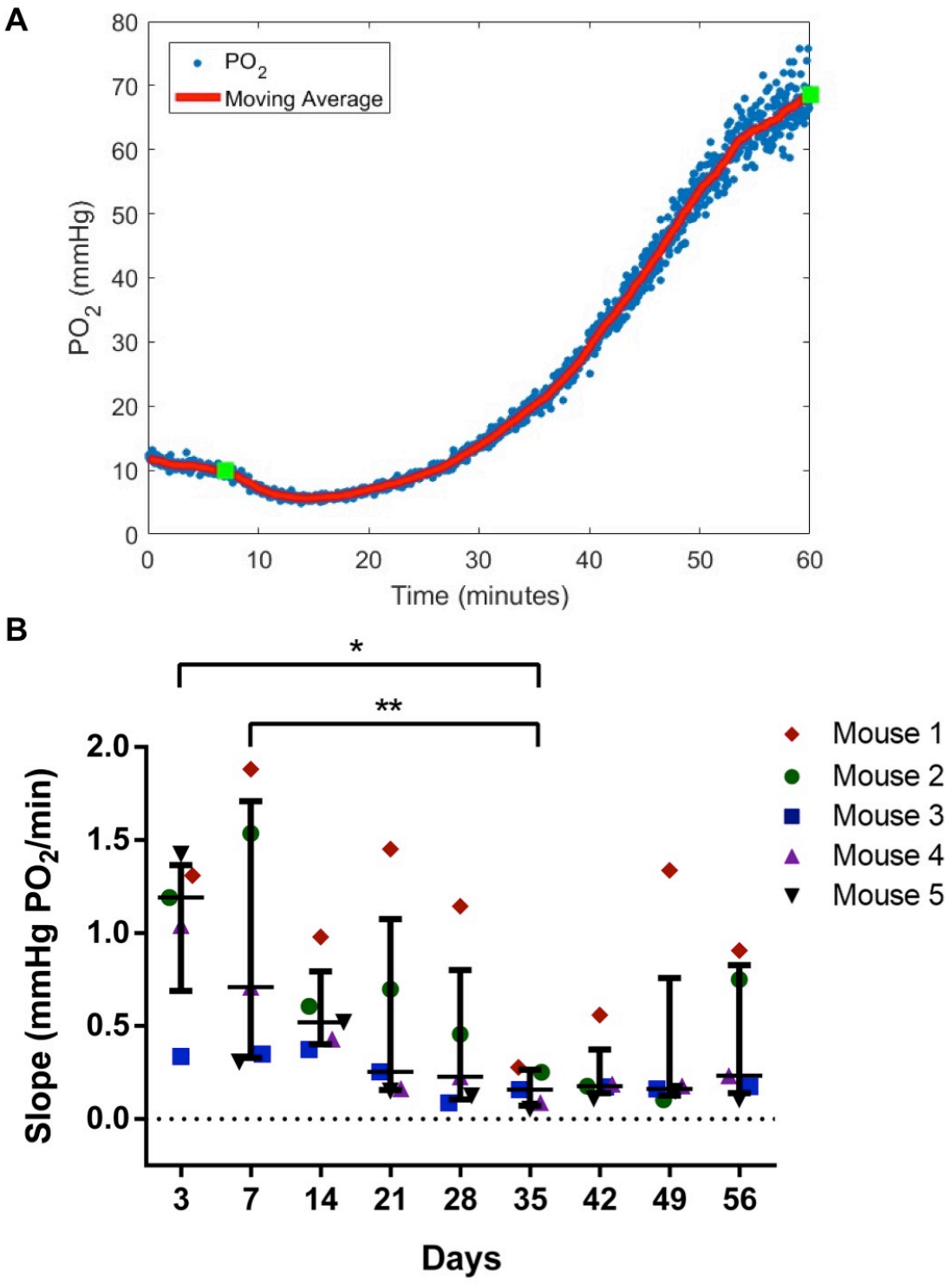

Figure 3.9: Comparison of oxygen dynamics via DIGTs over 8 weeks of noninvasive monitoring. (A) An individual dynamic inhaled gas test (DIGT) after conversion of lifetime decay values (τ) to PO_2 measurements. Time between green boxes indicate the period of time the animal was breathing 100% (760 mmHg) oxygen, also called the *rise time*. (B) During the rise time, slopes from the minimum pO_2 to the maximum pO_2 represent the response rate of the change in oxygen. Individual timepoint comparisons via nonparametric Friedman test and post-hoc Dunn's multiple comparisons test indicate significant decreases in oxygen dynamics from day 3 to day 35 and day 7 to day 35. Data represent median±IQR. Statistical differences are indicated by *$p<0.05$, **$p<0.01$.

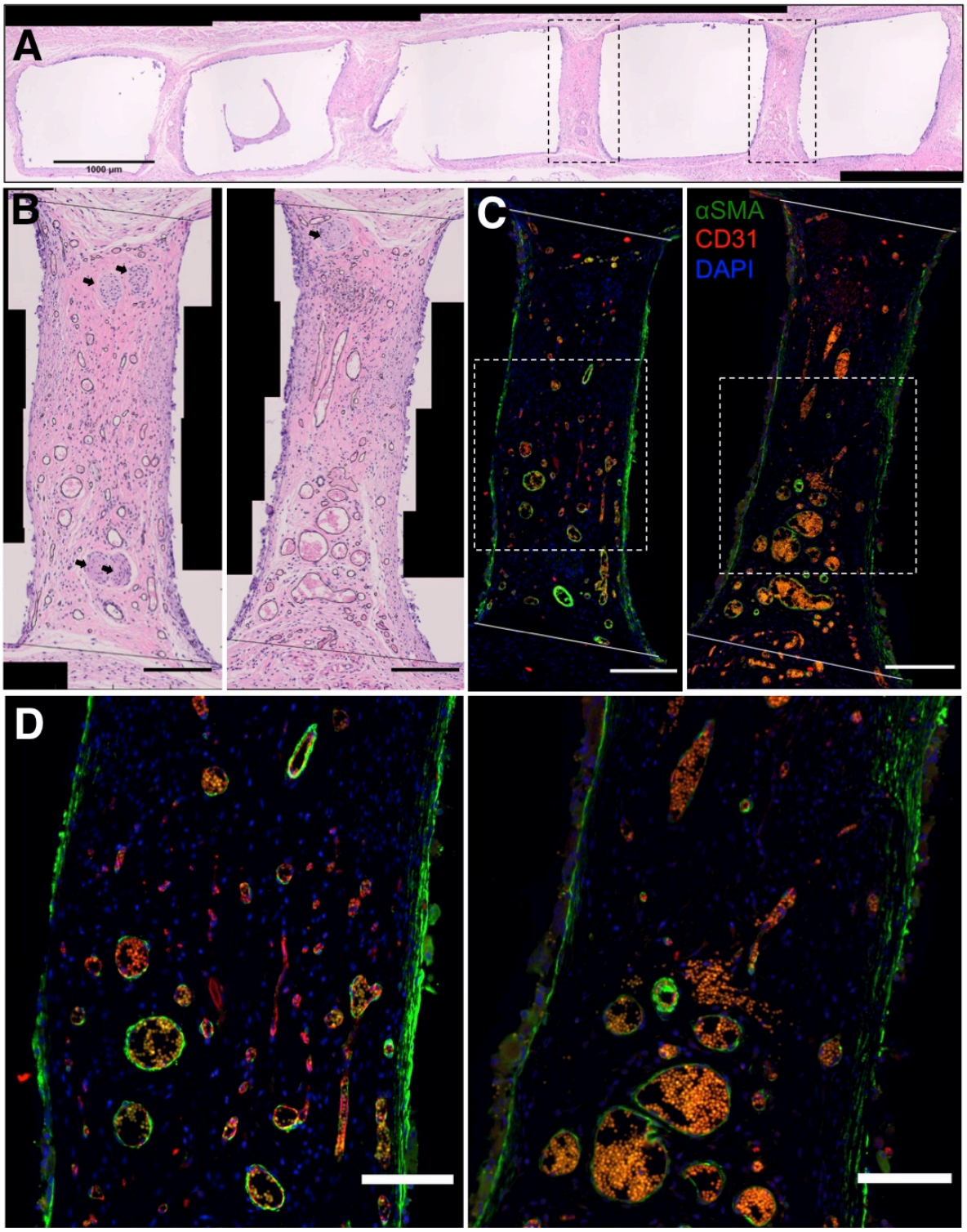

Figure 3.10: Histological analysis of oxygen sensitive device slit tissue 8 weeks post implantation. (A) H&E staining of a vertical section of the tissue surrounding the entire device. Scale bar=1000 µm. Black dashed lines represent (B) close-up views of individual slits with blood vessels outlined in black to get vessel morphometrics. Black arrows signify nerve tissue. Black vertical lines delineate the cut-off area for vessel counting. Scale bar=200 µm. (C) Immunohistochemical staining of the same slit areas of αSMA (green) and CD31 (red) confirms presence of vasculature. Scale bar=200 µm. White dashed lines represent (D) close-up views of the central slit area. Scale bar=100 µm.

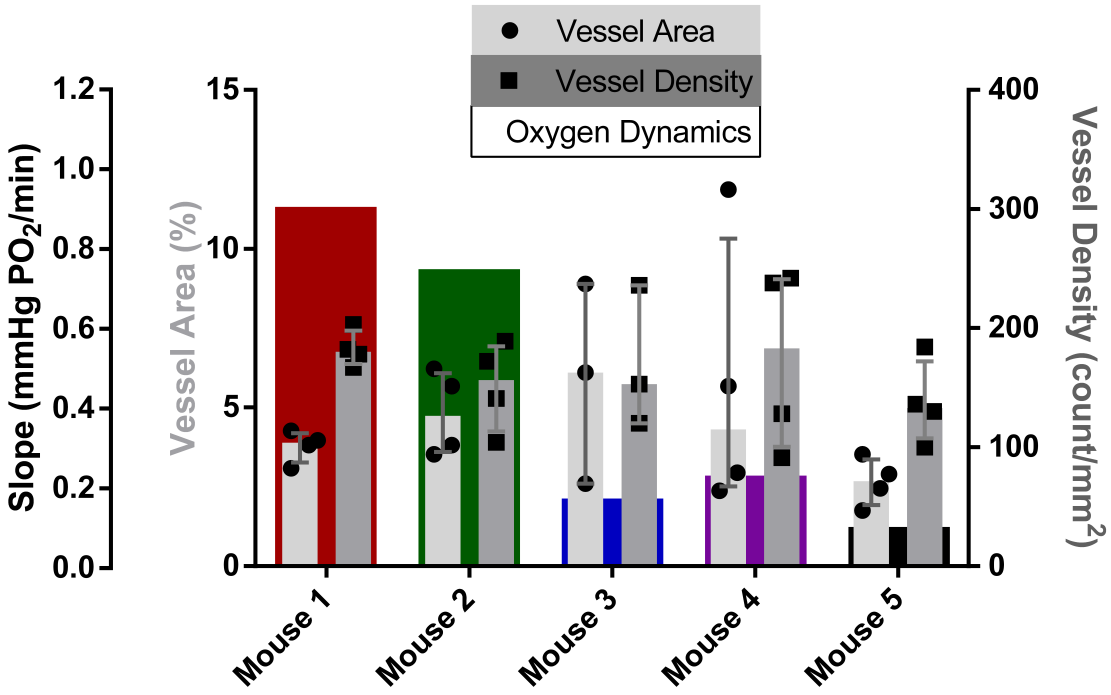

Figure 3.11: Vessel morphometrics and comparison to oxygen dynamics at day 56.
For individual PDMS devices, Kruskal-Wallis test found no statistical differences in terms of both vessel area (white bars) and vessel density (grey bars). Data represent median±IQR. Oxygen dynamics data (colored bars) for each PDMS device from day 56 in Figure 3.9(B) show no obvious correlation with histology data.

3.4 Discussion

Towards creating a vascularized device for islet transplantation in the subcutaneous space, various methods of fabricating PDMS devices, evaluating such devices for their vascularizing properties and oxygen dynamics, and delivering pancreatic islet tissue in a manner that preserves their viability were investigated. PDMS has been used for islet transplantation approaches,[59] making it a suitable material for engineered devices. Utilizing rapid 3D printing prototyping, molds were easily modified to create multiple prototypes of device designs. To minimize nutrient diffusional limitations, small device channels were created. Conventional islet transplantation involves the use of large diameter polyethylene tubing (PE-50, 0.965 mm outer diameter) in both the kidney capsule[98] and the subcutaneous space.[99] This tubing was therefore too large to be implemented in our planar sheet devices. We found small diameter polyimide tubing (PI, 0.300 mm outer diameter) and investigated a novel islet loading method. This loading method produced careful islet

placement close to a single-file configuration. Islet viability in various steps of the loading method was comparable to control islets after 24 hour culture. Particular arrangement of islets in a single-file configuration close to preformed vasculature different from traditional pellet-formation, scattering throughout a scaffold, or clumping together in a macrodevice may result in overcoming islet transplantation issues caused by nutrient diffusion limitations.

Oxygen availability in islet transplantation sites is a widely investigated topic thought to be the main limitation successful engraftment.[100–102] Providing the right amount of oxygen to transplanted islets has been shown to increase insulin secretion and reduce the dose of islets required for diabetes reversal.[103,104] In an *in vivo* prevascularized approach, local vasculature and tissue response to the implant will contribute most to the amount of oxygen the cells will have available to them. *In vivo* implantation and lectin perfusion demonstrated vascularized devices at dimensions that are relevant to future islet transplantation experiments (Section 4.3.4 and 4.3.5). The amount of oxygen provided by this vasculature in the complex *in vivo* microenvironment remains to be investigated. In this study, we created PDMS oxygen sensitive devices that were used to assess oxygen dynamics in the subcutaneous space over 8 weeks post implantation.

A variety of factors contribute to oxygen availability to transplanted cells within macrodevices. Vascularization and inflammatory responses are both at play after implantation of a macrodevice,[105] and balancing these two processes will be crucial in implementing a subcutaneous two-phase approach to islet transplantation. Harnessing the phosphorescent properties of an oxygen-quenching porphyrin dye, oxygen dynamics at the subcutaneous site were monitored noninvasively over time. Right after implantation, oxygen dynamics were fastest, most likely due to initial increased neovascularization and lack of immune cell infiltration.[106,107] As local tissue remodeling takes place, vasculature is pruned[108] and immune cells accumulate on the material forming foreign body giant cells (FBGCs). Formation of an avascular fibrotic collagen capsule that limits oxygen availability takes longer to develop,[106] possibly attributing to the decrease in oxygen dynamics over time. The interplay

between vascularization, wound healing, and oxygen transport dynamics could have implications in identifying not only optimal cell transplantation device designs but also optimal timing of islet transplantation.

3.5 Conclusion

Development of a novel pancreatic islet method loading allowed for single-file placement within 3D print-assisted PDMS housing with preserved viability *in vitro*. Noninvasively measured oxygen dynamics were found to be fastest shortly after implantation and slowed down over a period of 5 weeks. Further studies with devices that are closer in dimensions to those used for islet transplantation (i.e. smaller device channels) are necessary to better understand oxygen dynamics in that particular scenario would be beneficial. Histological correlations at more time points would be useful in distinguishing whether a certain amount of vasculature is necessary to support islet transplantation. Validating oxygen dynamics measurements with subsequent islet transplantation studies would elucidate whether this method is suitable for predicting outcomes of euglycemia.

Chapter 4: Islet Transplantation within Sheet Devices

4.1 Introduction

Pancreatic islet transplantation into the portal vein, also known at the Edmonton Protocol, for the treatment of type 1 diabetes (T1D) has demonstrated superior glycemic control compared to current state-of-the-art methods such as insulin therapy, especially for those suffering from hypoglycemia unawareness.[109] The procedure comes with a variety of risks[110] and gradual graft attrition[111] making it applicable only to those with severe symptoms. Alternative transplantation sites are currently being explored to allow for minimally invasive transplantation approaches and retrievability if the graft fails.[112] Retrievability will be especially important for future implications of stem cell technologies as a safety measure. The subcutaneous space is an attractive transplantation site to provide these benefits. Unfortunately, islet transplantation in the subcutaneous space in particular has been a challenge.

The isolation process renders pancreatic islets disconnected from host vasculature and supporting microenvironment matrix making oxygen delivery and nutrient access more difficult. Receiving 10% of the blood supply, islets compose only 1% of the pancreas,[113] suggesting their highly metabolic nature. Revascularization and vessel density after transplantation in the spleen, kidney, or liver is notably lower that the native pancreas.[114] Additionally, the unmodified subcutaneous space suffers from hypoxia and limited vascularization,[115] exacerbating the lack of oxygen to transplanted islets. Strategies to combat the 'oxygen problem' in the subcutaneous space have included administration of proangiogenic factors, oxygen delivery, cotransplantation of other cell types, and prevascularization approaches.[116] Moreover, these strategies tend to either disperse islets in a scaffold with random vascularization properties or compact islets in a large device potentially inducing necrotic cores and insufficient nutrient exchange. Creating a sufficiently vascularized environment in an engineered manner with precise islet placement may improve the success of subcutaneous islet transplants.

Several attempts at subcutaneous islet transplantation within prevascularized devices that were precisely designed are presented in this chapter. Through iterative

processes of *in vitro* testing and *in vivo* results, modifications were made to enhance device efficacy based off what was learned. The benefits of providing a prevascularized site for xenogeneic islet transplantation under the skin in an immunocompromised STZ mouse model were investigated.

4.2 Materials and methods

4.2.1 Animals

Athymic nude mice (Envigo) at 6-8 weeks old were the recipients of islets from Sprague-Dawley (SD) rat donors. Athymic nude mice were used for two reasons: (1) so comparisons can be drawn from previous studies and (2) because the device does not provide immunoisolation as it is currently fabricated. Recently, the JDRF (formerly Juvenile Diabetes Research Foundation) has called for tissue-integrated devices without encapsulation properties in the hopes of developing the technology more quickly. In parallel, researchers are developing stem cell technologies[117,118] and local immunomodulation approaches[119–121] that can be used in tandem with a macroencapsulation device. All animal experiments were approved under the UC Irvine Institutional Animal Care and Use Committee (IACUC #2008-2850 for experiments 1-4 or AUP-018-038 for experiment 5). Animals were housed at the UCI animal facility and maintained under 12 h light/dark cycles with ad libitum access to water and standard chow.

Induction of diabetes occurred by intraperitoneal injection of 180-200 mg/kg mouse body weight of streptozotocin (STZ) (Sigma-Aldrich) and confirmed by three consecutive days of hyperglycemia (>350 mg/dL) with a blood glucose meter (Bayer® Contour). Insulin-releasing implants (LinBit, LinShin Canada Inc.) were implanted in the subcutaneous space behind the neck to manage blood glucose levels until islet transplantation occurred. As displayed in Figure 4.1, 6 groups throughout the animal experiments were examined: (1) naïve non-diabetic controls (CTRL), (2) diabetic controls (DIA), (3) islets transplanted into the kidney capsule (KC) (positive control), (4) islets transplanted into the subcutaneous space alone (SQ)

(negative control), (5) islets loaded into devices *in situ* after a subcutaneous prevascularization period (PV), (6) subcutaneous nonprevascularized devices (NPV). Complete details of device fabrication can be found in Chapter 3, Section 3.2.1-3.2.2, 3.3.1 and Figure 3.5.

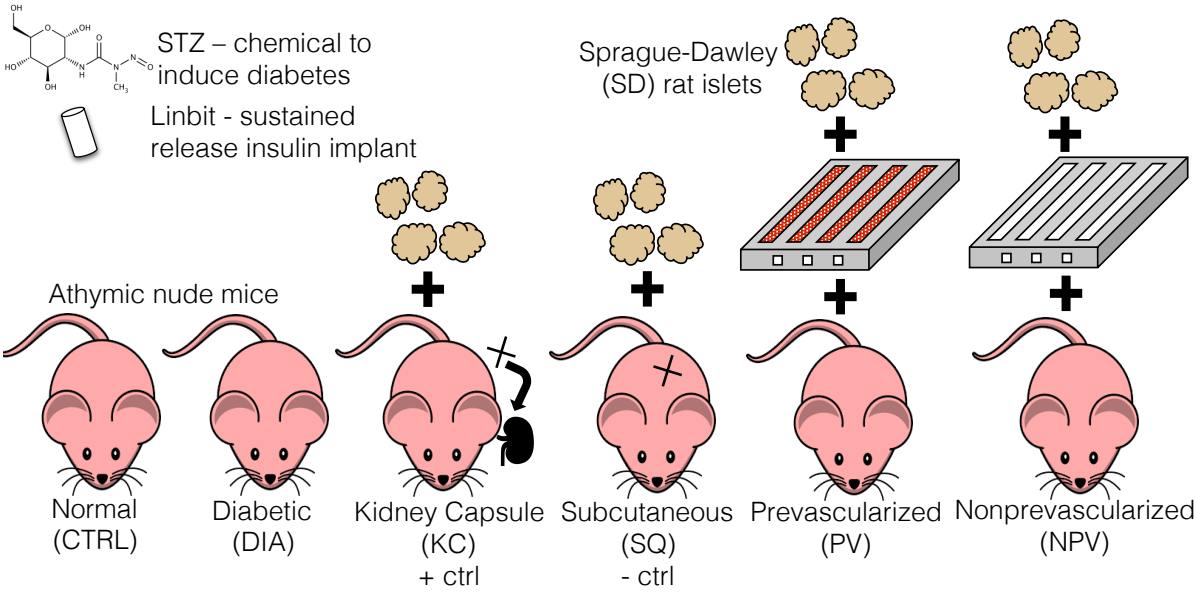

Figure 4.1: In vivo study set-up and groups.

4.2.2 Prevascularized device implantation

Eight to 28 days before transplantation, devices were implanted into the subcutaneous space of nude mice, similar to that of the slit sheets as described in Chapter 2. Briefly, animals were anesthetized with 1-5% isoflurane, and a small incision in the dorsal skin allowed for creation of a pocket large enough for the device to fit. The devices, without any islets but rods inserted into the device channels to prevent tissue ingrowth, were rinsed with saline and placed into the subcutaneous pocket. No external growth factors or reagents were administered or incorporated into the device. The incision was closed with skin glue, sutures, or surgical clips.

4.2.3 Islet transplantation

Sprague-Dawley (SD) rat islets were isolated via collagenase digestion and density purification according to standard techniques[94] and cultured overnight. Two samples from the islet suspension were stained with dithizone (DTZ, MP Biomedical) and counted by islet diameter via brightfield microscopy (EVOS) and ImageJ to achieve

islet equivalent (IE) counts. SD rat islets received were courtesy of Lakey laboratory in UCI Department of Surgery (experiments 1-4) or purchased and shipped from Joslin Diabetes Center (experiment 5) in Boston. On transplantation day, animals were anesthetized with 0.5-5% isoflurane.

For kidney capsule transplants, established techniques were used.[122] Briefly, a small incision was made through the skin and the peritoneum. After exposing the kidney, a small nick in the capsule was made with a 25G needle followed by insertion of a small glass pasteur pipette with a curved tip to make a small pocket. Aliquotted islets in an Eppendorf tube were aspirated into PE-50 tubing (Becton Dickinson) with a 23G Hamilton syringe. The tubing was inserted into a 50 mL conical tube and centrifuged at 1000 rpm to form a pellet. The tubing was then cut at the edge of the pellet and inserted into the kidney capsule pocket. The syringe was pressed slowly while withdrawing the tubing to release the islets under the kidney capsule. The kidney capsule incision was cauterized and the kidney was gently pushed back into the retroperitoneum prior to closing the muscle layer with sutures (3-0 silk) and the skin with surgical clips. An injection of buprenorphine was administered intramuscularly.

For subcutaneous only transplants (no device), a small incision in the skin allowed for creation of a pocket large enough to fit PE-50 tubing (~2 mm). Exactly as done for kidney capsule transplants, aliquotted islets were transferred to PE-50 tubing and centrifuged to form a pellet. The tubing was cut at the pellet edge and inserted into the subcutaneous pocket. The syringe was pressed slowly while withdrawing the tubing to release the islets into the subcutaneous pocket. The pocket was secured with surgical clips.

For nonprevascularized device transplants, devices were loaded with islets as described in Chapter 3. Briefly, aliquotted islets from a petri dish were aspirated either via the first-generation loading method (Section 3.2.4): (1) directly into 1 mL syringes with 22G needles (experiments 1-2) or via the second generation loading method (Section 3.2.5): (2) into PI tubing using a custom apparatus with attached needle and syringe (experiments 3-5). Syringes (1) or PI tubes filled with islets under

an EVOS scope (2) were inserted into device channels. The channels were loaded with islets by (1) pushing them directly out with the syringe (experiments 1-2) or (2) pushing them slowly out as the PI tubes were withdrawn (experiments 3-5). In some cases, PI tubing attached directly to a 31G needle and syringe was used for more efficient loading. The loaded device with islets was then implanted similarly to prevascularized devices as described in the previous section.

For prevascularized device transplants, the previously implanted devices were re-accessed by making a small incision at the channel openings. The inserted rods to prevent tissue ingrowth were removed with tweezers. Then, as done for the nonprevascularized case, either (1) 1 mL syringes or (2) PI tubes filled with islets were inserted into the device channels. Islets were (1) directly released into the channel space (experiments 1-2) or (2) gently released as the PI tubing was withdrawn back (experiments 3-5). Islets were distributed over all channels within the device. For experiment 5, fibrin was added to provide mechanical support to the islets and enhance channel vascularization in prevascularized devices. Lyophilized bovine fibrinogen (Sigma-Aldrich) was rehydrated in PBS with calcium and magnesium (Life Technologies). Reconstituted protein was added to the aliquotted islet dish with Hank's Balanced Salt Solution (Corning) at a final concentration of 2.5 mg/mL. Right before loading, bovine thrombin (Sigma-Aldrich) was added to the islet-fibrinogen solution at a concentration of 0.004 U/mL to initiate the polymerization reaction, but at a very slow rate (>5 hr, data not shown).

All incisions in the skin were closed with skin glue, sutures, and/or surgical clips. All animals were given ibuprofen for 5 days following transplants. Blood glucose and body weight were monitored daily and weekly, respectively, immediately after transplantation for two weeks in the morning with a blood glucose meter (Bayer® Contour) and scale (Ohaus®), respectively. Blood glucose (BG) monitoring declined to 2-3 times per week for the duration of the experiment. Animals were considered normoglycemic if readings reached <200 mg/dL and remained for the duration of the experiment.

4.2.4 Intraperitoneal Glucose Tolerance Test (IPGTT)

Mice were fasted for 8-16 hours and injected intraperitoneally with a 25G needle at a dose of 2-3 g glucose (Sigma-Aldrich)/kg mouse body weight. Blood glucose was measured at 10, 30, 60, 90 and 120 min after bolus injection. Time versus blood glucose levels and area under the curve (AUC) values were plotted.

4.2.5 C-peptide measurements

Before explantation of grafts, the mice undergo blood collection via the retro-orbital sinus. Mice were anesthetized with 1-5% isoflurane and the skin around the head and neck was secured in the thumb and middle finger to stabilize the head. The tip of a capillary tube (Kimble) was inserted with gentle pressure and rotation into retro-orbital sinus membrane. Additionally at time of sacrifice, blood was also collected from the heart using a 25G needle. Once punctured, the blood was collected into an Eppendorf tube. After 30 minutes, a clot was formed and the sample was centrifuged at 4°C for 10 minutes at 2700 rpm. At time of sacrifice, blood was also collected from the heart using a 25G needle. Serum samples were stored in the freezer at -20°C until measurement by ELISA for rat C-peptide (Mercodia) could be performed. The assay is described to have only 6% cross-reactivity with mouse C-peptide. C-peptide is a short polypeptide connecting the alpha and beta chains together within the proinsulin molecule. C-peptide is then cleaved from proinsulin creating insulin. Insulin clearance by the liver is large and variable, while C-peptide is not.[123] Measuring C-peptide can indicate graft insulin secretion even if BG levels remain high.

4.2.6 Graft explantation and histology

To confirm graft dependent euglycemia and eliminate native pancreatic regeneration, grafts were explanted either by nephrectomy or subcutaneous graft excision. Animals were monitored for 2 days following graft removal to confirm return to hyperglycemia. Explanted grafts were fixed in 10% phosphate buffered formalin for at least 24 h. Because PDMS is difficult to section through, device tissue samples went through post-processing steps to separate the tissue from the silicone

material. One end of the device was cut with a fresh microtome blade (SHURSharp™, Triangle Biomedical Sciences, Inc.). The surrounding fixed tissue was slid off of the device, leaving the surrounding slit tissue intact. PDMS devices were opened by separating the floor piece from the ceiling piece to expose the tissue within the channels. Channel tissue was lifted from the device by pouring heated 2% agarose (Sigma-Aldrich) over the top of the floor piece. The soft agarose gel was then lifted from the PDMS. Another agarose layer to encase the tissue was placed on top of the lifted piece. Alternatively, braids were removed from the open-faced PDMS pieces and placed side-by-side in a plastic Cryomold® (TissueTek®) and filled with 2% agarose. Tissue samples were processed, blocked in paraffin, and sectioned into 4 µm sections by JIT labs. Samples were stained with H&E as well as immunohistochemically (IHC). A list of primary antibodies used for IHC staining is shown below in Table 4.1. A list of secondary antibodies used is shown in Table 4.2. IHC was performed similarly to that as described in Chapter 2.

Table 4.1: List of primary antibodies used for IHC staining of explanted grafts.

Antigen	Host	Clonality	Company	Cat #
insulin	Rabbit	monoclonal	Abcam	ab181547
insulin	Guinea pig	polyclonal	Abcam	ab7842
glucagon	Rabbit	monoclonal	Abcam	ab92517
CD31	Goat	polyclonal	Santa Cruz	sc-1506
F4/80	Rat	monoclonal	eBioscience	14-4801-85
CD206 (MMR)	Goat	polyclonal	R&D Systems	AF2535

Table 4.2: List of secondary antibodies used for IHC staining of explanted grafts.

	Host	Fluorophore	Company	Cat #
anti-rabbit	Donkey	Alexa Fluor 488	Life Technologies	A21206
anti-rat	Donkey	Alexa Fluor 488	Life Technologies	A21208
anti-goat	Donkey	Alexa Fluor 594	Jackson ImmunoResearch	705-585-147
anti-guinea pig	Donkey	Alexa Fluor 647	Jackson ImmunoResearch	706-605-148

4.2.7 Islet immunohistochemistry

Antigen retrieval was performed by submersion of deparaffinized and rehydrated slides into 0.1M Tris/HCl buffer, pH=9, overnight at 80°C. Slides were washed with PBS (Lonza), permeabilized with 0.5% Triton X-100 (Arcos Organics) and blocked with 5% donkey serum (Jackson ImmunoResearch) for 60 min at room temperature. Slides were incubated with 1:300 monoclonal rabbit anti-insulin (Abcam) (experiment 4) or 1:100 polyclonal guinea pig anti-insulin (Abcam), 1:8000 monoclonal rabbit anti-glucagon (Abcam), and polyclonal goat CD31 (Santa Cruz Biotechnology) (experiment 5) in 5% donkey serum and 0.5% Triton X-100 in PBS overnight at 4°C. Slides were washed with PBS and incubated with secondary antibodies in PBS: 1:500 AlexaFluor 488 donkey anti-rabbit (Life Technologies), 1:400 AlexaFluor 594 donkey anti-goat (Jackson ImmunoResearch), and 1:400 AlexaFluor 647 donkey anti-guinea pig (Jackson ImmunoResearch) for 1 h at room temperature. Counter staining was performed by incubation with 1:3000 DAPI (Invitrogen) for 10 min.

Slides from experiment 4 were imaged on an Olympus IX-83 microscope with a 20× air objective and an Orca R2 camera (Hamamatsu Photonics) through Micro Manager[70] and stitched together using Fiji.[97]

Slides from experiment 5 were imaged on a laser-scanning confocal microscope (Olympus FluoView FV3000) with a 20× air objective (PlanApo, NA: 0.75, WD: 0.65 mm). Solid-state laser lines of 405 nm, 488 nm, 561 nm, and 640 nm were used to

excite their respective fluorophores and images were captured with FV31S-SW software.

4.2.8 Macrophage immunohistochemistry

Antigen retrieval was performed by incubating tissue sections in citrate solution, pH=6 (Dako) in a steam cooker (Black&Decker) for 30 min. Tissue sections were permeabilized and blocked as described above. Slides were then incubated with 1:100 monoclonal rat anti-F4/80 (BM8, eBioscience) as a pan-macrophage marker[124,125] and 1:100 polyclonal goat anti-cluster of differentiation 206 (CD206, R&D Systems) for labeling of alternatively activated M2 macrophages[126,127] in PBS supplemented with 5% donkey serum and 0.5% Triton X-100 at 4°C overnight. Slides were washed with PBS and incubated with 1:400 AlexaFluor 488 donkey anti-rat (Life Technologies) and 1:400 AlexaFluor 594 donkey anti-goat (Jackson ImmunoResearch). Counter staining for cell nuclei was performed by incubating all slides with 1:3000 DAPI (Invitrogen) for 10 min. Images of stained slides were acquired on the same system as the experiment 4 slides described in the previous section.

4.2.9 Data display and statistics

All data from islet transplantation was graphed and statistics were completed in GraphPad Prism 6. One-way ANOVA was calculated with Holm-Sidak *post-hoc* testing for multiple comparisons between groups. Data represent means and all error bars represent SEM unless otherwise stated. Statistics were not performed if data contained less than 3 individuals per group.

4.2.10 Device modeling

In collaboration with Dr. Anna Grosberg in the UCI Department of Biomedical Engineering, modeling of the latest device prototype was implemented in MATLAB (MathWorks).

4.3 Results

4.3.1 Experiment 1

In the first transplantation experiment, the conditions of prevascularized and nonprevascularized were tested in athymic nude mice at a dose of 2500 and 2825 islet equivalents (IE), respectively. Islets were injected with a syringe (old method) directly into the channels of large devices (~20 mm x 30 mm x 1 mm, 8 channels, Appendix Figure A.2) fabricated with early prototype techniques (Section 3.2.1). Nonprevascularized devices achieved some glucose control initially, but quickly returned to hyperglycemia (Figure 4.2A) over a course of 7 days. It is hypothesized that the pre-loaded islets failed slowly over time due to lack of vascularization into the device. Prevascularized devices (8 day prevascularization period) achieved lower glucose levels for 21 and 11 days in mouse 1 and mouse 2, respectively (Figure 4.2B). Mouse 1 showed initial blood glucose instability but reached lower, stable levels after 7 days for the duration of the study. An intraperitoneal glucose tolerance test (IPGTT) at a dose of 3 g glucose/kg body weight of mouse 1, diabetic, and non-diabetic controls indicate that the device produces similar insulin dynamics to that of the naïve mouse, both much improved over the diabetic mouse (Figure 4.2C).

This first experiment provides preliminary evidence that islets transplanted into prevascularized devices in the subcutaneous space can improve blood glucose control in diabetic mice; however, the number of animals is insufficient to draw firm conclusions. The large device size hindered healing and wound closure. Thus, a second transplant experiment with smaller devices was performed.

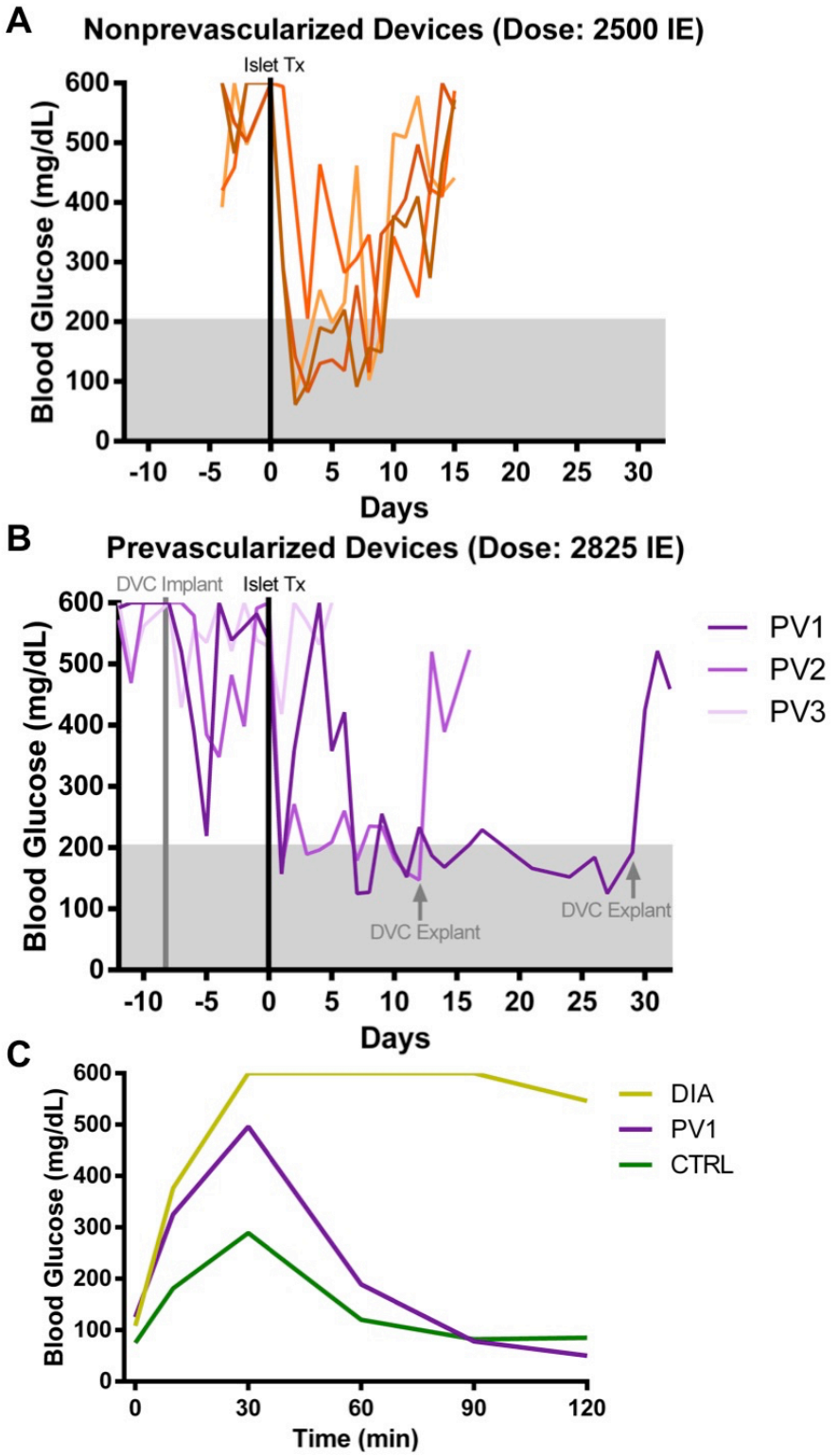

Figure 4.2: Blood glucose profiles and IPGTT of first experiment of islet transplant recipients. (A) Nonprevascularized (NPV) devices achieved lower blood glucose levels for a period of 7 days, but eventually lose glucose control. (B) Prevascularized (PV) devices (8-day prevascularization period) achieved lower blood glucose levels (after some initial fluctuations in mouse 1) until devices were explanted. (C) The IPGTT of mice administered with 3 g glucose/kg body weight after 8 h fast indicates the prevascularized device can achieve similar insulin release kinetics to the non-diabetic mouse (CTRL).

4.3.2 Experiment 2

The second experiment included more transplant groups: nonprevascularized (NPV), prevascularized (PV), kidney capsule (KC), subcutaneous (SQ), and non-diabetic controls (CTRL). The devices were refined from the first experiment to be smaller (~15 mm x 18.5 mm x 1 mm, 8 channels, Appendix Figure A.3) to improve healing but still made with early prototype fabrication techniques (Section 3.2.1). PV devices had a prevascularization period of 14 days. A dose of 1100 IE was transplanted into each group. The nonfasting blood glucose (NFBG) values of NPV devices (n=4) (Figure 4.3A, top left) demonstrated a slight lowering in the initial 10 days following transplantation. Eventually over the course of the 60-day experiment, BG levels remained high. Blood glucose levels of PV devices (n=4) (Figure 4.3A, top right) did not show any initial lowering or response to islet transplant. Animals did not survive past day 15 post-transplantation. Animals in the KC group (n=3) (Figure 4.3A, middle left) demonstrated lowered BG levels within 5 days of transplant and maintained euglycemia until nephrectomy was performed and glucose levels returned to hyperglycemic levels. Blood glucose levels in the SQ group (n=4) (Figure 4.3A, middle right) showed similar trends to the NPV group with initial lowering in some animals and gradual rise. Non-diabetic control mice (n=3) (Figure 4.3, bottom left) showed euglycemic levels throughout the duration of the experiment as expected. Average blood glucose values of each group were plotted together (Figure 4.3B) indicating non-function of NPV, PV, and SQ groups and euglycemia in CTRL and KC groups.

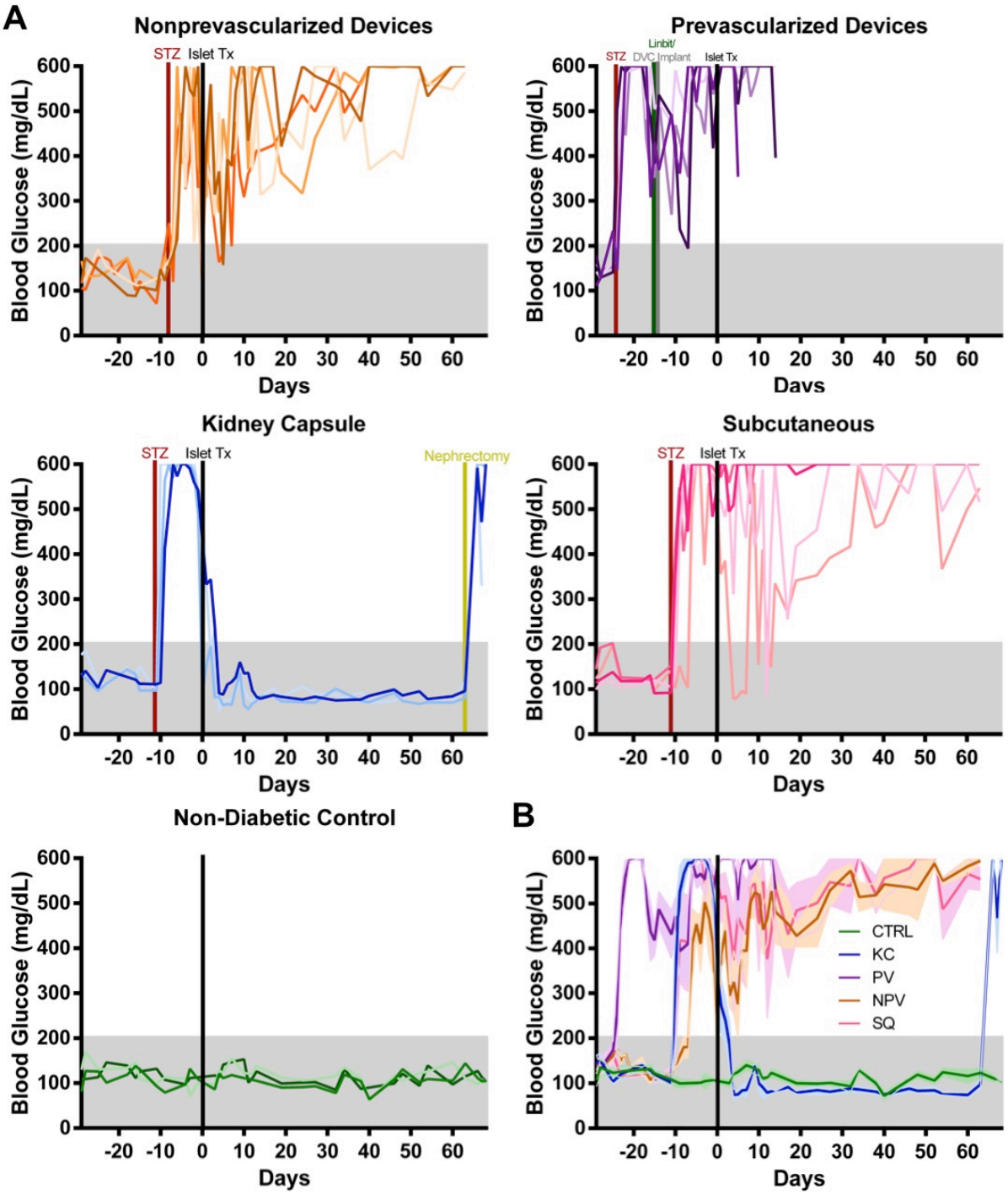

Figure 4.3: Blood glucose profiles of nude mice in second transplant study.
(A) Nonfasting blood glucose profiles of individual mice in each group: nonprevascularized (NPV, orange), prevascularized (PV, purple), kidney capsule (KC, blue), subcutaneous (SQ, pink), and non-diabetic controls (CTRL, green) are shown. All islet transplant recipients received a doses of ~1100 IE. Each individual line represents an individual athymic nude mouse. PV devices had a prevascularization period of 14 d; yet, animals did not survive past day 20. NPV and SQ transplant groups show similar results with initial lowering and eventual failure. The KC group maintained euglycemia for 60 days until nephrectomy was performed with subsequent high blood glucose values. Non-diabetic CTRL mice also maintained euglycemia as expected. (B) Average blood glucose values of all groups are displayed. Shading around each line indicates SEM.

At 4-5 weeks post-transplantation, an IPGTT at a dose of 3 g glucose/kg body weight was performed in all remaining mice. The NPV group (Figure 4.4A, top left) displayed peculiar results with initial high values at the beginning of the test but eventual lowering over the 2 h period. This result may indicate either residual native pancreas function or delayed response of the graft that may be difficult to discern in the nonfasting state. The KC (Figure 4.4A, top right) and CTRL groups (Figure 4.4A, middle left) showed glucose clearance curves consistent with expected results of initial increase to maximum BG values after 30 min and return to normal levels after 2 h from the initial bolus. A majority of the SQ group (Figure 4.4A, middle right) animals also displayed high glucose levels for the duration of the experiment. Average IPGTT curves (Figure 4.4B) and subsequent area under the curve (AUC) values were calculated (Figure 4.4C). Glucose profiles for the SQ group were the worst of all groups.

With the results of this experiment and paired *in vitro* experiments, it was determined that the first generation loading method of needle and syringe may be causing significant damage to the islets. For subsequent *in vivo* experiments, device loading and fabrication methods were improved.

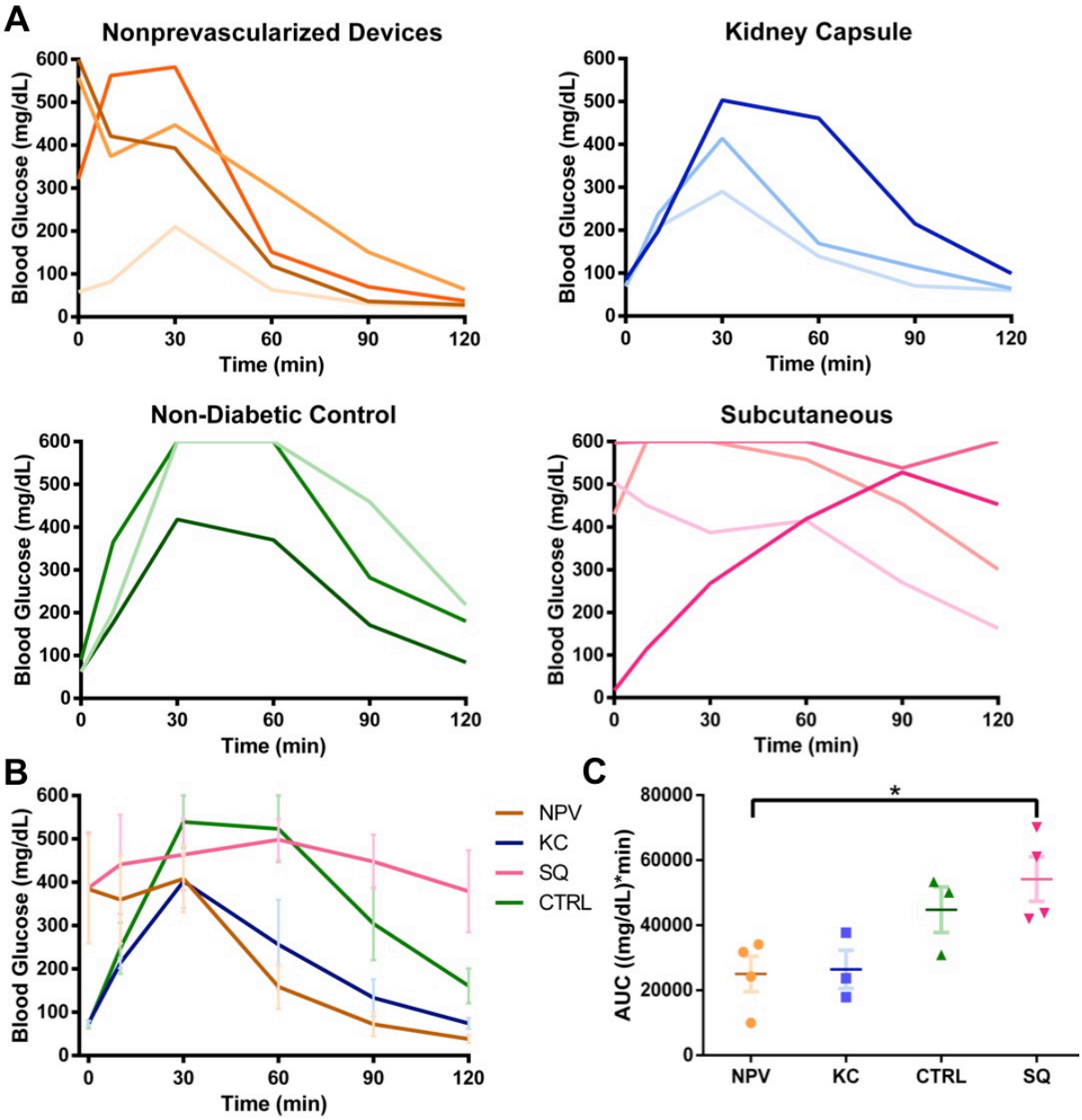

Figure 4.4: IPGTT results of second transplant experiment recipients.
(A) IPGTT at a dose of 3 g glucose/kg body weight after 16 h fast results of individual mice within each transplant group: nonprevascularized (orange), non-diabetic control (green), kidney capsule (blue), and subcutaneous (pink) 4-5 weeks post transplantation. (B) Average IPGTT results of each group. (C) Area under the curve calculations for each group. Error bars represent SEM. Statistical differences via one-way ANOVA with *post-hoc* Holm-Sidak testing for multiple comparisons are indicated by *p<0.05.

4.3.3 Experiment 3

The third experiment employed implantation of two even smaller devices (10 mm x 14.5 mm x 1 mm, 6 channels, Appendix Figure A.4-A.5) at a dose of 800 IE each for a total of 1600 IE per animal and the new PI tubing loading method. The devices

tested in this experiment were made with the later prototype device fabrication methods (Section 3.2.2) with the incorporation of PEEK braids to prevent islet loss outside of the device channels and slit alignment to prevent irregularities with cutting the PDMS material. In the previous two islet transplant experiments, STZ diabetes induction occurred prior to device implantation. It was hypothesized that the prolonged diabetic state (e.g. body weight loss and weakened condition) was compromising the ability of the islet graft to reverse the disease. In experiment 3, we investigated STZ induction after device implantation. A prevascularization period of 28 days was investigated. NFBG levels (Figure 4.5) of 4 mice indicate varied results. Two mice (PV1, PV2) died shortly after STZ induction. STZ is known to sometimes cause high rates of mortality.[128] Of the remaining two mice, PV3 died after islet transplantation most likely due to infection. On the other hand, PV4 showed glycemic control for 7 days after an initial 7-day stabilization period. The mouse was

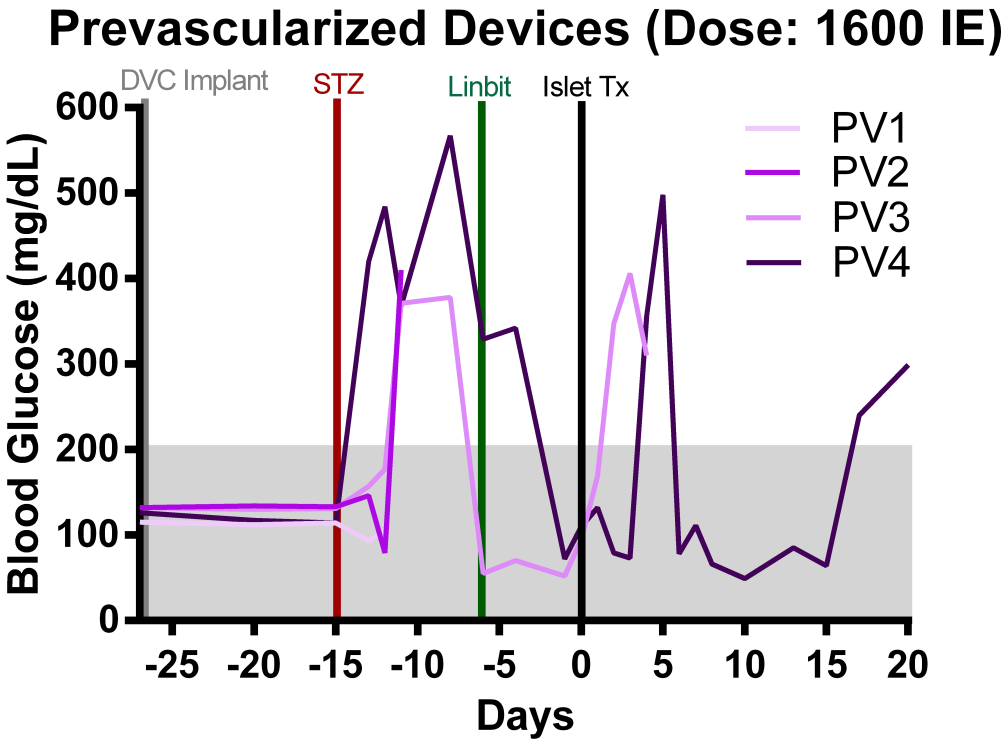

Figure 4.5: Blood glucose values of four PV mice in third transplantation experiment.
Mice were initially implanted with devices 28 d prior to islet transplantation. Two mice (PV1, PV2) implanted with devices died shortly after STZ injection. After islet transplantation (1600 IE) PV3 died within 4 days, most likely from infection. PV showed glycemic control for 7 days until the animal had to be sacrificed due to insufficient healing.

sacrificed due to incomplete healing and risk of further infection. It was determined that device implantation prior to STZ induction should be avoided and implantation of only one small device would encourage sufficient healing. Other changes like rounded device edges and an addition of a 'ceiling flap' to cover the inserted rods and prevent them from protruding up through the epidermis would also be beneficial.

4.3.4 Experiment 4

The fourth experiment included only one device per animal for better healing in the NPV (n=5) and PV (n=5) groups at two different doses (800 IE and 1200 IE). These dosages were based off another group developing a prevascularized subcutaneous islet transplantation scaffold using the same animal model.[40] Devices (13.3 mm x 13.3 mm x 1 mm, 6 channels) made with later prototype fabrication techniques (Section 3.2.2) also incorporated rounded edges and an extended ceiling flap (Appendix Figure A.6-A.7) to cover the prevascularization rods and to prevent device protrusion. BG levels for NPV mice (Figure 4.6A, top) for both doses showed similar trends to previous experiments with hyperglycemic levels for the experiment duration. BG levels for PV mice (Figure 4.6A, bottom) had STZ induction prior to a 28-day prevascularization period. Linbits provided glucose control during this period. Two mice (PV4 and PV5) had generally lower NFBG levels and longer survival times but no mice achieved euglycemia. Healing of the device was much improved with no complications compared to previous experiments.

IPGTT of PV mice (Figure 4.6B) 21 days post islet transplantation at a dose of 2 g glucose/kg body weight resulted in unexpected results. PV1 and PV5 indicate some glucose clearance ability. This result may be due to some residual function within the native pancreas or delayed glucose control that is difficult to discern in the nonfasting regime. Rat C-peptide measurements (Figure 4.6C) at sacrifice showed minimal levels in all animals indicating minimal graft function.

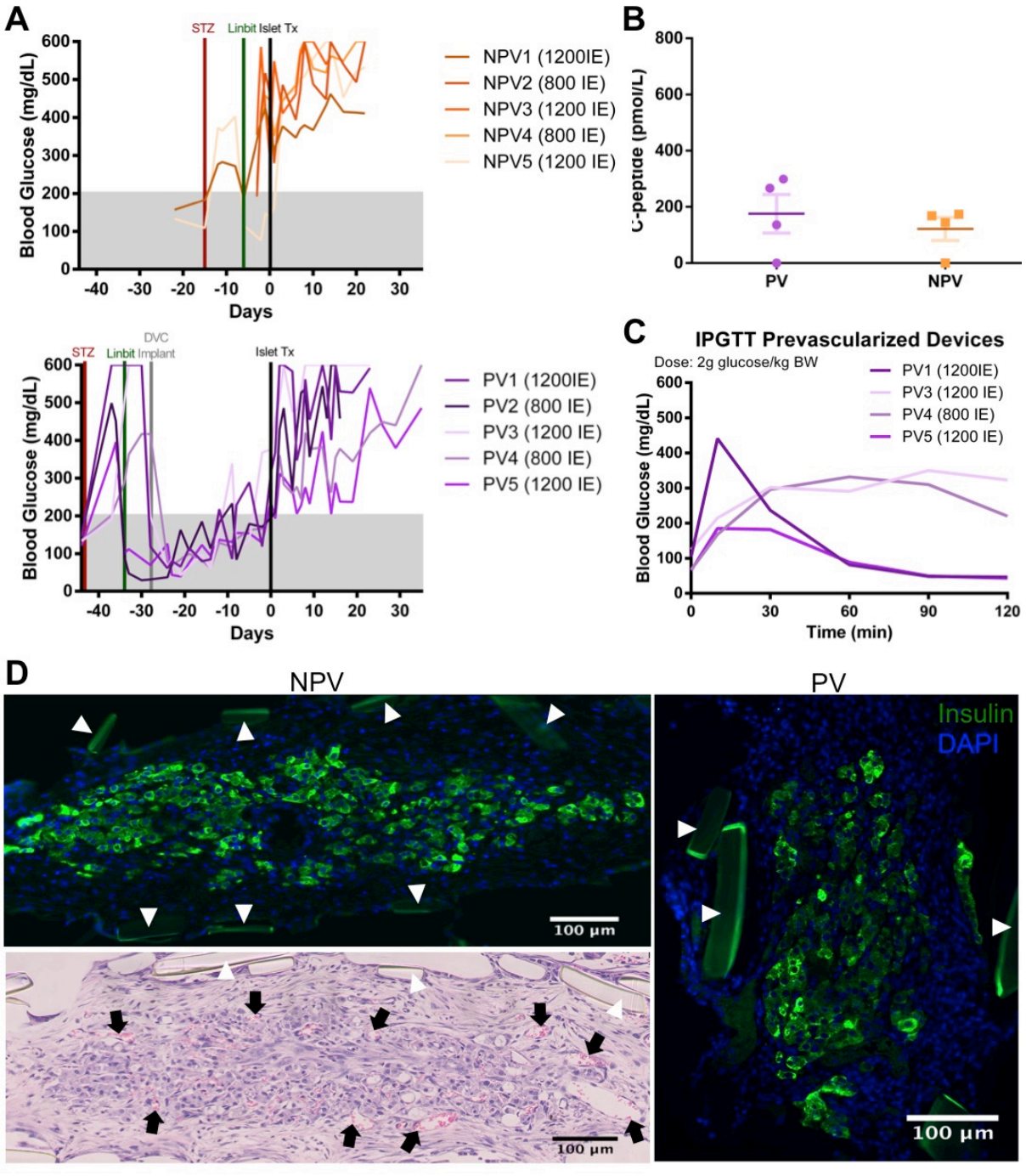

Figure 4.6: Results from fourth islet transplant experiment.
(A) Nonfasting blood glucose values of nonprevascularized (NPV, top) and prevascularized (PV, bottom) show gradual increase of glucose values over a period of 30 days after islet transplantation of either 1200 or 800 IE. Each individual line represents an individual mouse. (B) After 16 h fast with a dose of 2 g glucose/kg body weight, IPGTT at 3 weeks post transplant demonstrates some grafts may have residual function. Data represent mean±SEM. (C) Rat C-peptide measurements show very little concentrations in the serum from these animals. (D) Insulin (green) staining and DAPI counterstaining (blue) of the tissue within the channels of NPV devices (top) was evident with corresponding H&E staining (bottom) of the same area. White arrows point to the PEEK braid material. Black arrows point to blood vessels. PV device channels also indicate some insulin positive cells. Scale bars=100 µm.

To determine if islets within devices showed any insulin production, immunohistochemical (IHC) staining was performed (Figure 4.6D). In both the NPV (Figure 4.6D, top left) and PV (Figure 4.6D, right) cases, insulin positive beta cells (green) were found within the braid-reinforced channels (white arrows). Matching H&E staining (Figure 4.6D, bottom left) of the same area within the NPV device indicate local microvasculature (black arrows). However, a majority of scaffolds showed no intact islets suggesting that while some islet species can survive and produce insulin within devices, it may not be sufficient for nonfasting glucose control. Additionally, the insulin-positive islets within device channels were dispersed and have lost their characteristic compact spherical morphology that is typically seen within the native pancreas.

To investigate possible reasons for why euglycemia was not achieved in either the NPV or PV groups, IHC staining for macrophages was performed (Figure 4.7). The foreign body response (FBR) to an implanted material has a significant effect on the functionality of that material and anything incorporated within it.[129,130] PDMS is a widely used biomaterial approved by the US Food and Drug Administration (FDA) for a variety of medical devices. It is also known that not only the chemical composition but also the structural composition (e.g. implant size,[131] pores,[132] grooves,[133] smoothness[134]) of a material plays a vital role in the FBR. Devices are composed of medical grade PDMS but also have an inherent roughness due to the 3D printed prototyping method. Molds utilized for device fabrication are formed layer-by-layer leaving a "sawtooth" pattern behind and are not completely smooth. Fluorescent imaging of the slit space in NPV (Figure 4.7A) and PV (Figure 4.7B) devices display a pan-macrophage marker (F4/80, green) and a "pro-healing" or M2 alternatively activated marker (CD206, red).[135] The images indicate a substantial amount of macrophages at the tissue-implant boundary (white dashed lines), with a majority of them lacking staining for the M2 pro-healing marker, suggesting that most macrophages present probably take on a M1 "pro-inflammatory" classically activated phenotype. M2 pro-healing macrophages tended to be only located within

the center portions of the slit while other macrophage subtypes localize to the boundary. Foreign body giant cells (FBGCs) also appear to be evident at the implant boundary (Figure 4.7B left, white arrows). The aggressive response by the immune system to the implant indicates an impaired immune response that may be preventing adequate nutrient diffusion to the transplanted cells within the devices.

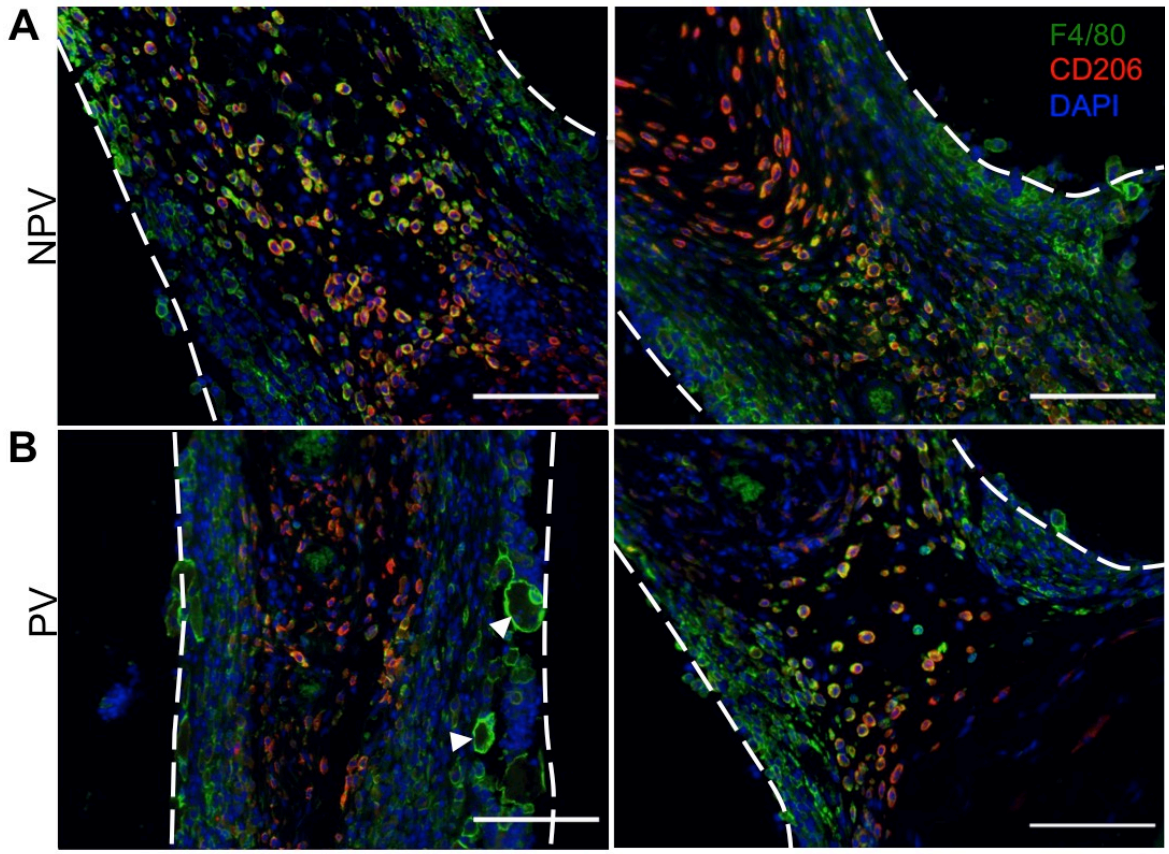

Figure 4.7: Macrophage immunohistochemistry staining in device slit tissue.
Tissue within the slit space of (A) NPV and (B) PV devices indicate macrophage infiltration via the pan-macrophage marker F4/80 (green) and M2 alternatively activated 'pro-healing' macrophage marker CD206 (red). DAPI counterstaining (blue) shows cell nuclei. White arrows indicate FBGCs. Dashed white lines denote the material-tissue interface. Scale bars=100 μm.

Although a new islet loading technique and improved device design was implemented, euglycemia in diabetic animals with a prevascularized device was not achieved. It was hypothesized that the implanted islets may not receive enough support or vasculature during islet loading and shortly after transplantation, respectively. Fibrin, a protein involved in the clotting cascade, is well-known for its vascularizing properties.[136] Incorporation of fibrin during islet loading as well as a larger islet dose was investigated in the next experiment.

4.3.5 Experiment 5

The fifth and final experiment included addition of fibrin to the islet medium to help support the cells during implantation and promote vascularization within the device channels. Devices (13.3 mm x 13.3 mm x 1 mm, 6 channels, Appendix Figure A.6-A.7) were made with the exact same dimensions and fabrication methods as islet transplant experiment 4. A prevascularization period of 12 days and an islet dose of 2000 IE in the PV group (n=4) was used to mimic similar doses used in the first islet transplant experiment and compared to the KC group (n=2) with a dose of 500 IE. Glucose measurements in KC mice (Figure 4.8A) and PV mice (Figure 4.8B) were taken over the duration of the 100+ day experiment. Both KC mice demonstrated euglycemia for the entire period after transplantation; however, nephrectomy did not return glucose values to hyperglycemic levels. This result indicates that endogenous pancreatic islet function was regained which has been documented to occur.[137] For PV mice, all devices healed properly; however, varied results were observed. PV1 and PV2 had initial BG lowering but eventual return to consistent hyperglycemia after 14 days post transplantation. PV3 demonstrated slightly better glucose control initially but eventually returned to consistent hyperglycemia after 30 days post transplantation. PV4 demonstrated superior glycemic control immediately after transplantation and remained for the duration of the 80-day experiment. After explantation, BG values returned to high levels. PV4 demonstrated the first success of long-term glucose control with a prevascularized device in the subcutaneous space without the need to terminate the experiment early due to wound healing concerns.

Rat C-peptide levels 50 days after transplant and after graft explant (Figure 4.8C) in the various groups are displayed. Mice PV3 and PV4 (PV1 and PV2 had to be sacrificed before blood collection was approved) showed different values, PV3 at 361 pM and PV4 at 631 pM. The higher rat C-peptide level in PV4 indicated that the graft was functioning and was similar to the KC group. In the animals tested before explantation, C-peptide levels dropped after device explantation at time of sacrifice. CTRL and DIA showed minimal amounts of C-peptide, most likely due to the cross-reactivity of the assay or hemolysis interference.[138]

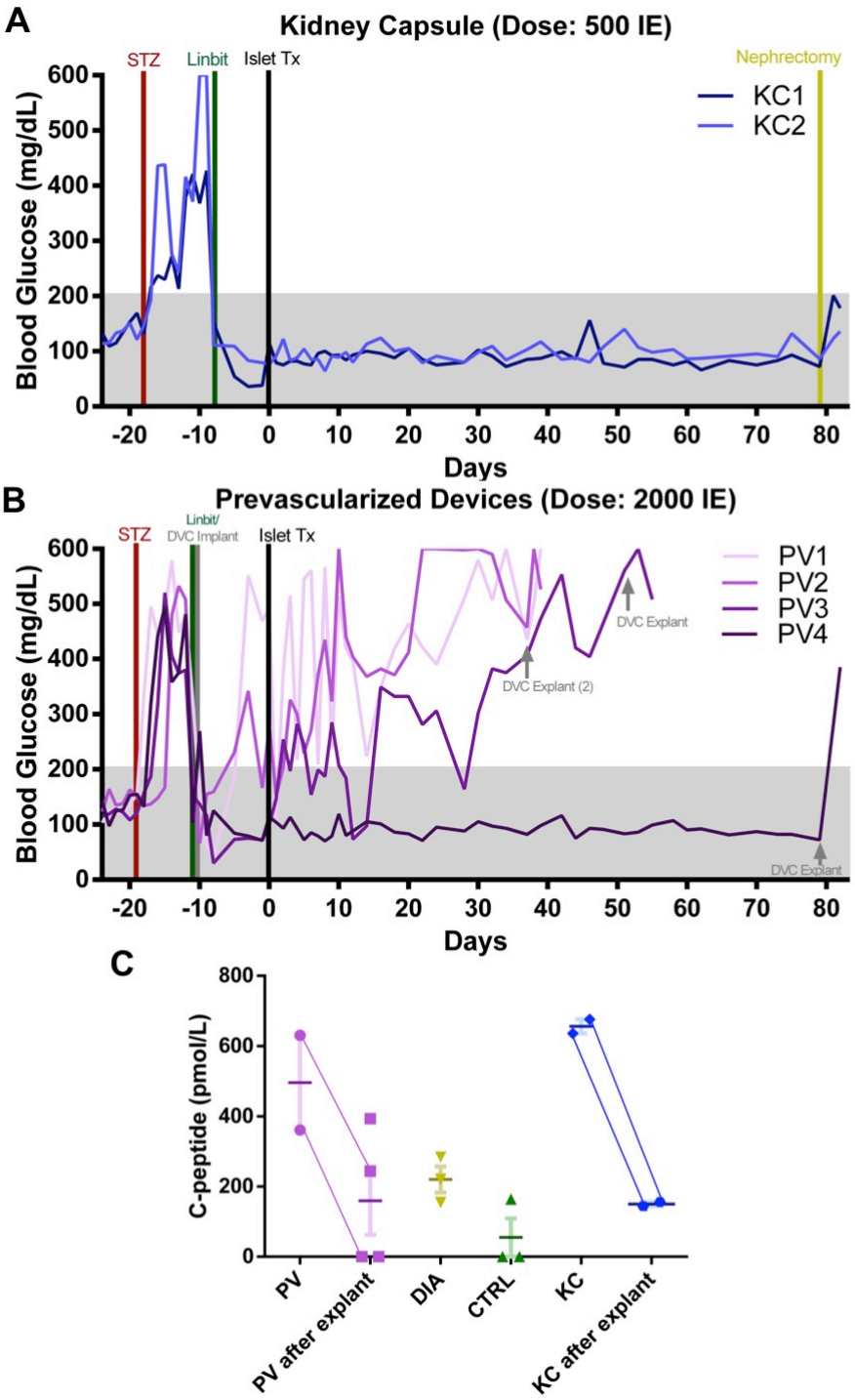

Figure 4.8: Blood glucose profiles and blood C-peptide measurements in experiment 5 groups. (A) Nonfasting blood glucose (NFBG) measurements of KC mice (blue) demonstrate euglycemia immediately after transplantation for the duration of the experiment. Nephrectomy did not induce return to hyperglycemia. (B) NFBG measurements of PV mice (purple) show engraftment failure in two mice (PV1, PV2), initial moderate function and gradual attrition in one mouse (PV3) and euglycemia in one mouse (PV4) for 80 days until device explant and return to hyperglycemia. (C) Rat C-peptide measurements in the blood of PV and KC mice before and after graft explantation as well as in diabetic (DIA) and nondiabetic (CTRL) controls. Lines connecting individual data points represent the change in C-peptide measurements from before to after explant. Data represent mean±SEM.

IPGTTs (Figure 4.9A) were performed on the different groups to determine the ability of the transplanted grafts to clear glucose effectively. IPGTTs were completed at 4 weeks post-transplantation as well as after graft explantation on the PV and KC groups. Average glucose clearance profiles (Figure 4.9B) and AUC calculations (Figure 4.9C) summarize the varied results. Similar to that seen in experiment 2, although grafts in PV1, PV2, and PV3 were demonstrating high NFBG levels, glucose clearance profiles (Figure 4.9A, top left) indicate there may be some function; however, this may be due to the native pancreas regenerating. After explant, similar profiles for PV1 and PV3 (Figure 4.9A, top right) suggest that the native pancreas was compensating. PV4 glucose clearance was much worse after explantation, as expected. For KC mice, the phenomenon of similar glucose clearance profiles before (Figure 4.9A, middle right) and after explant (Figure 4.9A, middle left) in KC2 was also seen but KC1 had a similar response as PV4 with impaired clearance after explant. CTRL (Figure 4.9A, bottom left) and DIA (Figure 4.9A, bottom right) showed expected glucose clearance profiles with fast and very slow rates, respectively. All results are summarized (Figure 4.9B) and AUC calculations displayed (Figure 4.9C).

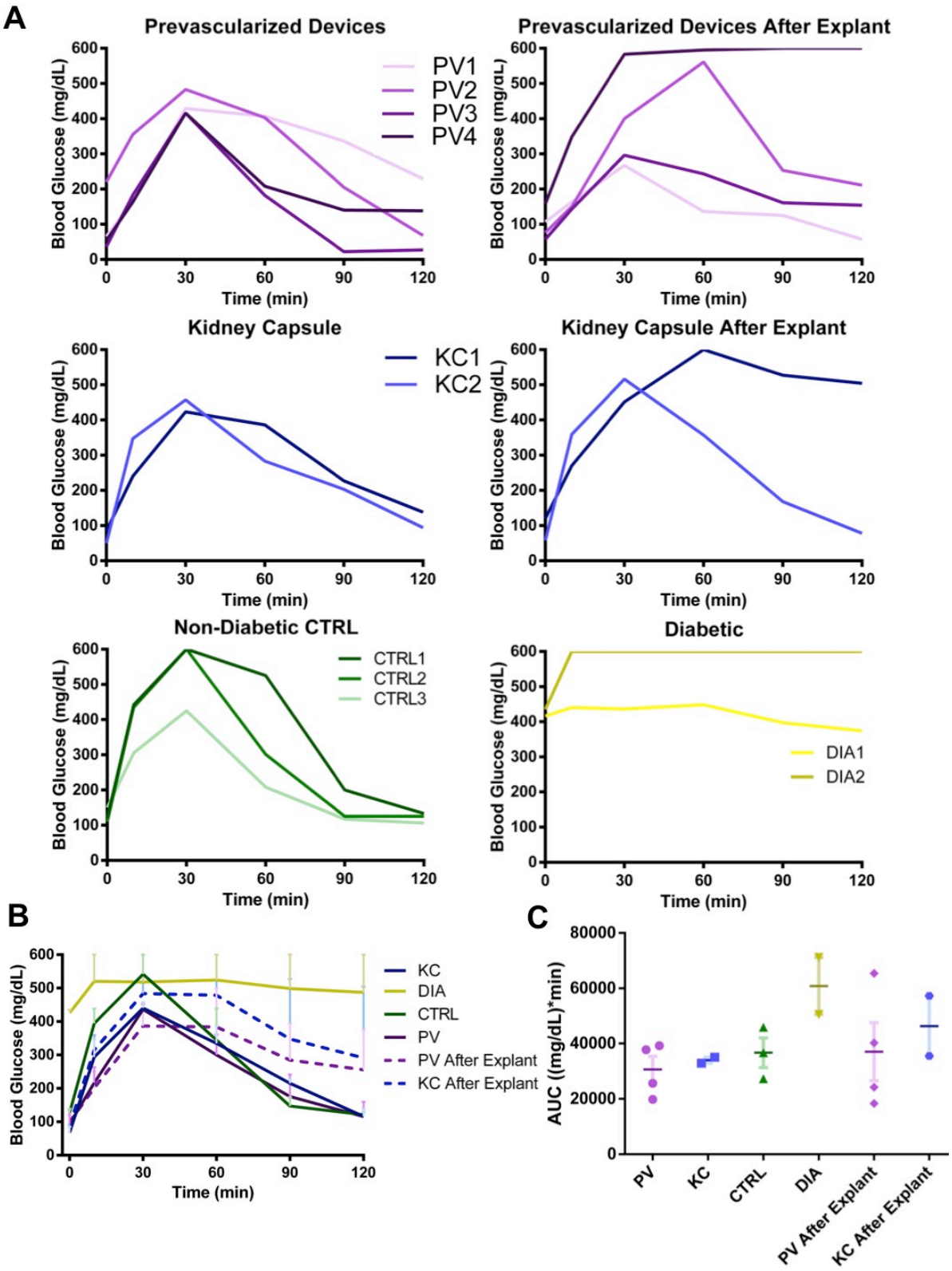

Figure 4.9: IPGTT results of fifth experiment.
(A) IPGTT 4 weeks after transplantation and two days after graft explant at a dose of 3 g glucose/kg body weight after 8 h fast results of individual mice within each transplant group: prevascularized (purple), kidney capsule (blue), non-diabetic control (green), and diabetic (yellow). (B) Average IPGTT of each group. (C) Area under the curve calculations for each group. Data represent means and error bars represent SEM.

Immunohistochemistry of islets within the pancreas as well as grafts was performed to determine the effectiveness of STZ injection as well as the extent of insulin production in the graft area, respectively (Figure 4.10). Islets within the naïve CTRL pancreas (Figure 4.10A) showed the characteristic structure of mouse islets, with a majority of insulin staining within the islet center and some glucagon staining around the islet edge.[139,140] In the DIA group pancreas (Figure 4.10B), the opposite was observed, with a majority of the islet stained positively for glucagon, and small amounts of insulin on the edges. For the KC mice pancreas (Figure 4.10C), a mixture of glucagon and insulin positive cells were observed indicating that the STZ may have had some effect, but did not completely destroy all β cells. All pancreas staining indicated a highly vascularized environment. In the KC grafts (Figure 4.10D) and functional PV grafts (Figure 4.10E), insulin staining was strong and robust with compact morphology. Glucagon staining was also apparent in the PV graft. In contrast, the nonfunctional PV2 graft (Figure 4.10F) showed little staining for insulin or glucagon.

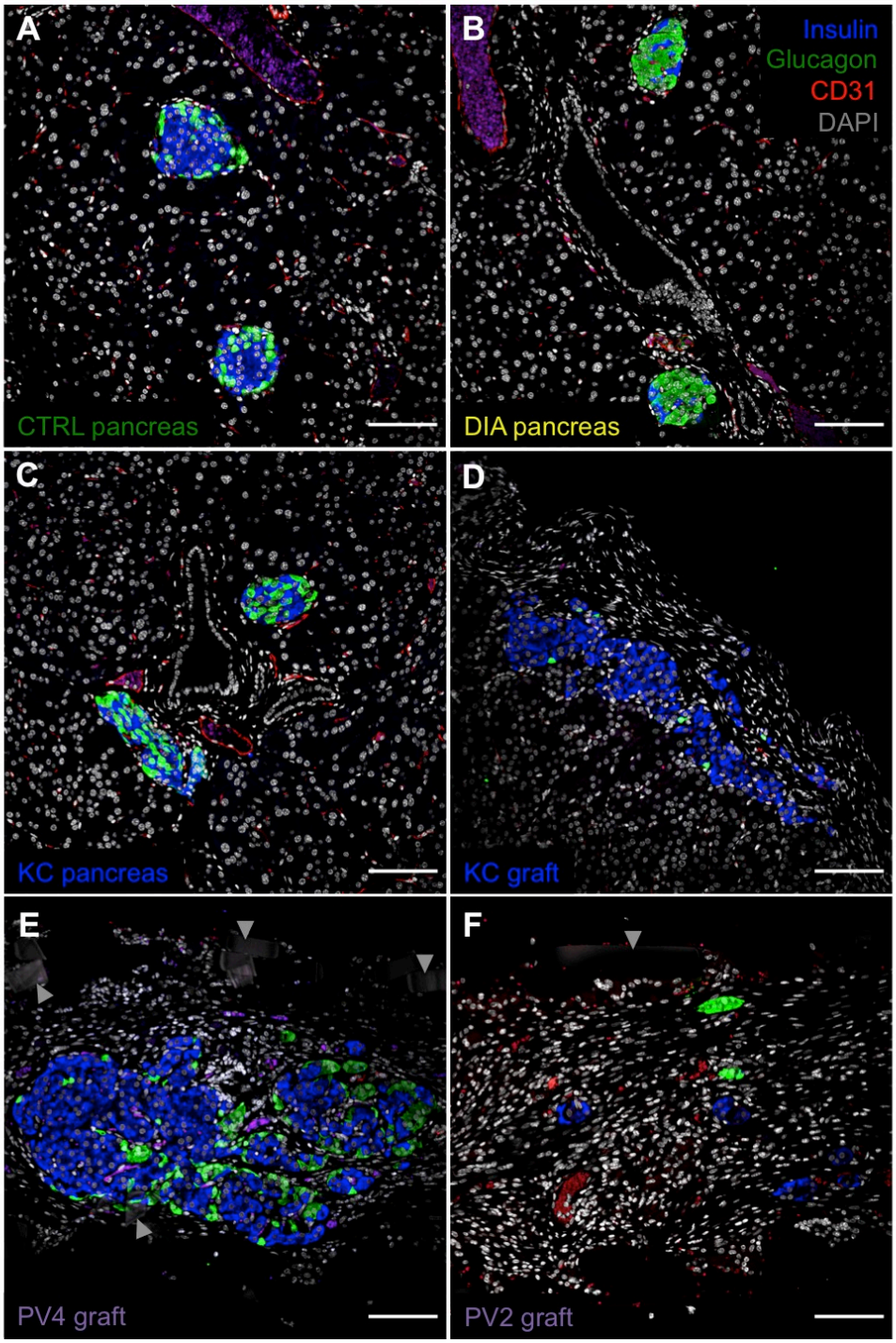

Figure 4.10: Islet immunohistochemistry of pancreas and graft tissue from experiment 5 groups. (A) Islets from a control mouse show a majority of insulin (blue) staining in the center with scattered glucagon (green) staining around the edges of the islet and supporting blood vessels identified by CD31 (red). (B) Diabetic mice via STZ show a majority of glucagon staining in the center with minimal insulin staining. (C) KC mice seem to show a mixture of insulin and glucagon staining, which may indicate why glucose values did not return to hyperglycemic levels after graft explant. Vascular density appears to be high within the pancreas samples. (D) SD rat islets in the graft of the KC show insulin staining. (E) Islets within the working PV4 graft show strong insulin staining. (F) Insulin staining within the nonfunctional PV2 graft shows is minimal. Vascular density appears to be decreased in the grafts when compared to the native pancreas. Counterstaining with DAPI (grey) shows cell nuclei. Grey arrows indicate the braiding material from the device. Scale bars=100 μm.

4.3.6 Device modeling

To gain a better understanding of the *in vivo* results, we set-up a series of simple, analytical models to estimate the effects of perfusion and packing fraction (islet density) on the device's ability to maintain normoglycemia in mice. This work was completed in collaboration with Dr. Anna Grosberg in the UCI Department of Biomedical Engineering.

Parameter Estimation and Validation

Diffusion coefficients, consumption rates, and concentrations mainly from Buchwald *et al*,[141] unless otherwise cited, were implemented in this model (Table 4.3).

Table 4.3: Parameter values for analytical model.

Parameter	Value	Description
R_{oxygen}	-3.4×10^{-20} mol/($\mu m^3 \cdot s$)	Oxygen consumption
$R_{glucose,max}$	-2.8×10^{-20} mol/($\mu m^3 \cdot s$)	Glucose consumption
$R_{insulin,max}$	3×10^{-23} mol/($\mu m^3 \cdot s$)	Insulin production (second phase)
$D_{oxygen,water}$	3000 $\mu m^2/s$	Diffusion coefficient of oxygen through water
$D_{oxygen,tissue}$	2000 $\mu m^2/s$	Diffusion coefficient of oxygen through tissue
$D_{oxygen,PDMS}$	3250 $\mu m^2/s$	Diffusion coefficient of oxygen through PDMS[142]
$D_{glucose,water}$	900 $\mu m^2/s$	Diffusion coefficient of glucose through water
$D_{glucose,tissue}$	300 $\mu m^2/s$	Diffusion coefficient of glucose through tissue
$D_{glucose,PDMS}$	0 $\mu m^2/s$	Diffusion coefficient of glucose through PDMS
$C_{oxygen,media}$	2×10^{-20} mol/μm^3	Concentration of oxygen at the bottom of 1 mm media[143]
$C_{glucose,media}$	1.118×10^{-19} mol/μm^3	Concentration of glucose in media (CMRL-1066, Sigma-Aldrich)
$C_{oxygen,blood}$	9.3×10^{-18} mol/μm^3	Concentration of oxygen in arterial blood[144]

We validated the parameter choices for oxygen by estimating the size of a spherical islet with no necrotic core *in vitro*. Starting from the binary continuity equation in the spherical coordinate system, we derived the maximum spherical radius where no necrotic core exists. The maximum spherical radius is calculated by:

$$r_{max} = \sqrt{\frac{-6C_{oxygen,media}D_{oxygen,tissue}}{x_{pf}R_{oxygen}}} \qquad \text{Equation 4:1}$$

where $C_{oxygen,media}$, $D_{oxygen,tissue}$, and R_{oxygen} can be found in Table 4.3, and x_{pf} is the cell packing fraction. In Figure 4.11, the blue line represents the maximum sphere diameter as packing fraction increases. At a packing fraction of 1, the blue line meets a maximum survivable islet diameter of 168 μm, approaching a value of 150 μm (black line, Figure 4.11) similar to that found in other publications,[143] validating the parameter set. Applying the same parameters from the spherical case to the cylindrical case with no perfusion and *in vitro* boundary conditions, the maximum cylindrical radius with no necrotic core is given by:

$$r_{max} = \sqrt{\frac{-4C_{oxygen,media}D_{oxygen,tissue}}{x_{pf}R_{oxygen}}} \qquad \text{Equation 4:2}$$

We graphed the maximum radius as a function of cell packing fraction (Figure 4.11, red line). Fabricated devices contain PEEK braid-enforced channels, with a radius (r_{tube}) of 184 μm (green line, Figure 4.11). With this cylindrical radius, only a cell packing fraction of 14% or less *in vitro* will preclude a necrotic core, demonstrating not only the potential but also the need for perfusion.

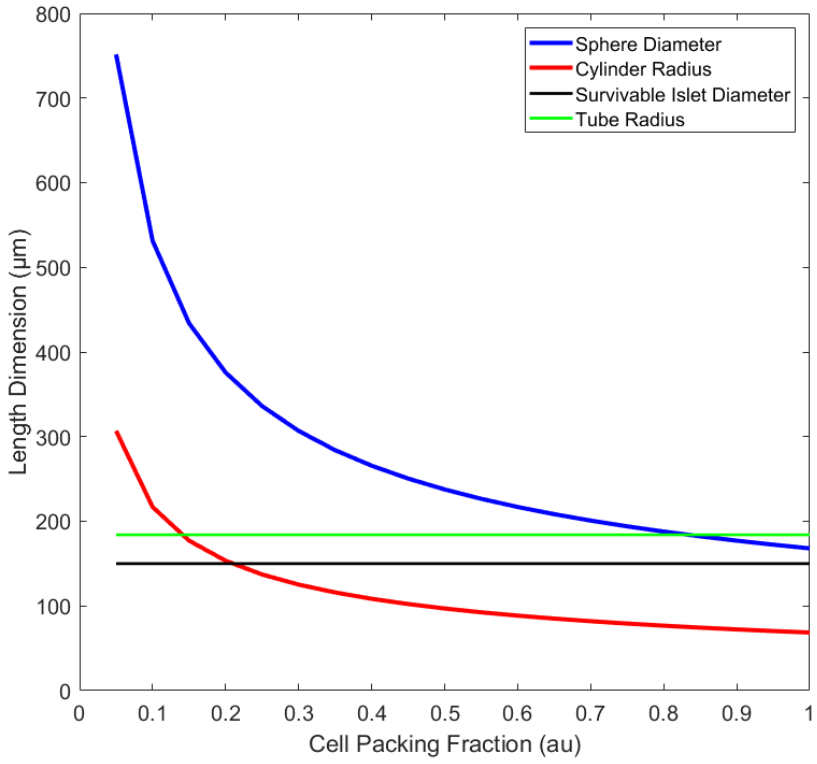

Figure 4.11: Maximum length estimation dependent on cell packing fraction *in vitro*.
With *in vitro* boundary conditions, the blue and red lines describe the maximum sphere diameter and cylindrical tube radius, respectively. The black line represents the survivable islet diameter at 150 μm.[143] The green line represents the PEEK braid radius at 184 μm.

Perfusion: Oxygen

Different from many models of islet insulin secretion that focus on *in vitro* static culture or perfusion chambers, we aimed to investigate the role of *in vivo* perfusion within the sheet device on islet insulin production. For oxygen in the presence of hemoglobin, the transport via perfusion by blood vessels will dominate over transport by diffusion. We observed in experimental data that in some cases, cells can survive and produce insulin while completely filling the braid-reinforced channel tubes (Figure 4.6D, 4.10E). As diffusion only transport will result in a large number of dead islet cells in the core of the islet cylinder, which was not observed experimentally, we focus on the perfusion transport of oxygen. Given this experimental data, we estimated the amount of perfusion needed by determining the minimum contact area of blood vessels within the windows of the device to maintain full survivability. The minimum contact area is given by:

$$A_{min} = -\frac{4D_{oxygen,tissue}\pi L r_{tube}^2 R_{oxygen} x_{pf}}{(h_{mass} r_{tube}^2 R_{oxygen} x_{pf} + 4C_{oxygen,blood} D_{oxygen,tissue})}$$ Equation 4:3

where $D_{oxygen,tissue}$, R_{oxygen}, and $C_{oxygen,blood}$ can be found in Table 4.3, r_{tube}=184 μm, x_{pf} is the packing fraction, h_{mass} is the convective mass transport coefficient, and L is the length of the device segment. Because blood contains red blood cells with hemoglobin, the carrying capacity for oxygen and therefore concentration of oxygen is much higher than conventional *in vitro* systems. Devices were reduced down to repeating segments of L=1000 μm (red dashed box, Figure 4.12) and we assumed symmetry across the device.

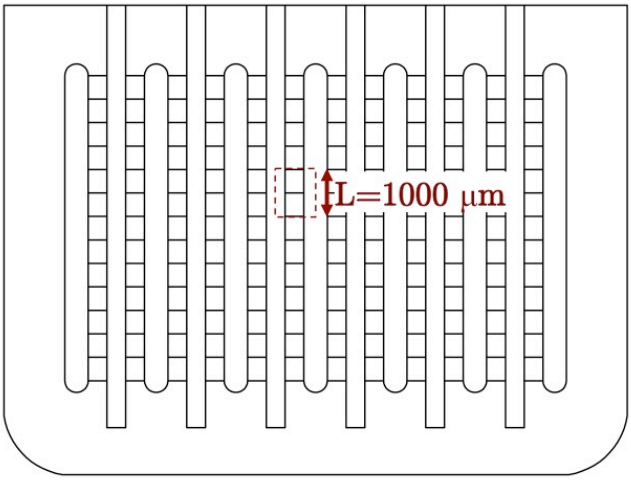

Figure 4.12: Schematic of the device and outline of a repeating segment.

The mass transport coefficient is defined as:

$$h_{mass} = \frac{D_{oxygen,water} Sh}{L_c}$$ Equation 4:4

where $D_{oxygen,water}$ can be found in Table 4.3, Sh=3 is the Sherwood number estimated from Huang and Tarbell,[145] and L_c=10 μm is the characteristic length defined to be the diameter of the capillaries inside the window. A_{min} can be divided by the cross-sectional area of the device windows, the only space in which blood vessels can directly access the device channels, to get a perfusion fraction. For a packing fraction x_{pf} of 1, a minimal perfusion fraction of 1.76% is needed to maintain survivability of all of the islets through the whole of the tube radius in the device channels, with

respect to oxygen. The finding that a low perfusion fraction at a packing fraction x_{pf} of 1 is needed demonstrates the powerful effect of perfusion with hemoglobin-carrying red blood cells.

Perfusion: Glucose

There are no glucose carriers in the blood, so perfusion is only beneficial in the sense of providing convective transport. The device imposes an extra barrier to glucose transport, which was described with resistances. The equation for resistance of features with symmetry in Cartesian coordinates is:[146]

$$R_{feature} = \frac{L_{feature}}{D_{AB}A_{feature}} \qquad \text{Equation 4:5}$$

where R is the resistance of a device feature, L is the length of that feature, D_{AB} is the diffusion coefficient of a molecule of interest (e.g. glucose) through the material of that feature (e.g. PDMS, tissue), and A is the cross-sectional area of that feature. Dimensions that were used for calculating resistances can be derived from device drawings in Appendix Figure A.6. Set-up of the resistances from the cells within the braid-enforced device channels to outside of the device is depicted in Figure 4.13. A resistance term $R_{convection}$ is also added and given by:

$$R_{convection} = \frac{1}{h_{mass}A_{contact}} \qquad \text{Equation 4:6}$$

The total resistance, R_T encompasses all of the resistances depicted in Figure 4.13.

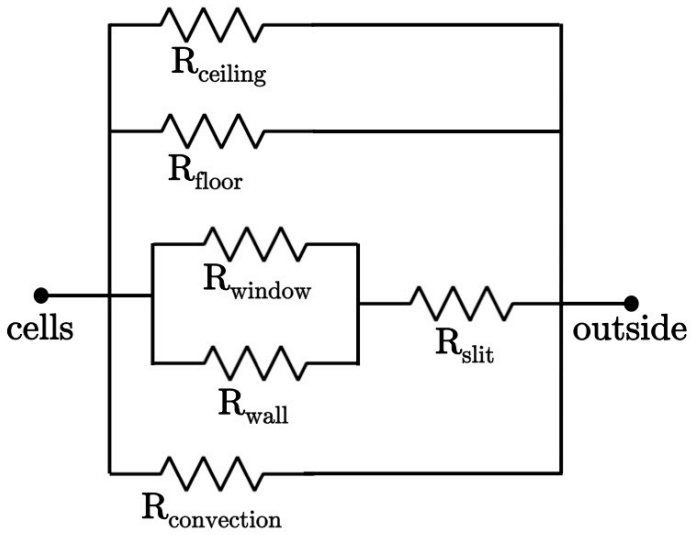

Figure 4.13: Resistance map for R_T with convection.

In an actual system, the rate of glucose consumption by islets depends on the glucose concentration,[147] which is not realistic to solve analytically. Thus, we estimate the effect of perfusion by assuming an average constant glucose consumption rate. It is important to emphasize that this is a rough estimate and should be interpreted as such. As a result, the output of this simple model is the average glucose consumption given varying blood glucose concentration $C_{glucose,blood}$ at various perfusion fractions and packing fractions with the condition that the consumption rate cannot exceed a maximum $R_{glucose,max}$ per volume of cells. The available glucose consumption rate is:

$$R_{glucose,available} = \frac{-C_{glucose,blood}}{x_{pf}(\pi L R_T r_{tube}^2 R_{glucose} + \frac{1}{4D_{glucose,tissue}})} \quad \text{Equation 4:7}$$

The glucose consumption rate with a maximum cap is implemented by:

$$R_{glucose,actual} = \begin{cases} R_{glucose,available} \; if \; |R_{glucose,available}| < |R_{glucose,max}| \\ R_{glucose,max} \; if \; |R_{glucose,available}| \geq |R_{glucose,max}| \end{cases} \quad \text{Equation 4:8}$$

and the total glucose consumption rate for the whole device is:

$$Q_{glucose} = x_{pf} R_{glucose,actual} \pi r_{tube}^2 Ln_{repeatingunits} \quad \text{Equation 4:9}$$

Figure 4.14 displays the total glucose consumption rate by the device at varying physiological blood glucose levels (3-30 mM or 54-540 mg/dL, which corresponds to $0.3x10^{-17}$-$3x10^{-17}$ mol/μm^3). When perfusion levels and packing fraction are highest (black line, Figure 4.14), the glucose consumption rate is at a maximum level for all blood glucose concentrations. When perfusion levels slightly decrease (green and purple line, Figure 4.14), glucose consumption rates reach a maximum even at low glucose concentrations. When perfusion levels are severely limited (yellow line, Figure 4.14), higher blood glucose concentrations are needed to reach the maximum glucose consumption rate. At medium perfusion and low packing fraction (light blue line, Figure 4.14), glucose consumption is at a smaller maximum at all blood glucose concentrations due to the smaller volume of cells. At low perfusion levels and low packing fractions, (orange and dark blue line, Figure 4.14) total glucose consumption rates are limited at low-mid blood glucose concentrations. It is worth noting that

packing fractions x_{pf} less than one are likely in the *in vivo* case as islets take on a spherical shape. Perfectly fitting spheres into a cylindrical tube is less likely in the experimental case.

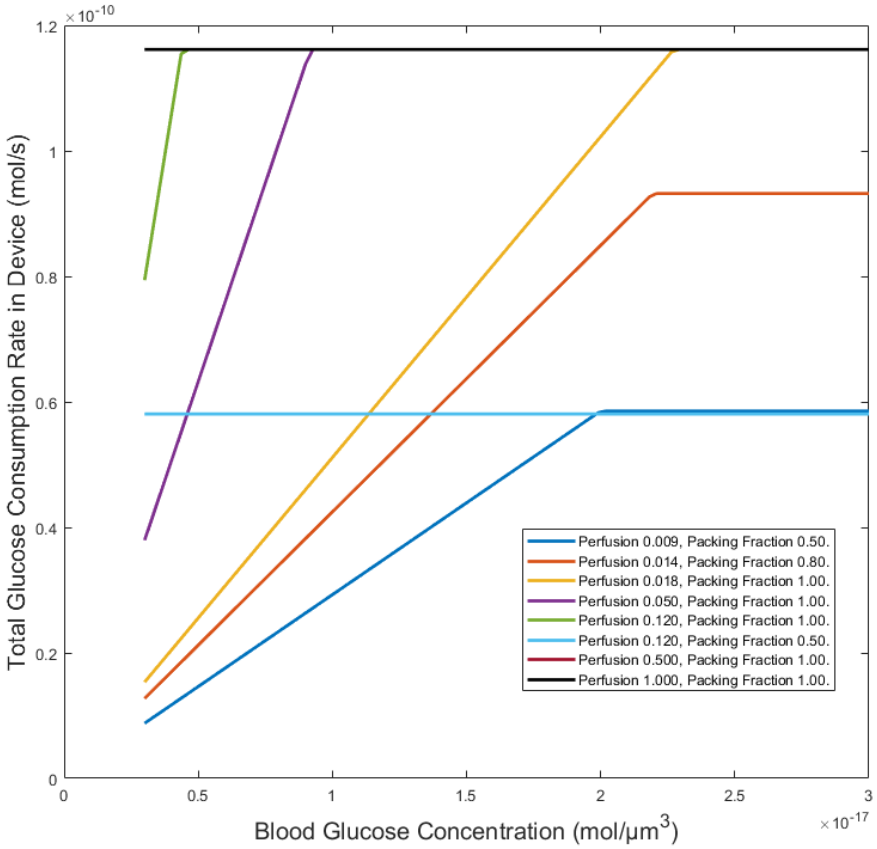

Figure 4.14: Glucose consumption rate in the device as a function of glucose concentration. At varying perfusion and packing fractions, glucose consumption rates increase as glucose concentration increases and eventually reaches a maximum.

The amount of insulin that the islets will produce will depend on the glucose concentration that is available to them. The islet tube surface glucose concentration is given by:

$$C_{glucose,surface} = C_{glucose,blood} + \pi L R_T r_{tube}^2 R_{glucose,actual} x_{pf} \qquad \text{Equation 4:10}$$

Figure 4.15 displays the glucose concentration at the surface of the braid (i.e. islet tube) as a function of blood glucose concentrations. When perfusion and packing fraction are ideal (equal to 1) (black line, Figure 4.15), the glucose concentration at the tube surface is close to that in the blood. When perfusion is dropped to half (0.5) (red line, Figure 4.15), the trend is the same. More drastically, when the perfusion is dropped to 12% (0.12) (green line, Figure 4.15) or even more so to 5% (0.05) (purple

line, Figure 4.15), glucose concentrations at the tube surface start to diminish relative to the blood glucose concentration. If the islets are not 'seeing' the accurate blood glucose concentrations and instead are exposed to a lesser glucose concentration, their insulin secretion will also be limited. When perfusion is decreased even further (less than 1.8%) and packing fraction is lowered (dark blue, orange, and yellow lines, Figure 4.15), the difference in glucose concentration between that at the islet tube surface and that in the blood is drastically larger. When packing fractions are lowered (light blue, dark blue, and orange lines, Figure 4.15), the glucose concentration at thee tube surface is slightly higher because less cells are consuming glucose. These results indicate the need for high perfusion within the device.

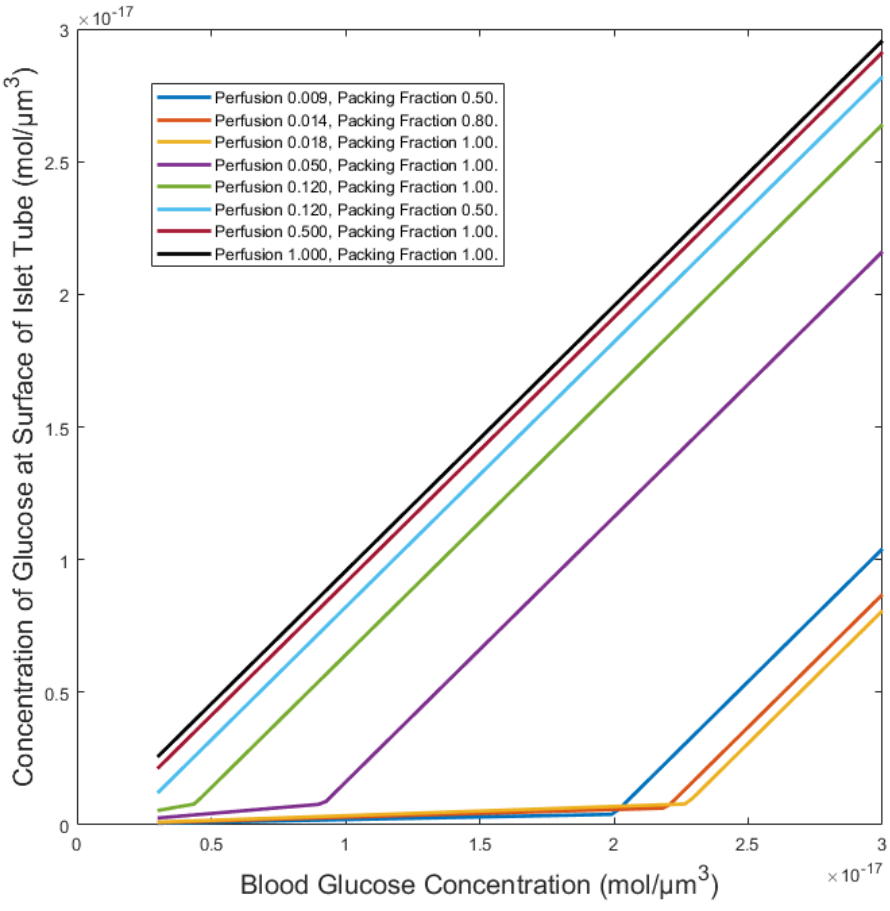

Figure 4.15: Tube surface glucose concentration as a function of blood glucose concentration. At various perfusion levels and packing fractions, the concentration of glucose at the surface of the islets within the braids changes with blood glucose concentration. In a mid-highly packed and mid-highly perfused case (black, red, light blue, and green lines), these two concentrations are nearly the same (slope=1). When perfusion is slightly limited (purple line) or severely limited (dark blue, orange, and yellow lines), the concentrations become dramatically different.

Insulin Production

To estimate the amount of insulin the device can produce given the glucose concentration at the islet tube surface, we determined glucose concentration within the tube is given by:

$$C_{glucose}(r) = \frac{x_{pf} R_{glucose,available}}{4D_{glucose,tissue}}(r_{tube}^2 - r^2) + C_{glucose,surface} \qquad \text{Equation 4:11}$$

Using the Hill function as described by Buchwald,[147] the rate of insulin production is given by:

$$R_{insulin}(r) = R_{insulin,max}\frac{(C_{glucose}(r))^{n_i}}{(C_{glucose}(r))^{n_i} + C_{HF,insulin}^{n_i}} \qquad \text{Equation 4:12}$$

where $C_{HF,insulin}^{n_i}$=7x10^{-18} mol/μm^3 and n^i=2.5 and R$_{insulin,max}$=3x10^{-23} mol/(μm^3 • s). The rate of insulin production of the device is found by integrating over the tube volume and multiplying by the number of repeating units:

$$Q_{insulin} = (L\int_0^{r_{tube}} 2\pi r\, x_{pf} R_{insulin}\, dr) n_{repeating\ units} \qquad \text{Equation 4:13}$$

Total insulin production is found by multiplying the insulin production rate by the number of repeating segments in the whole device and is shown in Figure 4.16. Similar to that described for Figure 4.15, the actual insulin produced as a result of blood glucose concentration is very much dependent on the amount of perfusion and the packing fraction of the islets within the tube (Figure 4.16). With low perfusion rates, even at the highest physiological glucose concentration, maximum insulin production is not reached.

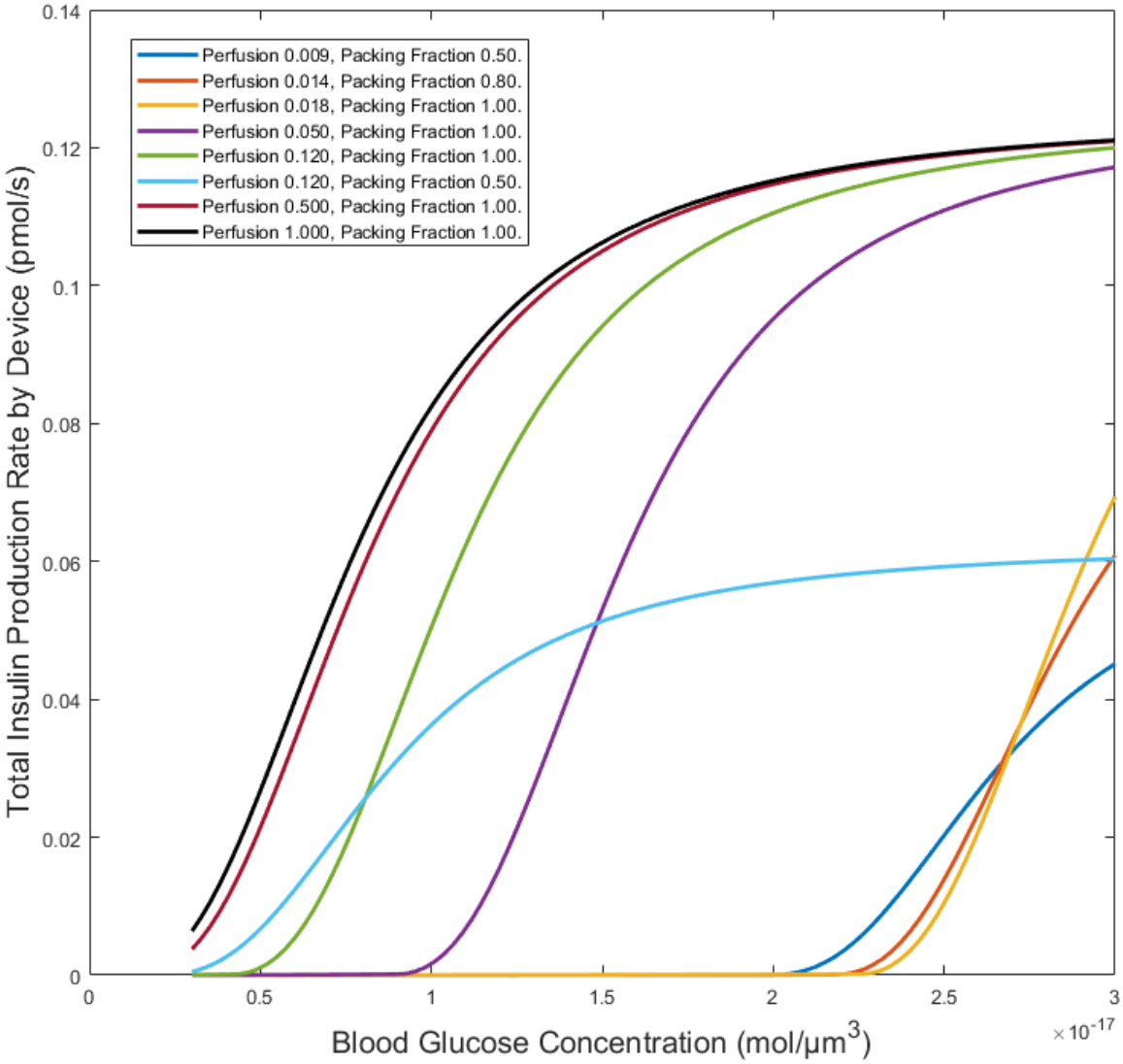

Figure 4.16: Total insulin production by the device per time over varying glucose concentrations. Using a Hill model function for insulin secretion and integrating over the tube volume, the total insulin production at varying levels of perfusion and packing fractions is calculated. With high perfusion and packing fraction (black and red lines) at low physiological ranges of glucose concentration, insulin secretion is initiated. At medium perfusion levels (green, light blue, and purple lines), insulin production is slightly shifted and initiation occurs at middle physiological ranges. At medium perfusion level and diminished packing fraction (light blue line), insulin production rate reaches a smaller maximum due to the reduced number of cells. For low perfusion levels (dark blue, orange, and yellow lines), insulin production only begins at mid-high glucose concentrations.

4.4 Discussion

In athymic nude mice with STZ-induced diabetes, SD rat islets were transplanted into various prototypes of skin integrated PDMS sheet devices via a two-phase prevascularization approach. Devices were initially large in size at 30 mm x 20 mm, with a prevascularization period of 8 days before transplantation. An islet dose of

2825 IE resulted in moderate control of blood glucose in two mice, one for 12 days and one for 22 days. Incomplete healing prompted premature device excision. To improve upon these preliminary results, devices were reduced by half in size to 18.5 mm x 10 mm with a smaller islet dose of 1100 IE and a longer prevascularization period of 14 days. No mice reached euglycemia and decreased survival was observed.

Islet loading into the devices was refined to provide a gentler method of *in situ* transplantation. Two devices with a decreased size of 14.5 mm x 10 mm were implanted with a dose of 800 IE each (1600 IE total) after a longer prevascularization period of 28 days. One mouse maintained normoglycemia for 10 days. Again, inadequate healing resulted in graft failure. The final device design at a size of 13.3 mm x 13.3 mm with rounded edges was implemented with two islet doses of 1200 and 800 IE and a prevascularization period of 28 days. Unfortunately, none of the mice achieved euglycemia; however, device healing was much improved and there were no significant complications as seen in prior studies. IPGTTs and IHC insulin staining indicated that the grafts might have been partially functional, although not to the extent to result in normoglycemia.

The final study utilized fibrin and its proangiogenic properties[148] to encourage neovascularization directly to the device channels to further support islet engraftment. Various groups have implemented fibrin within scaffolds for improving normoglycemia rates in the subcutaneous space[40] and the epididymal fat pad.[149] The same device (13.3 mm x 13.3 mm) was used with a prevascularization period of 12 days at a dose of 2000 IE. One out of four (25%) mice transplanted achieved euglycemia for 80 days without healing complications. Insulin staining of the functional graft indicated high numbers of insulin-producing cells in a compact, rounded morphology, which was different from the more spread-out insulin-positive cells in the previous study.

With varied results of *in vivo* studies, we turned to simple, analytical modeling of the device to investigate why such differences may have occurred. We found that the amount of perfusion has a severe impact on how much glucose reaches the cells within the device channels. The decrease in glucose concentration in less perfused

states in turn decreases the amount of insulin that is produced. In previous chapters, we have found vascular area percentages within the slit space to range from 2-15%. Whether this perfusion fraction can be generalized from what is observed in the slit space to the window space has yet to be investigated, but if we assume that perfusion is similar, it could account for the varying degrees of achieving euglycemia with prevascularized sheet devices. Determining a method to more reliably promote a certain threshold of vascularization, with a tailored fibrin incorporation protocol for example, to the device channels could improve euglycemia rates.

Still, in the various prototypes of prevascularized devices tested, the kidney capsule transplant site proved to be more efficacious requiring smaller islet doses and achieving higher rates of euglycemia. This result was to be expected as the kidney capsule has a long track record of success in murine islet transplantation.[150] In humans, however, the kidney capsule suffers from relatively poor blood supply, limited space for a clinically-relevant transplant volume, an invasive surgical procedure, and potential damage from diabetic nephropathy.[151,152] The advantages of a subcutaneous device being easy to image,[153,154] minimally invasive, and easy to retrieve may offset the fact that it is less efficacious. Retrievability may be especially important for future implementation of stem cell technologies[155] in which complications such as teratoma formation and unchecked hormone release could be mitigated with graft removal. The subcutaneous site also affords compatibility with local immunomodulation approaches via cotransplantation of other cell types[156,157] or pharmaceuticals[119,120] to promote graft survival in immunocompetent animals. Further improvements can be made to make the skin integrated PDMS sheet approach to islet transplantation more advantageous.

4.5 Conclusion

Overcoming the limitations of the intraportal islet transplantation with alternative transplantation sites will be critical in implementing cell therapy to a wider T1D patient population. Housing of islets within an engineered PDMS device that can be easily altered coupled with a distinct islet loading method provides mechanical stability, intradevice prevascularization, and precise islet spatial

distribution. Further improvements of the device design, material biocompatibility, prevascularization period, islet dose, and *in situ* islet transplantation will be necessary to achieve greater success of the subcutaneous two-phase approach in the future. Additional numbers of animals in transplant groups will be necessary in verifying repeatable results. Coupling these improvements with local immunomodulation techniques and other islet sources such as stem cell derived insulin-producing cells could provide a whole solution for subcutaneous islet transplantation in humans.

Chapter 5: Summary and Future Directions

5.1 Summary

Islet encapsulation technologies have long been plagued by hypoxia due to lack of vascularization. It was hypothesized that the unique slit architecture and single file configuration of islets would improve device vascularization, mass transport kinetics, and subsequently islet transplantation into the subcutaneous space. PDMS devices fabricated from 3D printed molds were assessed for vascularization, islet viability, oxygen availability, and diabetes reversal.

There are many explanations for why a higher rate of euglycemia was not achieved. (1) The exact optimal timing for islet transplantation has yet to be determined and will vary based on the method employed. Oxygen dynamics measurements indicate that earlier implantation may be more advantageous; however, this is different from longer prevascularization periods of 28 days employed by other approaches.[40,158] (2) Although vascularization was investigated both in thin slit sheets (0.5 mm thickness) and in fully fabricated devices (1 mm thickness); the immune response to the material was only briefly explored. Preliminary results indicate a strong foreign body response to the PDMS material fabricated from 3D printed molds. An abundance of macrophages were observed in the slit space, with only a minority of them stained positive for CD206, the prohealing M2 macrophage marker. (3) The optimal islet dose has yet to be determined. In this dissertation, doses ranged from 800-2825 IE with varying results. In the subcutaneous space of mouse models, other groups have been successful with as low as 400 mouse islets[159] up to 3000 rat islets[160] and 5000 porcine islets.[161] (4) Device size and islet density within devices, largely determined by islet dose, will also need to be finely tuned to ensure optimal islet viability and function once transplanted.

In the interest of being clinically relevant, the macroencapsulation device scalability remains a major challenge in the translation of these technologies from small animals to humans.[101,162] The dose required for subcutaneous islet transplantation in humans is still unknown, but estimates suggest 5000 IE/kg to 10000 IE/kg could be required based off current clinical portal vein islet

transplantation requirements.[163,164] At the 5000 IE/kg dose, preliminary calculations call for 5 sheets stacked (5 mm thickness total) with dimensions of 6.7 cm x 3.2 cm for a 60 kg patient, which is reasonable for a subcutaneous implant, although other configurations are possible. With the improvements explored by this dissertation, islet transplantation may be more accessible as a treatment for type 1 diabetes.

5.2 Future Directions

In the future, the two-phase approach with subcutaneously integrated devices could be refined to help increase the chances of success. Careful investigation of the optimal islet dose, prevascularization period, device dimensions, and device material biocompatibility will be essential to improving functionality. Alternatively, other materials could be used with similar geometries and loading methods as described in this dissertation to achieve euglycemia in diabetic animals in the subcutaneous space. One composition of interest includes bijel (bicontinuous interfacially jammed emulsion gel)-templated materials. In collaboration with Dr. Ali Mohraz's group in the UCI Department of Chemical Engineering, we have previously found that the unique interpenetrating network of pores with smooth surfaces throughout bijel-templated materials have vascularizing and tissue-integrating properties.[165] Slit sheet designs comprised of bijel-templated materials of various chemical compositions could be implanted into the subcutaneous space for improved mitigation of the foreign body response while enhancing vascularization. Coupled with the developed *in situ* islet loading, bijel slit sheets could drastically improve the chances for euglycemia after islet transplantation into the subcutaneous space.

Appendix

SolidWorks drawings

The devices used for *in vitro* and *in vivo* were fabricated by molding from 3D printed molds from an Asiga stereolithographic printer. Shown here are the SolidWorks drawings used to print the molds for the various device designs and experiments. PDMS pieces molded from the devices do not take the exact measurements that were designed in the CAD (computer-aided design) drawing due to slight changes induced by both the printing and molding process but generally fall within 20% of the original drawing measurement.

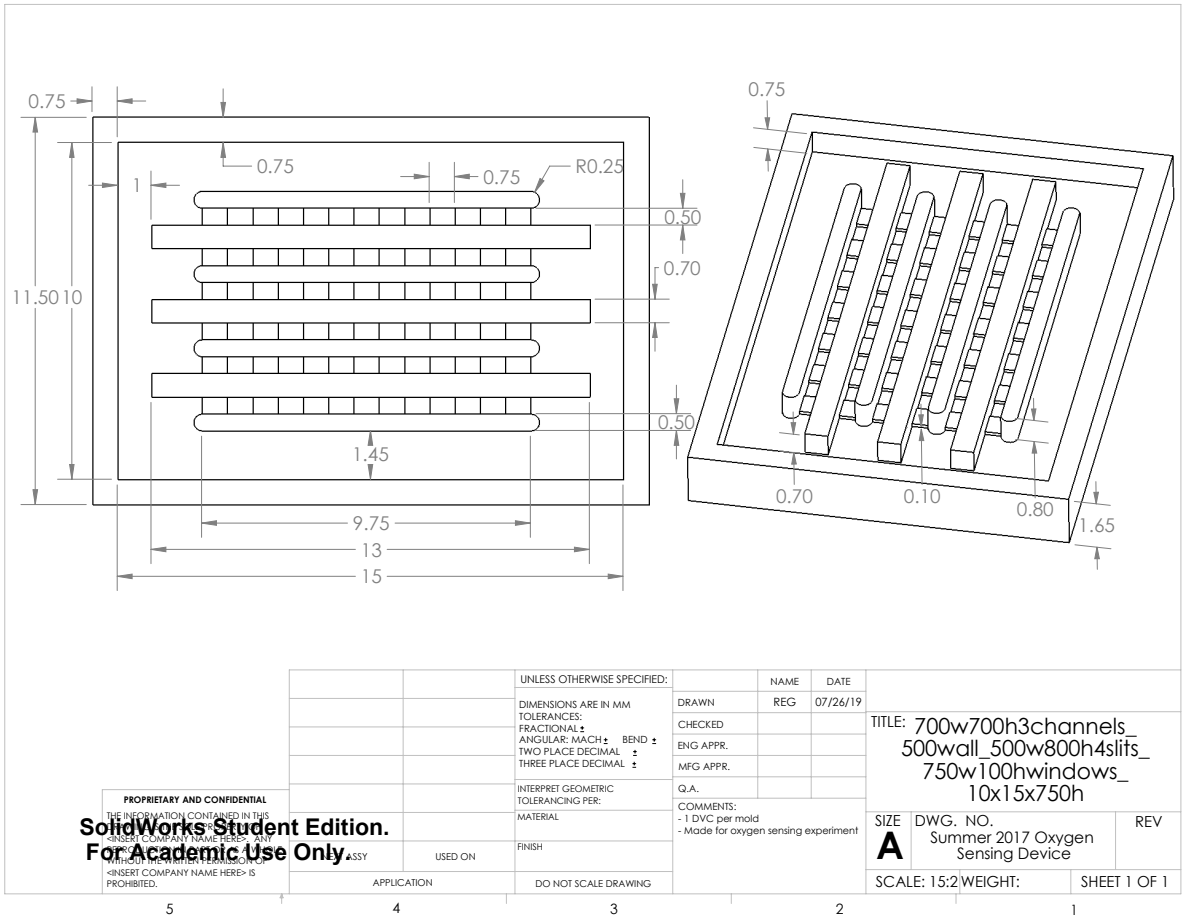

Figure A.1: Device mold design for *in vivo* oxygen sensing study.

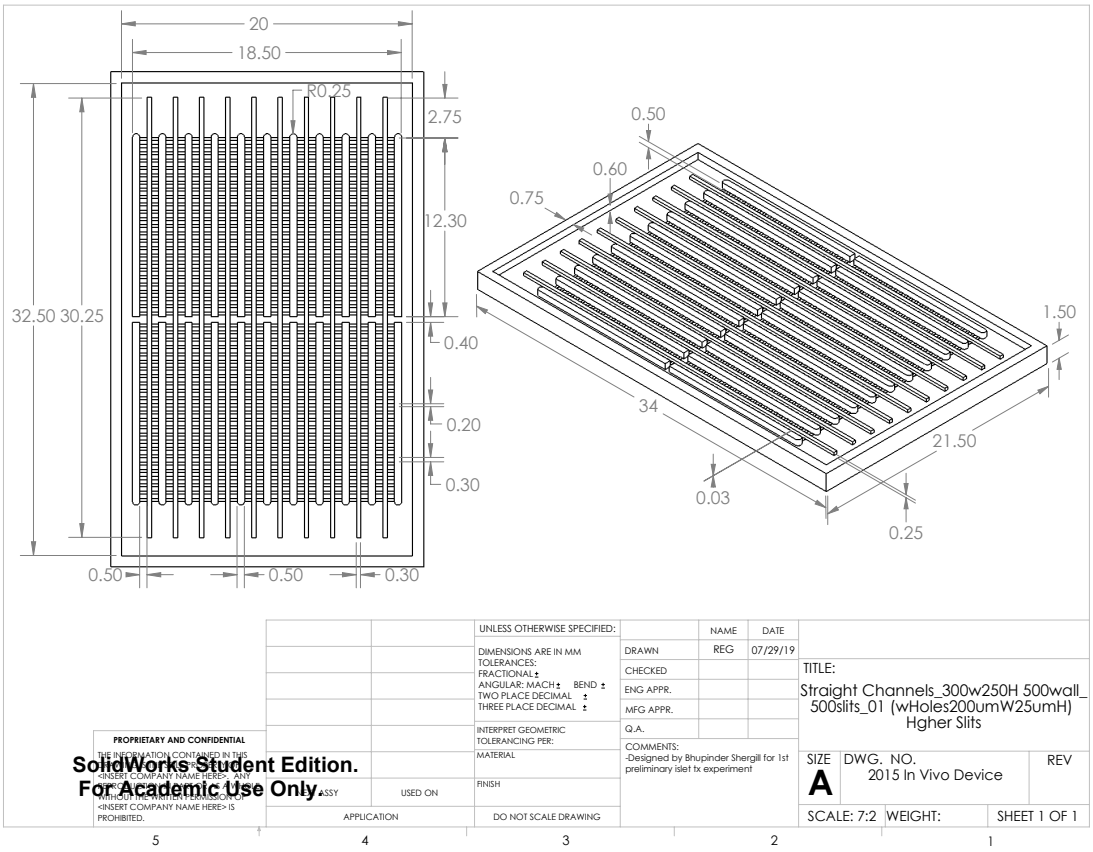

Figure A.2: Device mold design for islet transplantation experiment 1.

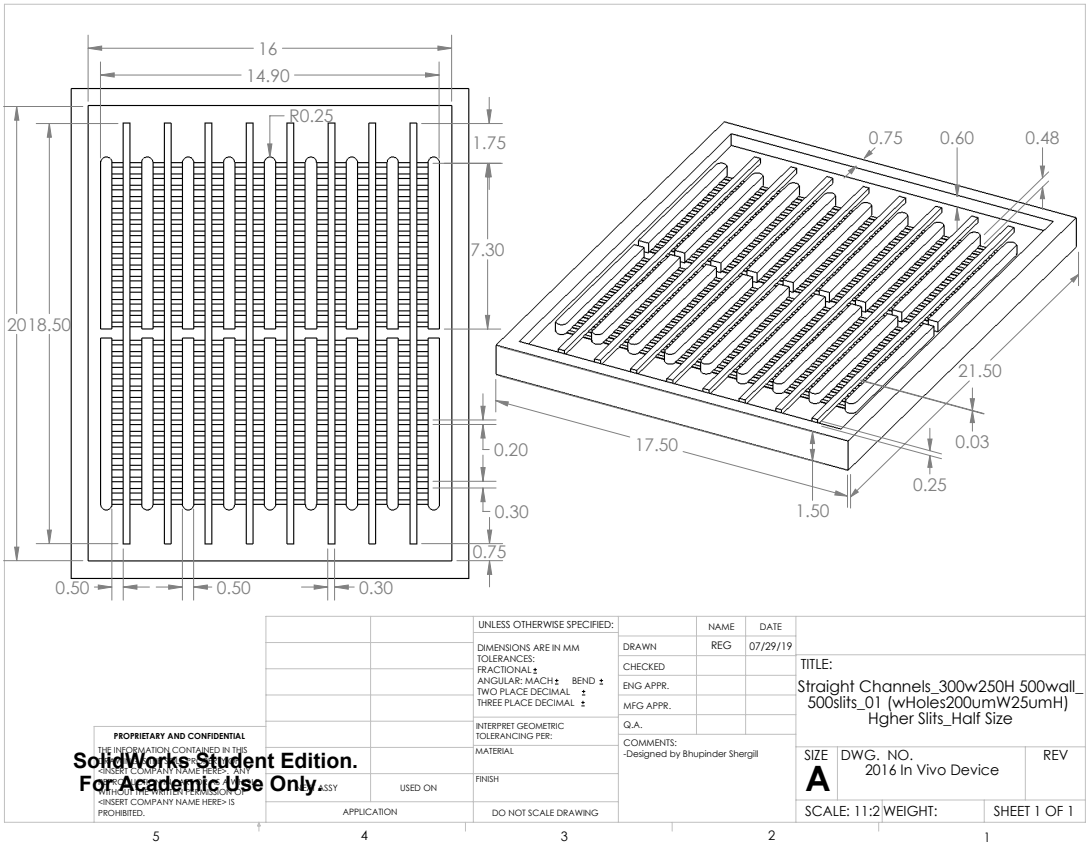

Figure A.3: Device mold design for islet transplant experiment 2.

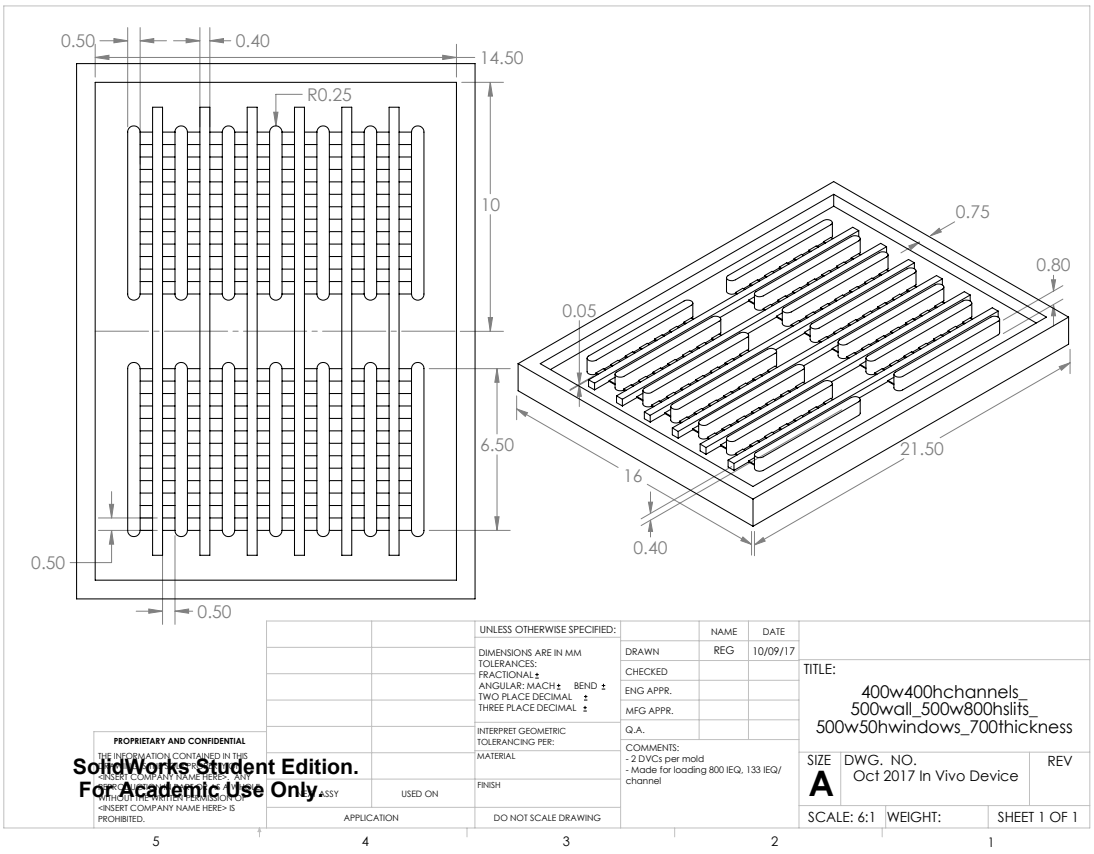

Figure A.4: Device floor mold design for islet transplant experiment 3.

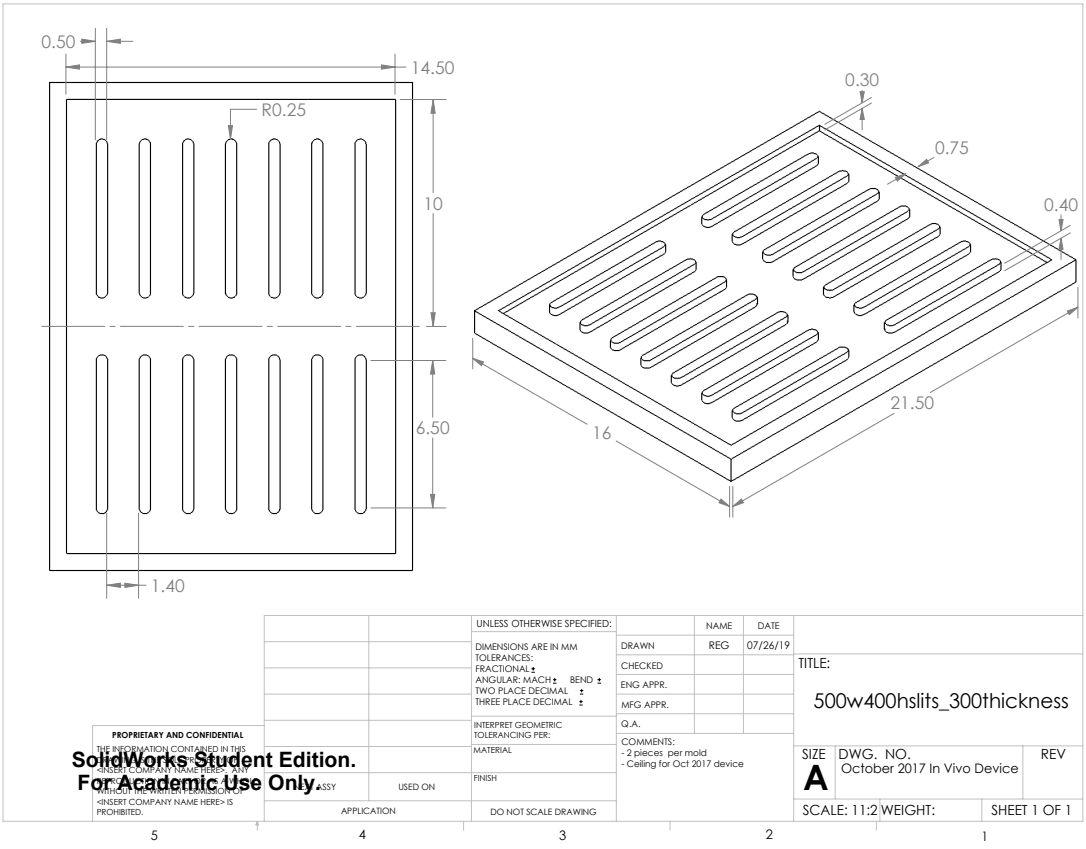

Figure A.5: Device ceiling mold design for islet transplant experiment 3.

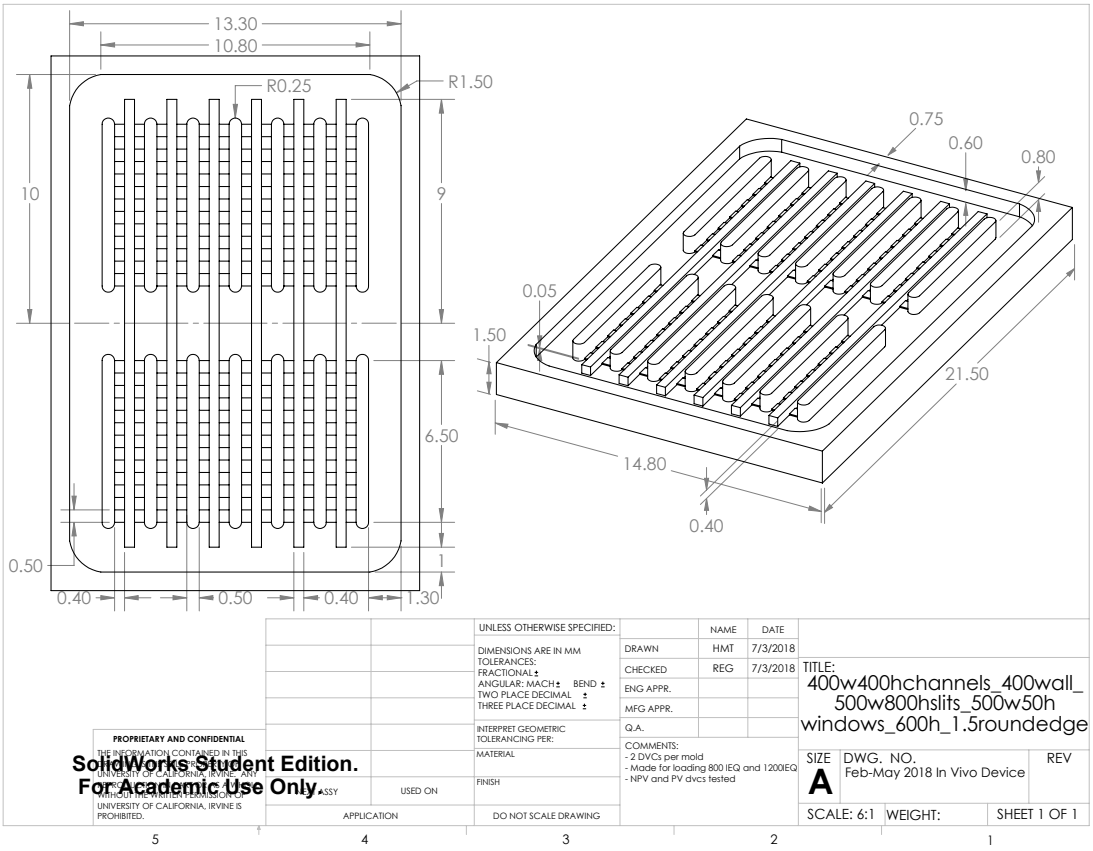

Figure A.6: Device floor mold design for islet transplant experiments 4-5.

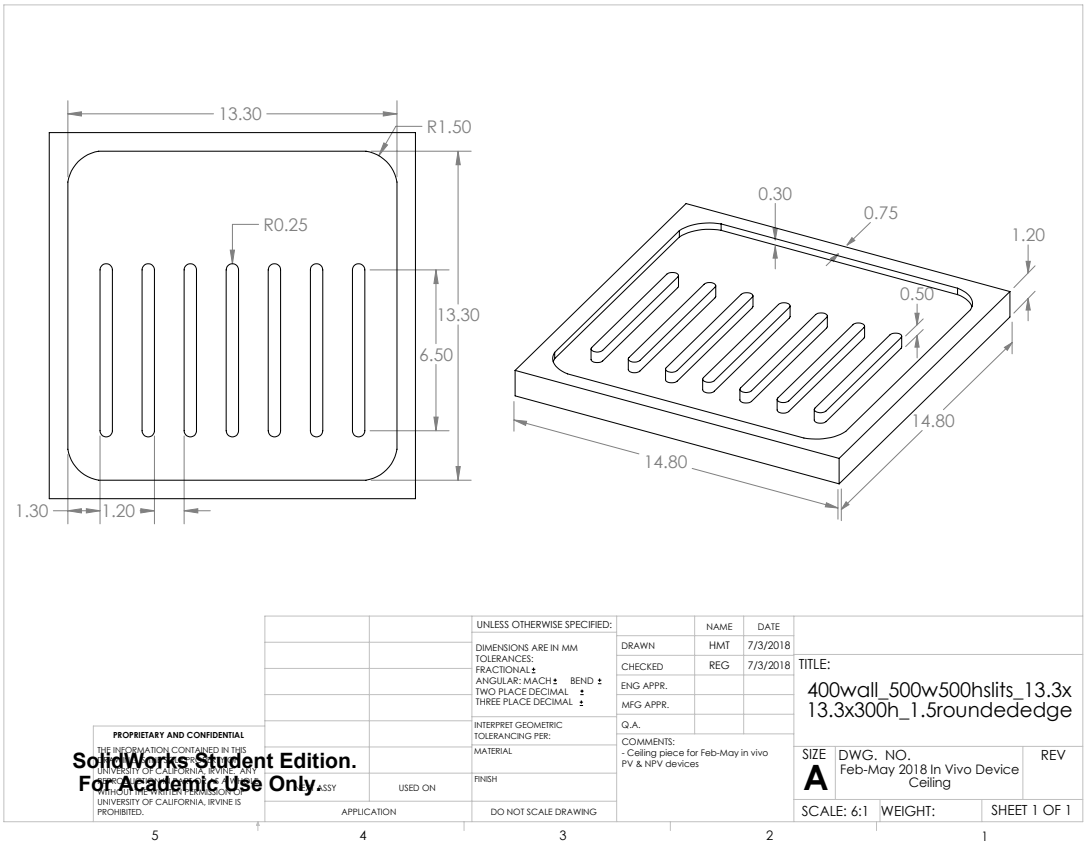

Figure A.7: Device ceiling mold design for islet transplant experiments 4-5.

Modeling MATLAB code

```
clc; clear all; close all
%Transport Constants
DO2water=3000; %from Buchwald 2018 %Diffusion coefficient of oxygen through
water in micron^2/s
D_A_water(1) = DO2water; %A=1 is Oxygen
%DO2tissue=1700; %from Datta textbook pg 427  %Diffusion coefficient of
oxygen through tissue in micron^2/s
DO2tissue=2000; %from paper Buchwald 2018 %Diffusion coefficient of oxygen
through tissue in micron^2/s
D_A_tissue(1) = DO2tissue; %A=1 is Oxygen
DO2pdms=3000;  %Diffusion coefficient of oxygen through PDMS in micron^2/s
D_A_pdms(1) = DO2pdms; %A=1 is Oxygen
Dgluwater=900;  %Diffusion coefficient of glucose through water in
micron^2/s
D_A_water(2) = Dgluwater; %A=2 is glucose
Dglutissue=300;  %Diffusion coefficient of glucose through tissue in
micron^2/s
D_A_tissue(2) = Dglutissue; %A=2 is glucose
Dglupdms=0;   %Diffusion coefficient of glucose through PDMS in micron^2/s
D_A_pdms(2) = Dglupdms; %A=2 is glucose

C_A_media_infinity(1)=0.2e-19; % Concentration of oxygen in the media in
units of mol/(microns^3), Buchwald 2018
C_A_media_infinity(2) = 0.02124*(1/1000)*((1/(10^4))^3)*(1/180);
%Concentration of glucose in the media in mol/(microns^3)
%https://www.sigmaaldrich.com/content/dam/sigma-
aldrich/docs/Sigma/Datasheet/c0422dat.pdf
C_O2_blood = 9.3e-18; %concentration of oxygen in an arterial blood vessel
in units of mol/(microns^3), assumes full Hb concentration and about 0.15
gHb/ml blood
R_gencons(1)=-3.4e-20; %from Buchwald 2018 %Oxygen consumption by islets --
some average value, no relationship with insulin production known
R_gencons(2) = -2.8e-20; %from Buchwald 2018 %Glucose consumption by islets
-- some average value
R_gencons(3) = 3e-23;%Maximum insulin secretion rate in phase 2 Buchwald
Theoretical Biology and Medical Modelling 2011, 8:20; units of
mol/(micron^3 s)
CHF_Glucose = (1e-20); %hill function parameter units of mol/micron^3
CHF_Insulin = 7e-18; %Buchwald 2011
n_insulin = 2.5; %Buchwald 2011, no units, power in hill function
R_use_I = 1.6e-14; %use of insulin by the body mol/(s)
R_body_con = 10; %the body consumption of glucose in mg/(dL*min)

%Geometry constants
rtube=184;   %Radius of the tube in microns
L=1000; %Length of repeating (i.e. symmetric) segments in microns
Hfloor=500; %height of bottom of device in microns
Wfloor=400; %width of bottom of device in microns
Afloor=2*2*Hfloor*Wfloor; %area of both floor and symmetric ceiling in
microns
Lfloor=300; %length of the floor and ceiling portions in microns

Hslit=500; %height of the slit in microns
Wslit=1000; %width of the slit in microns
Aslit=Hslit*Wslit; %area of the slit in microns^2
Lslit=650; %length of the slit in microns
```

```
Hwindow=50; %height of the window in microns
Wwindow=500; %width of the window in microns
Awindow=Hwindow*Wwindow; %area of the window in microns^2
Lwindow=400; %length of the window in microns

Hwall=400; %height of the wall in microns
Wwall=1000; %width of the wall in microns
Awall=Hwall*Wwall-Awindow; %area of of the wall discounting the part that
is taken by the window in microns^2
Lwall=400; %length of the wall in microns

%Convection Constants
Acap=Awindow; %In the presence of convection the area of window is the
maximum possible contact area
Sh = 3; %An approximation from Table 1, Huang 1997
L_c = 10; %The characteristic length is the diamter of the likely
capilarries inside the window in microns
hmass= Sh.*D_A_water./L_c; %(micron/s)convective mass transport coefficient
assumes diffusion inside the capillary is through the plasma of the blood,
which is close enough to water for transport

%Calculate Resistances for all components
Rfloor=Lfloor./(D_A_pdms.*Afloor); %Resistance of the floor and ceiling
portion s/(microns^3)
One_over_Rwall=(D_A_pdms.*Awall)./Lwall; %one over the resistance of the
wall to transport in s/(microns^3)
Rslit_vivo=Lslit./(D_A_tissue.*Aslit); %in vivo resistance of transport
from the slit in s/(microns^3)
Rslit_vitro=Lslit./(D_A_water.*Aslit); %in vitro resistance of transport
from the slit in s/(microns^3)
Rwindow_vivo=Lwindow./(D_A_tissue.*Awindow); %in vivo resistance of the
window in s/(microns^3)
Rwindow_vitro=Lwindow./(D_A_water.*Awindow); %in vitro resistance of the
window in s/(microns^3)

%Calculate combined resistances
Rchannelside_vitro=1./(One_over_Rwall+1./Rwindow_vitro); %wall and window
are in parellel
Rchannelside_vivo=1./(One_over_Rwall+1./Rwindow_vivo); %wall and window are
in parellel
Rside_vitro=Rslit_vitro+Rchannelside_vitro; %sides in parellel with slit
Rside_vivo=Rslit_vivo+Rchannelside_vivo; %sides in parellel with slit

%Total in vitro resistance
Rt_vitro=1./((1./Rfloor)+(1./Rside_vitro)); %the total resistance in vitro

%Solve for the radius where either the dead cells begin or glucose does not
reach
packing_fraction = 0.05:0.05:1; %vector for varying packing fractions
for j=1:length(packing_fraction)
    fact(1) = packing_fraction(j); %change for oxygen
    fact(2) = packing_fraction(j); %no change for glucose
    for i=1:2
        R_A_fac = fact(i)*R_gencons(i);
```

```
        %r_max(i,j) = sqrt((-
4*C_A_media_infinity(i)*D_A_tissue(i)/R_A_fac)*(1-pi()*L_c*Rt_vitro(i)));
%cylinder
        r_max(i,j) = sqrt((-
4*C_A_media_infinity(i)*D_A_tissue(i)/R_A_fac)); %cylinder no perfusion
        r_max_sph(i,j) = sqrt((-
6*C_A_media_infinity(i)*D_A_tissue(i)/R_A_fac)); %sphere no resistance

        C_As_limit(i) = -(1/4).*(rtube^2).*R_A_fac./(D_A_tissue(i));
    end
end

figure(1)
plot(packing_fraction,2.*r_max_sph(1,:),'b','LineWidth',3)
ylabel('Length Dimension (µm)');
xlabel('Cell Packing Fraction (au)');
figure(1)
hold on
plot(packing_fraction,r_max(1,:),'r','LineWidth',3)
plot(packing_fraction,150.*ones(size(packing_fraction)),'k','LineWidth',2)
plot(packing_fraction,rtube.*ones(size(packing_fraction)),'g','LineWidth',2
)
legend('Sphere Diameter','Cylinder Radius','Survivable Islet
Diameter','Tube Radius');
set(gca,'FontSize',15);

%Calculate the packing fraction based on the oxygen concentration, In vitro
for checking
x_pf_media = -
(4*C_A_media_infinity(1)*D_A_tissue(1))/((rtube^2)*R_gencons(1));

%In vivo Oxygen
x_pf_vivo_temp = -
(4.*D_A_tissue(1).*C_O2_blood)/(((rtube^2)*R_gencons(1))*(4.*D_A_tissue(1).
*(pi()*L/(hmass(1)*Acap))+1));
if x_pf_vivo_temp>1
    x_pf_vivo = 1;

    A_cap_min = -
((4.*D_A_tissue(1))*pi()*L*(rtube^2)*R_gencons(1)*x_pf_vivo)/(hmass(1)*((rt
ube^2)*R_gencons(1)*x_pf_vivo+C_O2_blood*4.*D_A_tissue(1)));
    VascFrac = A_cap_min/Awindow;

else
    x_pf_vivo = x_pf_vivo_temp;
end

%Rconv=1/(hmass*A_contact); This is the equation for the convective
resistance, but it will be put in terms of actual variables into the total
resistance to avoid issues with infinity when A_contact is zero

%Vary the area of contact from the minimum to the max
%A_cont_vec = [linspace(0.5*A_cap_min,0.12*Acap,8)
linspace(0.12*Acap,Acap,4)];

A_cont_vec = [0.5*A_cap_min,0.8*A_cap_min, A_cap_min, 0.05*Acap, 0.12*Acap,
0.12*Acap, 0.5*Acap, Acap];
```

```
%Minimum an maximum glucose concentration, units of %mol/micron^3
C_G_min = 3e-18; C_G_max = 3e-17;
C_G_vec = linspace(C_G_min,C_G_max,100);
time_vec = 0:1:120; %time in minutes

%Vary packing fraction
x_pf_vec = linspace(0.5,1,50);

formatSpec = 'Perfusion %.3f, Packing Fraction %.2f.';

for j = 1:length(A_cont_vec)
    A_contact = A_cont_vec(j); %contact area
    %Total resistance (use only for glucose as O2 has been calculated with
a different concentration;

    Rt_vivo=1./((1./Rfloor)+(1./Rside_vivo)+(hmass.*A_contact)); %the total
resistance in vivo

    %Careful if the first contact area is greater than A_cap_min this might
    %be a problem with the if statment set-up
    if A_contact < A_cap_min
        x_pf = -
(4.*D_A_tissue(1).*C_O2_blood)/(((rtube^2)*R_gencons(1))*(4.*D_A_tissue(1).
*(pi()*L/(hmass(1)*A_contact))+1));
    else if j > 1
            if A_cont_vec(j) == A_cont_vec(j-1)
                x_pf = 0.5;

            else
                x_pf = 1;
            end
        end
    end
    for k = 1:length(C_G_vec)
        C_G_inf = C_G_vec(k); %concentration of glucose in the blood/tissue
        %Average glucose consumption rate
        R_G_temp = -(C_G_inf/((rtube^2)*(pi()*L*Rt_vivo(2) +
(1/(4*D_A_tissue(2))))))./x_pf;
        R_G(k,j) = max(R_G_temp, R_gencons(2));
        %Average glucose consumption rate for the whole device
        Q_Glucose_device(k,j) = x_pf.*R_G(k,j)*(pi()*(rtube^2)*L)*(6*6.5);
        Q_no_limits_device(k,j) =
x_pf.*R_G_temp*(pi()*(rtube^2)*L)*(6*6.5); %no limits on the consumption
rate

        %Concentration at the tube
        C_G_Surface(k,j) =
C_G_inf+pi()*L*Rt_vivo(2)*(rtube^2)*R_G(k,j)*x_pf;
        %         if C_G_Surface(k,j) < 0.5*C_G_max
        %             R_I(k,j) = R_gencons(3).*(C_G_Surface(k,j)/C_G_max);
        %             R_I_device(k,j) =
R_I(k,j)*(pi()*(rtube^2)*L*x_pf)*(6*6.5);%mol/s
        %         else
        %             R_I(k,j) = R_gencons(3).*(0.5*C_G_max/C_G_max);
        %             R_I_device(k,j) =
R_I(k,j)*(pi()*(rtube^2)*L*x_pf)*(6*6.5);%mol/s
```

```
        %         end
        rad_integr = linspace(0,rtube,2000);

        Q_temp = 0;

        for p=2:(length(rad_integr))
            C_G_cyl =
C_G_Surface(k,j)+(x_pf*R_G(k,j)/(4*D_A_tissue(2)))*((rtube^2)-
((rad_integr(p))^2));
            R_insulin =
R_gencons(3)*(C_G_cyl^n_insulin)/((C_G_cyl^n_insulin) +
(CHF_Insulin^n_insulin));

            Q_temp = Q_temp +
2*L*pi*((rad_integr(p))*x_pf*R_insulin)*(rad_integr(p)-rad_integr(p-1));
        end
        Q_Insulin(k,j) = Q_temp*(6*6.5);
        Q_quest(k,j) = R_gencons(3).*(pi()*(rtube^2)*L*x_pf)*(6*6.5);

        %Clearance rate
        %         R_G_Clearance(k,j) = R_I_device(k,j)*R_body_con/R_use_I;
%units of mg/(dL*min)
        %         C_G_body(:,k,j) = ones(size(time_vec)).*(C_G_inf*(50/3e-
18)) - (R_G_Clearance(k,j)).*time_vec;
    end

    %figure(2)
    %plot(C_G_vec,(R_G(:,j)./R_gencons(2)),'LineWidth',2)
    %hold on;

    str = sprintf(formatSpec,(A_contact/Acap),x_pf);
    legend_vec{j} = str;

    figure(3)
    p3=plot(C_G_vec,((Q_Insulin(:,j))*(1e12)),'-','LineWidth',2);
    hold on;
    % plot(C_G_vec,((Q_quest(:,j))*(1e12)),'.-')

    figure(4)
    p4=plot(C_G_vec,-Q_Glucose_device(:,j),'LineWidth',2);
    hold on;

    %figure(5)
    %plot(C_G_vec,-Q_no_limits_device(:,j),'LineWidth',2)
    %hold on;

    figure(7)
    p7=plot(C_G_vec,C_G_Surface(:,j),'LineWidth',2);
    hold on;

    for k = 1:length(x_pf_vec)
        C_G_inf = C_G_min+0.9*(C_G_max-C_G_min);
        x_pf = x_pf_vec(k); %packing fraction
        %Average glucose consumption rate
        R_G_temp = -(C_G_inf/((rtube^2)*(pi()*L*Rt_vivo(2) +
(1/(4*D_A_tissue(2))))))./(x_pf);
```

```
        R_G_PackFrac(k,j) = max(R_G_temp, R_gencons(2)); %consumption rate
cannot go above maximum
        Q_Glucose_device_pk(k,j) =
R_G_PackFrac(k,j)*(x_pf*pi()*(rtube^2)*L)*(6*6.5);
    end
    %figure(6)
    %plot(x_pf_vec,(-Q_Glucose_device_pk(:,j)),'LineWidth',2)
    %hold on;

end

%figure(2)
%xlabel('Concentration of Glucose (mol/micron^3)')
%ylabel('Average Glucose consumption Rate Normalized by max')
%lgd = legend(legend_vec);
%title('Varying Perfusion contact area fraction')

figure(3)
xlabel('Blood Glucose Concentration (mol/μm^3)','FontSize',15);
ylabel('Total Insulin Production Rate by Device (pmol/s)','FontSize',15);
legend(legend_vec)
%title('Varying Perfusion contact area fraction')
p3(1).Color = 'k';

figure(4)
xlabel('Blood Glucose Concentration (mol/μm^3)','FontSize',15);
ylabel('Total Glucose Consumption Rate in Device (mol/s)','FontSize',15);
legend(legend_vec)
%title('')
p4(1).Color = 'k';

%figure(5)
%xlabel('Concentration of Glucose (mol/micron^3)')
%ylabel('Total Glucose Consumption Rate in Device (mol/s)')
%legend(legend_vec)
%title('No limits set on the consumption rate')

figure(7)
xlabel('Blood Glucose Concentration (mol/μm^3)','FontSize',15)
ylabel('Concentration of Glucose at Surface of Islet Tube
(mol/μm^3)','FontSize',15)
legend(legend_vec)
%title('Limits set on the consumption rate')
p7(1).Color = 'k';

%figure(6)
%xlabel('Packing Fraction of Islets')
%ylabel('Total Glucose Consumption Rate in Device (mol/s)')
%legend(legend_vec);
%title(sprintf('Varying Perfusion contact area fraction and glucose
concentration of %f', C_G_inf)
```

References

1. Atkinson MA, Eisenbarth GS, Michels AW. Type 1 diabetes. *The Lancet* 2014; 383: 69–82.
2. Juvenile Diabetes Research Foundation. Type 1 Diabetes Facts.http://www.jdrf.org/about/fact-sheets/type-1-diabetes-facts/.
3. The Diabetes Control and Complications Trial Research Group. The effect of intensive treatment of diabetes on the development and progression of long-term complications in insulin-dependent diabetes mellitus. *New England Journal of Medicine* 1993; 329: 977–986.
4. Pickup JC, Freeman SC, Sutton AJ. Glycaemic control in type 1 diabetes during real time continuous glucose monitoring compared with self monitoring of blood glucose: meta-analysis of randomised controlled trials using individual patient data. *BMJ* 2011; 343: d3805.
5. Thabit H, Tauschmann M, Allen JM, et al. Home Use of an Artificial Beta Cell in Type 1 Diabetes. *New England Journal of Medicine* 2015; 373: 2129–2140.
6. Tao B, Pietropaolo M, Atkinson MA, et al. Estimating the cost of type 1 diabetes in the U.S.A propensity score matching method. *PLoS ONE* 2010; 5: e11501.
7. Naftanel MA, Harlan DM. Pancreatic islet transplantation. *PLoS Medicine* 2004; 1: 198–201.
8. Shapiro AMJ, Pokrywczynska M, Ricordi C. Clinical pancreatic islet transplantation. *Nature Reviews Endocrinology* 2016; 13: 268–277.
9. Eberhard D, Kragl M, Lammert E. 'Giving and taking': Endothelial and β-cells in the islets of Langerhans. *Trends in Endocrinology and Metabolism* 2010; 21: 457–463.
10. Shapiro AMJ, Lakey JRT, Ryan EA, et al. Islet Transplantation in Seven Patients with Type I Diabetes Mellitus Using a Glucocorticoid-Free Immunosuppressive Regimen. *The New England Journal of Medicine* 2000; 343: 230–238.
11. Holmes-Walker DJ, Gunton JE, Payk M, et al. Islet transplantation provides superior glycemic control with less hypoglycemia compared to continuous subcutaneous insulin infusion (CSII) or multiple daily insulin injections (MDI). *Transplantation* 2017; 101: 1268–1275.
12. Khosravi-Maharlooei M, Hajizadeh-Saffar E, Tahamtani Y, et al. Therapy of endocrine disease: Islet transplantation for type 1 diabetes: So close and yet so far away. *European Journal of Endocrinology* 2015; 173: R165–R183.
13. de Vos P, Marchetti P. Encapsulation of pancreatic islets for transplantation in diabetes: the untouchable islets. *Trends in Molecular Medicine* 2002; 8: 363–366.
14. Lim F, Sun AM. Microencapsulated islets as bioartificial endocrine pancreas. *Science* 1980; 210: 908–910.
15. de Vos P, Faas MM, Strand BL, et al. Alginate-based microcapsules for immunoisolation of pancreatic islets. *Biomaterials* 2006; 27: 5603–5617.
16. de Vos P, van Hoogmoed CG, van Zanten J, et al. Long-term biocompatibility, chemistry, and function of microencapsulated pancreatic islets. *Biomaterials* 2003; 24: 305–312.
17. Paredes-Juarez GA, Spasojevic M, Faas MM, et al. Immunological and Technical Considerations in Application of Alginate-Based Microencapsulation Systems. *Frontiers in Bioengineering and Biotechnology* 2014; 2: 1–15.
18. Kang A, Park J, Ju J, et al. Cell encapsulation via microtechnologies. *Biomaterials* 2014; 35: 2651–2663.
19. Johansson Å, Olerud J, Johansson M, et al. Angiostatic factors normally restrict islet endothelial cell proliferation and migration: Implications for islet

transplantation. *Transplant International* 2009; 22: 1182–1188.
20. Desai T, Shea LD. Advances in islet encapsulation technologies. *Nature Reviews Drug Discovery* 2016; 16: 338–350.
21. Weir GC. Islet encapsulation: Advances and obstacles. *Diabetologia* 2013; 56: 1458–1461.
22. Song S, Roy S. Progress and challenges in macroencapsulation approaches for type 1 diabetes (T1D) treatment: Cells, biomaterials, and devices. *Biotechnology and Bioengineering* 2016; 113: 1381–1402.
23. Krishnan R, Ko D, Tucker T, et al. Strategies to Combat Hypoxia in Encapsulated Islet Transplantation. *Surgery: Current Research* 2016; 6: 1000259.
24. Pepper AR, Pawlick RL, Gala-Lopez B, et al. Diabetes Is Reversed in a Murine Model by Marginal Mass Syngeneic Islet Transplantation Using a Subcutaneous Cell Pouch Device. *Transplantation* 2015; 99: 2294–2300.
25. Kriz J, Vilk G, Mazzuca DM, et al. A novel technique for the transplantation of pancreatic islets within a vascularized device into the greater omentum to achieve insulin independence. *American Journal of Surgery* 2012; 203: 793–7.
26. Gala-Lopez BL, Pepper AR, Dinyari P, et al. Subcutaneous clinical islet transplantation in a prevascularized subcutaneous pouch – preliminary experience. *CellR4* 2016; 4: e2132.
27. Colton CK, Weir GC. Commentary – A hard lesson about transplanting islets into prevascularized devices. *CellR4* 2017; 5: 1–4.
28. Roscioni SS, Migliorini A, Gegg M, et al. Impact of islet architecture on β-cell heterogeneity, plasticity and function. *Nature Reviews Endocrinology* 2016; 12: 695–709.
29. Bonner-Weir S. Morphological evidence for pancreatic polarity of beta-cell within islets of langerhans. *Diabetes* 1988; 37: 616–621.
30. Narayanan S, Loganathan G, Dhanasekaran M, et al. Intra-islet endothelial cell and β-cell crosstalk: Implication for islet cell transplantation. *World Journal of Surgery* 2017; 7: 117–128.
31. Sakata N, Aoki T, Yoshimatsu G, et al. Strategy for clinical setting in intramuscular and subcutaneous islet transplantation. *Diabetes/Metabolism Research and Reviews* 2014; 30: 1–10.
32. Bromberg JS. Islet implantation in a pocket. *Nature Biotechnology* 2015; 33: 493–494.
33. Kemp CB, Knight MJ, Scharp DW, et al. Effect of transplantation site on the results of pancreatic islet isografts in diabetic rats. *Diabetologia* 1973; 9: 486–491.
34. Pepper AR, Gala-Lopez B, Pawlick RL, et al. A prevascularized subcutaneous device-less site for islet and cellular transplantation. *Nature Biotechnology* 2015; 33: 518–23.
35. Rajab A. Islet transplantation: Alternative sites. *Current Diabetes Reports* 2010; 10: 332–337.
36. Andrades P, Asiedu C, Rodriguez C, et al. Subcutaneous Pancreatic Islet Transplantation Using Fibrin Glue as a Carrier. *Transplantation Proceedings* 2007; 39: 191–192.
37. Kim JS, Lim JH, Nam HY, et al. In situ application of hydrogel-type fibrin-islet composite optimized for rapid glycemic control by subcutaneous xenogeneic porcine islet transplantation. *Journal of Controlled Release* 2012; 162: 382–390.
38. Bhang SH, Jung MJ, Shin J-Y, et al. Mutual effect of subcutaneously transplanted human adipose-derived stem cells and pancreatic islets within fibrin gel. *Biomaterials* 2013; 34: 7247–7256.
39. Najjar M, Manzoli V, Villa C, et al. Fibrin Gels Engineered with Pro-Angiogenic Growth Factors Promote Engraftment of Pancreatic Islets in

Extrahepatic Sites in Mice. *Biotechnology and Bioengineering* 2015; 112: 1916–1926.
40. Smink AM, Li S, Hertsig DT, et al. The Efficacy of a Prevascularized, Retrievable Poly(D,L,-lactide-co-ε-caprolactone) Subcutaneous Scaffold as Transplantation Site for Pancreatic Islets. *Transplantation* 2017; 101: e112–e119.
41. Rios PD, Zhang X, Luo X, et al. Mold-casted non-degradable, islet macro-encapsulating hydrogel devices for restoration of normoglycemia in diabetic mice. *Biotechnology and Bioengineering* 2016; 9999: 1–11.
42. Weaver JD, Headen DM, Aquart J, et al. Vasculogenic hydrogel enhances islet survival, engraftment, and function in leading extrahepatic sites. *Science Advances* 2017; 3: e1700184.
43. Mahou R, Zhang DKY, Vlahos AE, et al. Injectable and inherently vascularizing semi-interpenetrating polymer network for delivering cells to the subcutaneous space. *Biomaterials* 2017; 131: 27–35.
44. Vlahos AE, Cober N, Sefton M V. Modular tissue engineering for the vascularization of subcutaneously transplanted pancreatic islets. *Proceedings of the National Academy of Sciences of the United States of America* 2017; 114: 9337–9342.
45. Wang W, Gu Y, Hori H, et al. Subcutaneous transplantation of macroencapsulated porcine pancreatic endocrine cells normalizes hyperglycemia in diabetic mice. *Transplantation* 2003; 76: 290–296.
46. Kawakami Y, Iwata H, Gu YJ, et al. Successful Subcutaneous Pancreatic Islet Transplantation Using an Angiogenic Growth Factor – Releasing Device. *Surgery* 2001; 23: 375–381.
47. Smink AM, Li S, Swart DH, et al. Stimulation of vascularization of a subcutaneous scaffold applicable for pancreatic islet-transplantation enhances immediate post-transplant islet graft function but not long-term normoglycemia. *Journal of Biomedical Materials Research Part A* 2017; 105A: 2533–2542.
48. Buitinga M, Janeczek Portalska K, Cornelissen D-J, et al. Co-culturing human islets with proangiogenic support cells to improve islet revascularization at the subcutaneous transplantation site. *Tissue Engineering Part A* 2016; 22: 375–85.
49. Botvinick EL, George SC, Shergill BS, et al. *Transplantation device and method of use, Patent Publication Number: WO2014197798 A3*. 2016.
50. Gurlin RE, Keating MT, Li S, et al. Vascularization and innervation of slits within polydimethylsiloxane sheets in the subcutaneous space of athymic nude mice. *Journal of Tissue Engineering* 2017; 8: 204173141769164.
51. Langer R, Vacanti JP. Tissue engineering. *Science* 1993; 260: 920–926.
52. Auger FA, Gibot L, Lacroix D. The pivotal role of vascularization in tissue engineering. *Annual Review of Biomedical Engineering* 2013; 15: 177–200.
53. Phelps EA, García AJ. Engineering more than a cell: Vascularization strategies in tissue engineering. *Current Opinion in Biotechnology* 2010; 21: 704–709.
54. Lovett M, Lee K, Edwards A, et al. Vascularization strategies for tissue engineering. *Tissue Engineering Part B: Reviews* 2009; 15: 353–370.
55. Stosich MS, Bastian B, Marion NW, et al. Vascularized adipose tissue grafts from human mesenchymal stem cells with bioactive cues and microchannel conduits. *Tissue Engineering* 2007; 13: 2881–90.
56. Chiu Y-C, Cheng M-H, Engel H, et al. The role of pore size on vascularization and tissue remodeling in PEG hydrogels. *Biomaterials* 2011; 32: 6045–6051.
57. Zhang W, Wray LS, Rnjak-Kovacina J, et al. Vascularization of hollow channel-modified porous silk scaffolds with endothelial cells for tissue regeneration. *Biomaterials* 2015; 56: 68–77.
58. Torisawa Y, Spina CS, Mammoto T, et al. Bone marrow-on-a-chip replicates hematopoietic niche physiology in vitro. *Nature Methods* 2014; 11: 663–9.

59. Pedraza E, Brady A-C, Fraker CA, et al. Macroporous three-dimensional PDMS scaffolds for extrahepatic islet transplantation. *Cell Transplantation* 2013; 22: 1123–35.
60. Clark RM, Cicotte KN, McGuire PG, et al. The effect of projection microstereolithographic fabricated implant geometry on myocutaneous revascularization. *Surgical Science* 2014; 5: 513–525.
61. Lundborg G, Gelberman RH, Longo FM, et al. In vivo regeneration of cut nerves encased in silicone tubes, growth across a six-millimeter gap. *Journal of Neuropathology & Experimental Neurology* 1982; 41: 412–422.
62. Rnjak-Kovacina J, Wray LS, Golinski JM, et al. Arrayed hollow channels in silk-based scaffolds provide functional outcomes for engineering critically sized tissue constructs. *Advanced Functional Materials* 2014; 24: 2188–2196.
63. Lee MK, Rich MH, Lee J, et al. A bio-inspired, microchanneled hydrogel with controlled spacing of cell adhesion ligands regulates 3D spatial organization of cells and tissue. *Biomaterials* 2015; 58: 26–34.
64. Stokols S, Sakamoto J, Breckon C, et al. Templated agarose scaffolds support linear axonal regeneration. *Tissue Engineering* 2006; 12: 2777–2787.
65. Hossain R, Kim B, Pankratz R, et al. Handcrafted multilayer PDMS microchannel scaffolds for peripheral nerve regeneration. *Biomedical Microdevices* 2015; 17: 1–9.
66. Moore MJ, Friedman JA, Lewellyn EB, et al. Multiple-channel scaffolds to promote spinal cord axon regeneration. *Biomaterials* 2006; 27: 419–429.
67. Soparkar CNS, Wong JF, Patrinely JR, et al. Growth factors embedded in an agarose matrix enhance the rate of porous polyethylene implant biointegration. *Ophthalmic Plastic and Reconstructive Surgery* 2000; 16: 341–6.
68. Sabini P, Sclafani AP, Romo III T, et al. Modulation of tissue ingrowth into porous high-density polyethylene implants with basic fibroblast growth factor and autologous blood clot. *Archives of Facial Plastic Surgery* 2009; 2: 27–33.
69. Koopal SA, Coma MI, Tiebosch ATMG, et al. Low-temperature heating overnight in tris-HCl buffer pH 9 is a good alternative for antigen retrieval in formalin-fixed paraffin-embedded tissue. *Applied Immunohistochemistry* 1998; 6: 228–233.
70. Edelstein AD, Tsuchida MA, Amodaj N, et al. Advanced methods of microscope control using μManager software. *Journal of Biological Methods* 2014; 1: 1–10.
71. Bloch K, Vanichkin A, Damshkaln LG, et al. Vascularization of wide pore agarose-gelatin cryogel scaffolds implanted subcutaneously in diabetic and non-diabetic mice. *Acta Biomaterialia* 2010; 6: 1200–1205.
72. Choi SW, Zhang Y, Macewan MR, et al. Neovascularization in biodegradable inverse opal scaffolds with uniform and precisely controlled pore sizes. *Advanced Healthcare Materials* 2013; 2: 145–154.
73. Mata M, Alessi D, Fink DJ. S100 is preferentially distributed in myelin-forming Schwann cells. *Journal of Neurocytology* 1990; 19: 432–442.
74. Brudno Y, Ennett-Shepard AB, Chen RR, et al. Enhancing microvascular formation and vessel maturation through temporal control over multiple pro-angiogenic and pro-maturation factors. *Biomaterials* 2013; 34: 9201–9209.
75. Gingras M, Paradis I, Berthod F. Nerve regeneration in a collagen-chitosan tissue-engineered skin transplanted on nude mice. *Biomaterials* 2003; 24: 1653–1661.
76. Agrawal V, Brown BN, Beattie AJ, et al. Evidence of innervation following extracellular matrix scaffold-mediated remodelling of muscular tissues. *Journal of Tissue Engineering and Regenerative Medicine* 2009; 3: 590–600.
77. Liu Q, Huang J, Shao H, et al. Dual-factor loaded functional silk fibroin scaffolds for peripheral nerve regeneration with the aid of neovascularization. *RSC Advances* 2016; 6: 7683–7691.

78. Jiang B, Waller TM, Larson JC, et al. Fibrin-loaded porous poly(ethylene glycol) hydrogels as scaffold materials for vascularized tissue formation. *Tissue Engineering Part A* 2012; 19: 120924061154007.
79. Freeman I, Cohen S. The influence of the sequential delivery of angiogenic factors from affinity-binding alginate scaffolds on vascularization. *Biomaterials* 2009; 30: 2122–2131.
80. Reinert RB, Cai Q, Hong J, et al. Vascular endothelial growth factor coordinates islet innervation via vascular scaffolding. *Development* 2014; 141: 1480–1491.
81. Smink AM, Hertsig DT, Schwab L, et al. A Retrievable, Efficacious Polymeric Scaffold for Subcutaneous Transplantation of Rat Pancreatic Islets. *Annals of Surgery* 2017; 266: 149–157.
82. Krishnan R, Arora RP, Alexander M, et al. Noninvasive evaluation of the vascular response to transplantation of alginate encapsulated islets using the dorsal skin-fold model. *Biomaterials* 2014; 35: 891–898.
83. Vajkoczy P, Menger MD, Simpson E, et al. Angiogenesis and vascularization of murine pancreatic islet isografts. *Transplantation* 1995; 60: 123–127.
84. Eter WA, Bos D, Frielink C, et al. Graft revascularization is essential for non-invasive monitoring of transplanted islets with radiolabeled exendin. *Scientific Reports* 2015; 5: 15521.
85. Weidling J, Sameni S, Lakey JRT, et al. Method measuring oxygen tension and transport within subcutaneous devices. *Journal of Biomedical Optics* 2014; 19: 087006-1–5.
86. Papkovsky DB, Zhdanov A V. Phosphorescence based O2 sensors – Essential tools for monitoring cell and tissue oxygenation and its impact on metabolism. *Free Radical Biology and Medicine* 2016; 101: 202–210.
87. Najdahmadi A. *Tissue Engineering and Biosensing, Towards Cure and Control of Diabetes*. 2018.
88. Zhang M. *Optical Oxygen Sensing in the Murine Subcutaneous Space for Islet Transplantation*. 2019.
89. Kurtz SM. *PEEK Biomaterials Handbook*. 2012.
90. Neufeld T, Ludwig B, Barkai U, et al. The Efficacy of an Immunoisolating Membrane System for Islet Xenotransplantation in Minipigs. *PLoS ONE* 2013; 8: e70150.
91. Ludwig B, Rotem A, Schmid J, et al. Improvement of islet function in a bioartificial pancreas by enhanced oxygen supply and growth hormone releasing hormone agonist. *Proceedings of the National Academy of Sciences of the United States of America* 2012; 109: 5022–5027.
92. Zekorn T, Siebers U, Bretzel RG, et al. Protetction of islets of langerhans from interleukin-1 toxicity by artificial membranes. *Transplantation* 1990; 50: 391–394.
93. Buchwald P, Bocca N, Marzorati S, et al. Feasibility of localized immunosuppression: 1. Exploratory studies with glucocorticoids in a biohybrid device designed for cell transplantation. *Pharmazie* 2010; 65: 421–428.
94. Carter JD, Dula SB, Corbin KL, et al. A practical guide to rodent islet isolation and assessment. *Biological Procedures Online* 2009; 11: 3–31.
95. Hirabaru M, Kuroki T, Adachi T, et al. A Method for Performing Islet Transplantation Using Tissue-Engineered Sheets of Islets and Mesenchymal Stem Cells. *Tissue Engineering Part C: Methods* 2015; 21: 1205–1215.
96. Kang J, Erdodi G, Kennedy JP, et al. Toward a bioartificial pancreas: Diffusion of insulin and IgG across immunoprotective membranes with controlled hydrophilic channel diameters. *Macromolecular Bioscience* 2010; 10: 369–377.
97. Schindelin J, Arganda-Carreras I, Frise E, et al. Fiji: An open-source platform for biological-image analysis. *Nature Methods* 2012; 9: 676–682.
98. Szot GL, Koudria P, Bluestone JA. Transplantation of Pancreatic Islets Into

the Kidney Capsule of Diabetic Mice. *Journal of Visualized Experiments* 2007; 2–3.
99. Juang J-H, Bonner-Weir S, Ogawa Y, et al. Outcome of subcutaneous islet transplantation improved by polymer device. *Transplantation* 1996; 61: 1557–1561.
100. Suszynski TM, Avgoustiniatos ES, Papas KK. Intraportal Islet Oxygenation. *Journal of Diabetes Science and Technology* 2014; 8: 575–580.
101. Papas KK, Avgoustiniatos ES, Suszynski TM. Effect of oxygen supply on the size of implantable islet-containing encapsulation devices. *Edizioni Minerva Medica* 2016; 58: 72–77.
102. Colton CK. Oxygen supply to encapsulated therapeutic cells. *Advanced Drug Delivery Reviews* 2014; 67–68: 93–110.
103. Komatsu H, Rawson J, Barriga A, et al. Posttransplant oxygen inhalation improves the outcome of subcutaneous islet transplantation: A promising clinical alternative to the conventional intrahepatic site. *American Journal of Transplantation* 2018; 18: 832–842.
104. Komatsu H, Kandeel F, Mullen Y. Impact of Oxygen on Pancreatic Islet Survival. *Pancreas* 2018; 47: 533–543.
105. Ward WK. A review of the foreign-body response to subcutaneously-implanted devices: the role of macrophages and cytokines in biofouling and fibrosis. *Journal of Diabetes Science and Technology* 2008; 2: 768–77.
106. Anderson JM. Biological Responses to Materials. *Annual Review of Materials Research* 2001; 31: 81–110.
107. van Amerongen MJ, Molema G, Plantinga J, et al. Neovascularization and vascular markers in a foreign body reaction to subcutaneously implanted degradable biomaterial in mice. *Angiogenesis* 2002; 5: 173–180.
108. DiPietro LA. Angiogenesis and wound repair: when enough is enough. *Journal of Leukocyte Biology* 2016; 100: 979–984.
109. Lablanche S, Vantyghem MC, Kessler L, et al. Islet transplantation versus insulin therapy in patients with type 1 diabetes with severe hypoglycaemia or poorly controlled glycaemia after kidney transplantation (TRIMECO): a multicentre, randomised controlled trial. *The Lancet Diabetes and Endocrinology* 2018; 6: 527–537.
110. Ryan EE, Paty BW, Senior PA, et al. Risks and side effects of islet transplantation. *Current Diabetes Reports* 2004; 4: 304–309.
111. Ryan EA, Paty BW, Senior PA, et al. Five-year follow-up after clinical islet transplantation. *Diabetes* 2005; 54: 2060–2069.
112. Vériter S, Gianello P, Dufrane D. Bioengineered sites for islet cell transplantation. *Current Diabetes Reports* 2013; 13: 745–755.
113. Zanone M, Favaro E, Camussi G. From Endothelial to β Cells: Insights into Pancreatic Islet Microendothelium. *Current Diabetes Reviews* 2008; 4: 1–9.
114. Carlsson P-O, Palm F, Andersson A, et al. Markedly Decreased Oxygen Tension in Transplanted Rat Pancreatic Islets Irrespective of the Implantation Site. *Diabetes* 2001; 50: 489–95.
115. Simeonovic CJ, Dhall DP, Wilson JD, et al. A comparative study of transplant sites for endocrine tissue transplantation in the pig. *The Australian Journal of Experimental Biology and Medical Science* 1986; 64 (Pt 1): 37–41.
116. Pepper AR, Gala-Lopez B, Pawlick RL, et al. A prevascularized subcutaneous device-less site for islet and cellular transplantation - Supplement. *Nature Biotechnology* 2015; 33: 518–523.
117. Millman JR, Xie C, van Dervort A, et al. Generation of stem cell-derived β-cells from patients with type 1 diabetes. *Nature Communications* 2016; 7: 11463.
118. Pagliuca FW, Millman JR, Gürtler M, et al. Generation of Functional Human

Pancreatic β Cells In Vitro. *Cell* 2014; 159: 428–439.
119. Frei AW, Li Y, Jiang K, et al. Local delivery of fingolimod from three-dimensional scaffolds impacts islet graft efficacy and microenvironment in a murine diabetic model. *Journal of Tissue Engineering and Regenerative Medicine* 2018; 12: 393–404.
120. Weaver JD, Song Y, Yang EY, et al. Controlled Release of Dexamethasone from Organosilicone Constructs for Local Modulation of Inflammation in Islet Transplantation. *Tissue Engineering Part A* 2015; 21: 2250–2261.
121. Jiang K, Weaver JD, Li Y, et al. Local release of dexamethasone from macroporous scaffolds accelerates islet transplant engraftment by promotion of anti-inflammatory M2 macrophages. *Biomaterials* 2017; 114: 71–81.
122. Zmuda EJ, Powell CA, Hai T. A Method for Murine Islet Isolation and Subcapsular Kidney Transplantation. *Journal of Visualized Experiments* 2011; 1–11.
123. Clark PM. Assays for insulin, proinsulin(s) and C-peptide. *Annals of Clinical Biochemistry* 1999; 36: 541–564.
124. Lucas T, Waisman A, Ranjan R, et al. Differential Roles of Macrophages in Diverse Phases of Skin Repair. *The Journal of Immunology* 2010; 184: 3964–3977.
125. Yu T, Wang W, Nassiri S, et al. Temporal and spatial distribution of macrophage phenotype markers in the foreign body response to glutaraldehyde-crosslinked gelatin hydrogels. *Journal of Biomaterials Science, Polymer Edition* 2016; 27: 721–742.
126. Giraldo JA, Molano RD, Rengifo HR, et al. The impact of cell surface PEGylation and short-course immunotherapy on islet graft survival in an allogeneic murine model. *Acta Biomaterialia* 2017; 49: 272–283.
127. Dollinger C, Ndreu-Halili A, Uka A, et al. Controlling Incoming Macrophages to Implants: Responsiveness of Macrophages to Gelatin Micropatterns under M1/M2 Phenotype Defining Biochemical Stimulations. *Advanced Biosystems* 2017; 1: 1700041.
128. Deeds MC, Anderson JM, Armstrong AS, et al. Single dose streptozotocin-induced diabetes: considerations for study design in islet transplantation models. *Laboratory Animals* 2011; 45: 131–40.
129. Anderson JM, Rodriguez A, Chang DT. Foreign body reaction to biomaterials. *Seminars in Immunology* 2008; 20: 86–100.
130. Ratner BD, Bryant SJ. Biomaterials: Where We Have Been and Where We Are Going. *Annual Review of Biomedical Engineering* 2004; 6: 41–75.
131. Veiseh O, Doloff JC, Ma M, et al. Size- and shape-dependent foreign body immune response to materials implanted in rodents and non-human primates. *Nature Materials* 2015; 14: 643–51.
132. Sussman EM, Halpin MC, Muster J, et al. Porous implants modulate healing and induce shifts in local macrophage polarization in the foreign body reaction. *Annals of Biomedical Engineering* 2014; 42: 1508–1516.
133. Luu TU, Gott SC, Woo BWK, et al. Micro- and Nanopatterned Topographical Cues for Regulating Macrophage Cell Shape and Phenotype. *ACS Applied Materials and Interfaces* 2015; 7: 28665–28672.
134. Salthouse TN. Some aspects of macrophage behavior at the implant interface. *Journal of Biomedical Materials Research* 1984; 18: 395–401.
135. Klopfleisch R. Macrophage reaction against biomaterials in the mouse model – phenotypes, functions and markers. *Acta Biomaterialia* 2016; 43: 3–13.
136. Ahmed TAE, Dare E V., Hincke M. Fibrin: a versatile scaffold for tissue engineering applications. *Tissue Engineering Part B: Reviews* 2008; 14: 199–215.
137. Hamamoto Y, Tsuura Y, Fujimoto S, et al. Recovery of function and mass of endogenous β-cells in streptozotocin-induced diabetic rats treated with islet

transplantation. *Biochemical and Biophysical Research Communications* 2001; 287: 104–109.
138. Schiettecatte J, Anckaert E, Smitz J. Interferences in immunoassays. In: *Advances in Immunoassay Technology*. 2012, pp. 45–62.
139. Cabrera O, Berman DM, Kenyon NS, et al. The unique cytoarchitecture of human pancreatic islets has implications for islet cell function. *Proceedings of the National Academy of Sciences of the United States of America* 2006; 103: 2334–9.
140. Brissova M, Fowler MJ, Nicholson WE, et al. Assessment of Human Pancreatic Islet Architecture and Composition by Laser Scanning Confocal Microscopy. *Journal of Histochemistry and Cytochemistry* 2005; 53: 1087–1097.
141. Buchwald P, Tamayo-Garcia A, Manzoli V, et al. Glucose-stimulated insulin release: Parallel perifusion studies of free and hydrogel encapsulated human pancreatic islets. *Biotechnology and Bioengineering* 2018; 115: 232–245.
142. Markov DA, Lillie EM, Garbett SP, et al. Variation in diffusion of gases through PDMS due to plasma surface treatment and storage conditions. *Biomedical Microdevices* 2014; 16: 91–96.
143. Buchwald P. FEM-based oxygen consumption and cell viability models for avascular pancreatic islets. *Theoretical Biology & Medical Modelling* 2009; 6: 5.
144. Hall JE. *Guyton and Hall Textbook of Medical Physiology*. 13th ed. Elsevier, 2016.
145. Huang ZJ, Tarbell JM. Numerical simulation of mass transfer in porous media of blood vessel walls. *The American Journal of Pathology* 1997; 273: H464–H477.
146. Çengel YA, Ghajar AJ. *Heat and Mass Transfer: Fundamentals & Applications*. 5th ed. McGraw-Hill Education, 2015.
147. Buchwald P. A local glucose-and oxygen concentration-based insulin secretion model for pancreatic islets. *Theoretical Biology & Medical Modelling* 2011; 8: 20.
148. Riopel M, Trinder M, Wang R. Fibrin, a Scaffold Material for Islet Transplantation and Pancreatic Endocrine Tissue Engineering. *Tissue Engineering Part B: Reviews* 2015; 21: 34–44.
149. Brady A, Martino MM, Pedraza E, et al. Proangiogenic hydrogels within macroporous scaffolds enhance islet engraftment in an extrahepatic site. *Tissue Engineering Part A* 2013; 19: 2544–52.
150. Cantarelli E, Citro A, Marzorati S, et al. Murine animal models for preclinical islet transplantation. *Islets* 2013; 5: 79–86.
151. Stokes RA, Cheng K, Lalwani A, et al. Transplantation sites for human and murine islets. *Diabetologia* 2017; 60: 1961–1971.
152. Cantarelli E, Piemonti L. Alternative transplantation sites for pancreatic islet grafts. *Current Diabetes Reports* 2011; 11: 364–374.
153. Eriksson O, Mintz A, Liu C, et al. On the use of [18F]DOPA as an imaging biomarker for transplanted islet mass. *Annals of Nuclear Medicine* 2014; 28: 47–52.
154. Liang S, Louchami K, Holvoet B, et al. Tri-modal In vivo Imaging of Pancreatic Islets Transplanted Subcutaneously in Mice. *Molecular Imaging and Biology* 2018; 20: 940–951.
155. Sneddon JB, Tang Q, Stock P, et al. Stem Cell Therapies for Treating Diabetes: Progress and Remaining Challenges. *Cell Stem Cell* 2018; 22: 810–823.
156. Nasr M Ben, Vergani A, Avruch J, et al. Co-transplantation of autologous MSCs delays islet allograft rejection and generates a local immunoprivileged site. *Acta Diabetologica* 2015; 52: 917–927.
157. Halberstadt C, Emerich DF, Gores P. Use of Sertoli cell transplants to provide local immunoprotection for tissue grafts. *Expert Opinion on Biological Therapy* 2004; 4: 813–825.

158. Pepper AR, Pawlick RL, Bruni A, et al. Harnessing the Foreign Body Reaction in Marginal Mass Device-less Subcutaneous Islet Transplantation in Mice. *Transplantation* 2016; 100: 1474–1479.
159. Yasunami Y, Nakafusa Y, Nitta N, et al. A novel subcutaneous site of islet transplantation superior to the liver. *Transplantation* 2018; 102: 1.
160. Perez-Basterrechea M, Briones RM, Alvarez-Viejo M, et al. Plasma-fibroblast gel as scaffold for islet transplantation. *Tissue Engineering Part A* 2009; 15: 569–577.
161. Kim JS, Jung Y, Kim SH, et al. Vascularization of PLGA-based bio-artificial beds by hypoxia-preconditioned mesenchymal stem cells for subcutaneous xenogeneic islet transplantation. *Xenotransplantation* 2019; 26: 1–10.
162. Giraldo JA, Weaver JD, Stabler CL. Enhancing clinical islet transplantation through tissue engineering strategies. *Journal of Diabetes Science and Technology* 2010; 4: 1238–1247.
163. Hering BJ, Kandaswamy R, Ansite JD, et al. Single-Donor, Marginal-Dose Islet Transplantation in Patients With Type 1 Diabetes. *JAMA* 2005; 293: 830–835.
164. Ahearn AJ, Parekh JR, Posselt AM. Islet transplantation for Type 1 diabetes: where are we now? *Expert Review of Clinical Immunology* 2015; 11: 59–68.
165. Thorson TJ, Gurlin RE, Botvinick EL, et al. Bijel-templated implantable biomaterials for enhancing tissue integration and vascularization. *Acta Biomaterialia* 2019; 94: 173–182.